University of Stuttgart

Institute of Geodesy

Understanding the limitations of Sentinel-3 inland altimetry through validation over the Rhine River

Master Thesis

Geodesy and Geoinformatics

University of Stuttgart

Nicholas M. Schneider

Stuttgart, December 2022

Supervisor: Dr.-Ing. Mohammad J. Tourian
University of Stuttgart

Erklärung der Urheberschaft

Ich erkläre hiermit an Eides statt, dass ich die vorliegende Arbeit ohne Hilfe Dritter und ohne Benutzung anderer als der angegebenen Hilfsmittel angefertigt habe; die aus fremden Quellen direkt oder indirekt übernommenen Gedanken sind als solche kenntlich gemacht. Die Arbeit wurde bisher in gleicher oder ähnlicher Form in keiner anderen Prüfungsbehörde vorgelegt und auch noch nicht veröffentlicht.

Ort, Datum Unterschrift

Abstract

Satellite altimetry is developing into one of the most powerful measurement techniques for long-term water body monitoring thanks to its high spatial resolution and its increasing level of precision. Although the principle of satellite altimetry is very straightforward, the retrieval of correct water levels remains rather difficult due to various factors. Waveform retracking is an approach to optimize the initially determined range between the satellite and the water body on Earth by exploiting the information within the power-signal of the returned radar pulse to the altimeter. Several so-called retrackers have been designed to this end, yet remain one of the most open study areas in satellite altimetry due to their crucial role they play in water level retrieval. Moreover, geophysical properties of the stratified atmosphere and the target on Earth have an effect on the travel time of the transmitted radar pulse and can amount to several meters in range.

In this study we provide an overall analysis of the performances of the retrackers dedicated to the Sentinel-3 mission and the applied geophysical corrections. For this matter, we focus on nine different locations within the Rhine River basin where locally gauged data is available to validate the Sentinel-3 level-2 products. Furthermore, we present a reverse retracking approach in the sense that we use the given in-situ data to determine the offset to each altimetry-derived measurement of every epoch. Under the assumption that these offsets are legitimate, they can be seen as an a-posteriori correction which we project onto the range and thus on a waveform level. Further analyses consist in the investigation of the relationship these a-posteriori corrections have to the waveform properties of the same epoch.

Later, the question whether the a-posteriori corrections to the initial retracking gates are appropriate for the retrieval of correct water levels, drives us to assign a probability to each and every bin of the waveform. Following this idea, we design stochastic-based retrackers which determine the retracking gate for water level retrieval from the bin with the highest probability assigned to it. To distribute the probabilities across all bins of the waveform, we consider three empirical approaches that take both the waveform itself and its first derivative into account: Addition, multiplication and maximum of both signals. For all three of the new retrackers, we generate the water level timeseries over the aforementioned sites and validate them against in-situ data and the retrackers dedicated to the Sentinel-3 mission.

Contents

List of Figures

List of Tables

Chapter 1

Introduction

1.1 Motivation to water body monitoring

The availability of surface water is fundamental to all life on Earth. So called wetlands only cover around 5% of the Earth's ice-free surface, but play a key role in the hydrological and biogeochemical cycles, as well as in the ongoing climate change (Prigent et al., 2007). Millions of people congregate around rivers since they serve as a source of drinking water and resource to renewable energy. Rivers are essential to continental navigation, transportation, flood control, irrigation and hydropower generation (Ho, 2017). Likewise, lakes and ponds are of great human importance in the sense that they provide water for domestic, industrial and agricultural use (Brönmark and Hansson, 2002), not to mention the huge role they play for wildlife and the local ecosystem itself. However, global warming and anthropogenic interactions are taking a toll on inland surface water and consequently on the hydrological cycle. More than 162,000 km^2 of water bodies previously considered as permanent have changed their characteristics over the past three decades, namely 90,000 km^2 of which have vanished entirely and 72,000 km^2 have turned into a seasonal state (Pekel et al., 2016). With evergrowing global temperatures one can only expect these losses to accelerate. Furthermore, the occurrences of climate-related extremes, such as floods and droughts are projected to increase with medium to high confidence in the 21st century (Field et al., 2012). As a matter of fact, even Central Europe which, in the past, has comparably been spared from natural hazards due to its advantageous geographic setting, has proven itself to be more exposed to climate-related extremes than ever before. As recent as summer 2021, record rainfall caused severe flooding events adjacent to the Rhine River in North Rhine-Westphalia and Rhineland-Palatinate, in which 40,000 lives were directly affected and several lost (Bosseler et al., 2021). Only one year later in the summer of 2022, 47% of Europe was considered in warning conditions and 17% in alert conditions by the Combined Drought Indicator (CDI) resulting in moderately to severely low water levels in the Rhine river. As an effect, discharge has been plummeting and thus significantly hampering the lower Dutch reaches of the river in terms of water distribution systems, dike stability, commercial navigation and oil transport (Toreti et al., 2022).

There is no doubt that a preliminary step to any countermeasures towards evergrowing occurrences of climate-related extremes, consists in the observation and detection of their outcomes on the Earth's surface. In particular, inland water body monitoring from space has become one of the most common fields of remote sensing applications and is evolving to be the most reliable as the number of in-situ gauging stations is rapidly decreasing. Among several other remote sensing techniques, satellite altimetry is a very renowned technique for the acquisition of water levels.

1.2 The development of satellite altimetry

The early ages of satellite altimetry missions began in 1969 at the Williamstown Seminar where experts from solid Earth and ocean domains found themselves discussing and evaluating the potential of this novel water body observation technique. The concept was promising and consequently initiated the development of increasingly accurate satellite altimeter systems in the course of the 1970s and 1980s, followed by a maturity age and later by far newer technologies (Stammer and Cazenave, 2017).

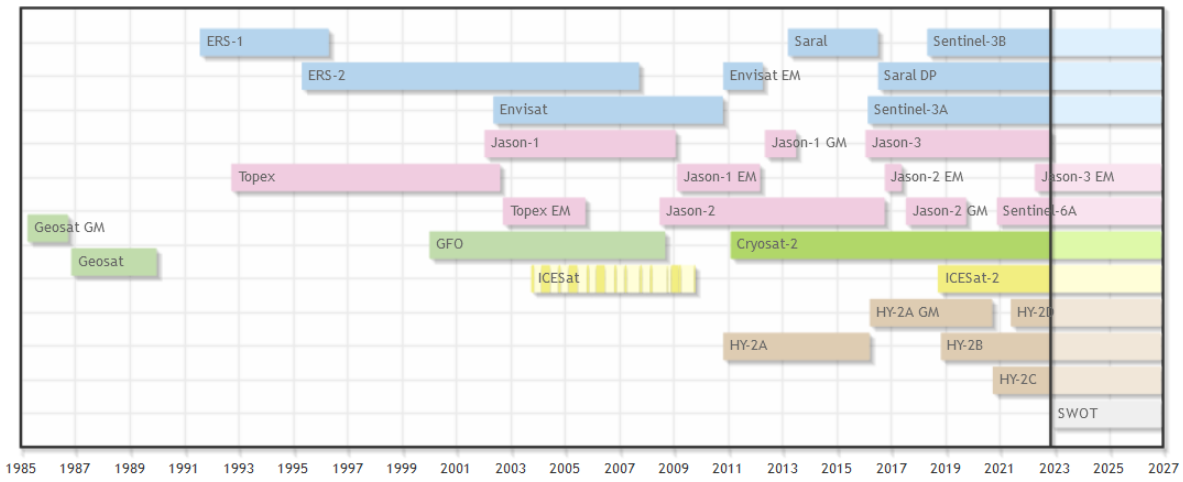

Figure 1.1: *Active, past and future satellite altimetry missions (OpenADB, TUM)*

Figure 1.1 visualizes the lifetime of all altimetry missions. Among these, several have terminated, some are currently operating and few are yet to be launched. Table 1.1 lists additional information on the entirety of satellite altimetry missions (Tourian et al., 2022).

Table 1.1: *Satellite altimetry mission details*

Mission	operated by	lifetime	height [km]	inclination [°]	rev./day	frequency [GHz]
Geosat	NOAA	03.1985-09.1989	785	108.0	244/17	13.5
ERS-1	ESA	07.1991-03.2000	785	98.5	501/35	13.5
TOPEX/Poseidon	CNES, NASA	09.1992-01.2006	1336	66.0	127/10	13.6 & 5.3
ERS-2	ESA	04.1995-09.2011	781	98.5	501/35	13.5
GFO	US-Navy	02.1998-11.2008	784	108.0	244/17	13.5
Jason-1	CNES, NASA	01.2002-06.2013	1336	66.0	127/10	13.6 & 5.3
ENVISAT	ESA	03.2002-04.2012	800	98.5	501/35	13.5 & 3.2
Jason-2	CNES, NASA, NOAA, EUMETSAT	06.2008-ongoing	1336	66.0	127/10	13.6 & 5.3
HY-2A	NSOAS	08.2011-ongoing	971	99.3	193/14	13.58 & 5.25
ICeSat	NASA	01.2003-10.2009	600	94.0	2723/183	Laser: 1064 & 532 nm
CryoSat-2	ESA	04.2010-ongoing	717	92.0	5344/369	13.575
SARAL/AltiKa	ISRO, CNES	02.2013-ongoing	800	98.5	501/35	35.75
Jason-3	CNES, NASA, NOAA, EUMETSAT	01.2016-ongoing	1336	66.0	127/10	13.6 & 5.3
Sentinel-3A	ESA, GMES	02.2016-ongoing	815	98.6	385/27	13.6 & 5.3
Sentinel-3B	ESA, GMES	04.2018-ongoing	815	98.6	385/27	13.6 & 5.3
ICeSat 2	NASA	09.2018-ongoing	480	92.0	1387/91	Laser: 1064 & 532 nm
HY-2B	NSOAS	10.2018-ongoing	971	99.3	193/14	13.58 & 5.25
Sentinel-6 Michael Freilich	EUMETSAT, NASA	11.2020-ongoing	1336	66.0	127/10	13.5
SWOT	NASA, CNES	12.2022-ongoing	890	77.6	292/21	35.75

The first United States space station, Skylab (1973-1974), saw the initial deployment of radar technologies for Earth observation purposes and served the acquisition of undulations in the marine geoid. Shortly after, the measurement principle was enhanced on the Geodynamic

Experimental Ocean Satellite (GEOS 3, 1975-1979), providing more accurate altimetric observations as well as the satellite's altitude using a laser retroreflector array. GEOS 3's altimeter also proved to deliver valid measurements over land and sea ice (Stammer and Cazenave, 2017). Later, in 1978, data quality was rapidly improving with the Seasat whose altimeter met the performance specification for 10-cm precision in the altitude measurements. In addition, Seasat's altimeter measured surface wave heights and ocean-surface backscatter coefficients from which wind speed can be derived (Tapley et al., 1982). Subsequently, Seasat became a "standard" for altimetric satellites that were yet to come. Geosat (1985), to name one, marked the first satellite altimetry mission primarily developed for geodetic purposes, such as ocean circulation, marine gravity/ bathymetry and continental ice, and was operated by the US Navy (Lillibridge et al., 2006).

The maturity age began with the TOPEX/Poseidon mission (1992-2006) which was designed to provide high-precision altimetry for mesoscale and large scale monitoring, in particular for the study of the circulation of the world oceans (Fu et al., 1994). Therein, two radar altimeter instruments were used, namely a dual-frequency altimeter (ALT) in C and Ku bands and a solid-state altimeter, Poseidon-1. Adding a dual frequency enabled the correction of ionospheric propagation effects. Furthermore, a three-band microwave radiometer (TMR) was introduced for wet tropospheric propagation effects. Partly overlapping in time, the European Remote Sensing satellite (ERS-1; 1991-2000) was in orbit, sampling data dedicated to mesoscale monitoring and providing high latitude information. Along with a follow-on operation of the Geosat, these missions established minimal time and space coverage over the ocean which became a big milestone in oceanography. Soon to follow was the Jason series (Jason-1, Jason-2, Jason-3) in which the accuracy of the TOPEX/Poseidon mission was not only maintained, but even improved and being optimized for an operational series. While payload equipment was advancing, the Jason series was capable of reducing the satellite mass by a factor of five with respect to the TOPEX/Poseidon spacecraft. Concurring with these missions were the ERS-2, following its predecessor, as well as Envisat and HY-2 (Stammer and Cazenave, 2017).

Newer technologies involving the use of the Synthetic Aperture Radar Altimeter (SRAL) marked the beginning of a another new era in satellite altimetry. CryoSat-2 is an ongoing mission and is the first satellite to be equipped with the SRAL. This altimeter encompasses a delay-Doppler mode (Synthetic Aperture Radar or SAR mode) as well as a SAR-Interferometric mode which adds cross-track slopes to the nadir topography. Initially CryoSat-2 was designed for ice measurements, but has proven itself to be useful for ocean monitoring and coastal applications as well. SARAL/AltiKa introduces another innovative radar altimetry mission utilizing a Ka-band altimeter concept involving the use of higher frequency and wider bandwidth. By utilizing the Ka-band, ionospheric effects are reduced, a smaller footprint is set up and horizontal and vertical resolutions are optimized (Verron et al., 2021). The Sentinel-3 mission aspires to provide long-term altimetric measurements from both of its satellites, Sentinel-3A and Sentinel-3B. Its payload is comprised of a dual-frequency (Ku and C) radar altimeter, complemented with a delay-Doppler capability to achieve high along-track resolution and reduced noise level (see Chapter 2). Following the launch of the Sentinel-3 satellites, the ongoing Sentinel-6 and recently launched SWOT missions are to join the state-of-the-art in satellite altimetry optimizing radar data sampling and aiding the global observation of surface water storage change, respectively (Donlon et al., 2021; Biancamaria et al., 2016).

1.3 Basic concepts of satellite altimetry

1.3.1 Measurement principle

In principle, satellite altimetry is based on a very simple and straightforward geometric setup. The main objective is to measure the range from the satellite to the surface of the water body by transmitting a radar pulse with known power from the altimeter towards the surface. Water bodies resemble a mirror in the sense that they reflect the pulse off of their surface, from which a portion heads back to the altimeter. Using half of the two-way travel time for the pulse to reach the altimeter and the speed of light, the range can be computed and corrected for atmospheric and geophysical effects following equation 1.1.

$$\rho = \hat{\rho} - \sum_{j} \Delta\rho_j \tag{1.1}$$

Hereby, $\hat{\rho}$ is the computed range, taking into account a number of geophysical corrections, $\Delta\rho_j$, resulting in the final range ρ. Subtracting the range from the satellite's altitude delivers the water surface elevation with respect to the reference ellipsoid (Fu and Cazenave, 2000).

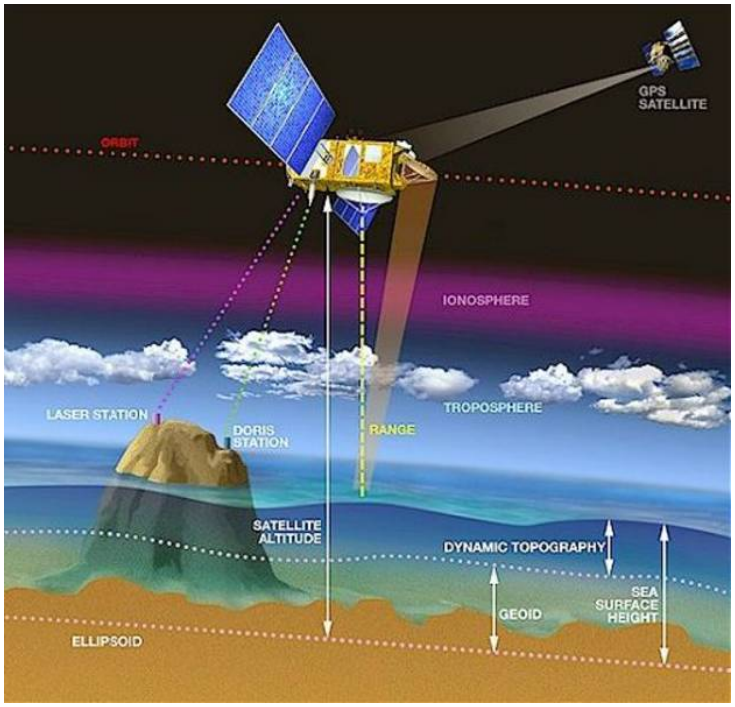

Figure 1.2: *Basic measurement concept of satellite altimetry (credit: CLS/AVISO)*

Figure 1.2 visualizes the measurement principle of satellite altimetry. The aforementioned corrections are a crucial measure to determine a precise range as the radar signal is impacted by various geophysical phenomena on its path between the satellite and the Earth's surface. These effects can amount to magnitudes from decimeters to meters which further underlines their importance (Stammer and Cazenave, 2017). Propagation corrections are those accounting for the

delay of the radar signal due to the properties of the stratified atmosphere. They consist of an ionospheric (3-5 cm), a wet tropospheric (3-45 cm) and a dry tropospheric (2.3 m) correction (Ablain et al., 2017). Ionospheric effects are traced back to the presence of free electrons in the upper atmosphere at altitudes between 50 and 2000 km. The wet troposphere effect is based on the integrated amount of water vapor and, to a lesser extent, on the integrated amount of liquid water. Likewise, the quantity of water vapor contributes to the dry troposphere effect along with dry gases that delay the radar pulse most significantly. Sea state bias is a target correction that typically only applies to oceans or large lakes. It is defined by the nonlinear, non-Gaussian and skewed nature of surface waves in addition to the fact that the curvature radius of wave troughs are larger than that of wave crests. These height differences within the illuminated footprint cause offsets to the mean water surface height and thus to the range measurement itself (Stammer and Cazenave, 2017). Further geophysical corrections encompass ocean tides (up to few meters), loading effects, solid Earth tides (3 dm), polar tides (1 cm) and the inverted barometric effect (up to 3 dm). Ocean tides and the inverted barometric effect however, can also be excluded from inland applications.

1.3.2 Satellite radar altimetry waveform

Pulse-limited satellite radar altimeters produce waveforms that contain information on the range in nadir direction, the reflectivity and on the roughness of the surfaces (Deng, 2003). In principle, these waveforms are temporal profiles (Marth et al., 1993) and can be utilized for optimizing the computed range between the satellite and the surface of the water body.

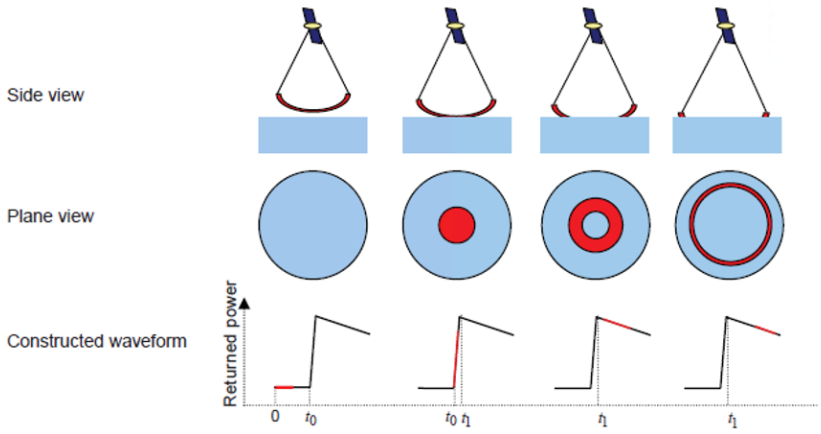

Figure 1.3: *Interaction principle between radar pulse and surface (Tourian, 2013)*

Figure 1.3 demonstrates four characteristic steps of interaction between the radar pulse transmitted by the altimeter and the surface, as well as the corresponding waveform. In the first step, an electromagnetic pulse of known power is released in nadir direction towards the Earth by the altimeter onboard the satellite. When the pulse reaches the surface, only a point is illuminated as the wavefront resembles a spherical shell. It is then reflected back towards the satellite. In the constructed waveform, this can be seen as a sharp increase in returned power, called the leading edge. The illuminated point evolves into a filled circle as the wavefront interacts with surfaces slightly off of nadir. After it reaches its maximal area, and thus a peak in

the constructed waveform, both the returned power and the illuminated surface gradually decrease again. At this instant, the illuminated surface rather corresponds to an annular ring with decreasing width and increasing diameter. In the constructed waveform, this gradual decrease is called the trailing edge (Robinson, 2004).

The waveform presented in figure 1.3 is a rather idealized one, which in reality is far more noisy. Consequently, a mean waveform of so-called multiple looks is generated which optimizes the shape of the waveform for that specific time (Robinson, 2004). In other words, this averaged waveform is set up by a timeseries of the mean returned power recorded by the satellite's altimeter and consists of three main parts (Tourian, 2013; Chelton et al., 2001):

- **Thermal noise**: Before the radar pulse reaches the altimeter after being reflected from the surface, a noise level is sampled which is generated by the instrument itself. The power of this noise level is relatively low and constant.
- **Leading edge**: Here, the main part of the waveform begins where the returned power sharply increases until its maximum. Typically, information on the Surface Wave Height (SWH), as well as on the range between the satellite's altimeter and the mean sea surface is gained from the leading edge.
- **Trailing edge**: In this portion of the waveform, the returned power steadily decreases.

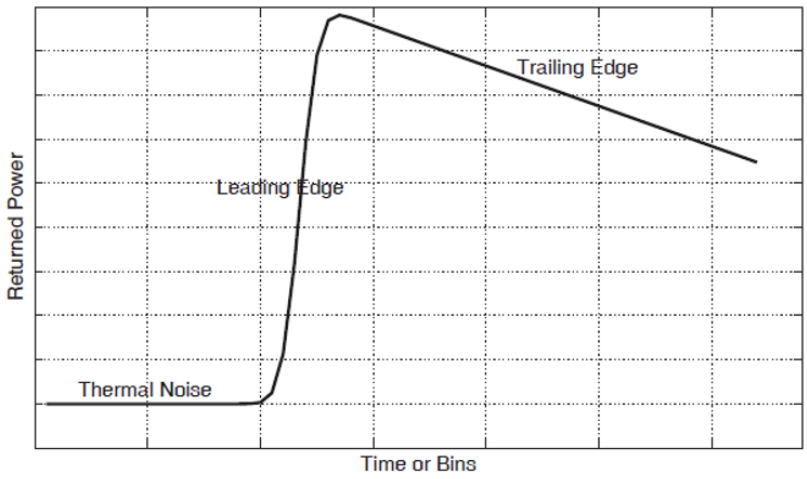

Figure 1.4: *Representation of an ideal waveform and its three main components (Tourian, 2013)*

The mean sea level is defined as half of the distance between wave crests and troughs. By tracking half of the power on the leading one can obtain the mean sea level from the constructed waveform.

1.3.3 Waveform retracking

On a waveform level, the range between the altimeter and the target on Earth is related to the transit time of the received radar pulse, more precisely to the time the received pulse reaches half of the leading edge's height. The receiver of the altimeter opens a given window of time to, among other factors, avoid information from the preceding and following signals being

recorded erroneously. Consequently, the waveforms are stored in a series of range gates (EUMETSAT, 2019). To know when to open and close the window, the satellite estimates the time that the leading edge of the signal is projected to return. The predicted range gate is commonly know as the tracking gate. There are two modes for setting the tracking window. Closed-loop mode is based on an analysis of the previously received waveform and therefore determines the tracking window in near-real time. In open-loop mode, a-priori information in form of pseudo-DEM look-up tables are used. In other words, the look-up table provides information on the approximate elevation of the satellite's instantaneous location on the Earth's surface (EUMETSAT, 2019).

Waveform retracking is a post-processing measure to improve the initially obtained range from the tracking gate. Usually the tracking gate is offset to the leading edge and therefore does not accurately represent the correct point of water level retrieval. Consequently, retracking was developed to find the correct point in the waveform. Different retrackers of physical and empirical approaches can be more suited to specific surfaces as the returned waveforms widely vary in shape and size (Shu et al., 2020). The algorithms suggested for the Sentinel-3 Level-2 products and hence considered in this study are listed as follows:

- Ocean: Inherited from the SAMOSA project, the Ocean retracker is fully analytical and designed for open ocean and coastal zones applications. It's aim is to fit the theoretically modeled multi-look waveform from Level-1B to the real Level-1B SAR waveform [1].
- Offset Center of Gravity (OCOG): The OCOG retracker is an empirical algorithm used mainly for sea-ice margins in SAR mode. The retracking gate is determined based on the offset to the center of gravity of the waveform's peak. For this, the width and amplitude of the peak must be estimated beforehand [2].
- Ice sheet: In Ice sheet retracking, a semi-analytical model of the returned waveform is fitted according to the least squares approach. The model is a modified gaussian form corresponding to a six parametrizable function [3].
- Ice: The Ice retracker is a physical-based one intended for ice caps studies. It tries to detect the waveform's edge and subsequently fits an error function to the leading edge and an exponential decrease to the trailing edge [4].
- Sea-ice: Sea-ice retracking is also an empirical algorithm modeling the leading edge as a Gaussian, fitting an exponential function to the decaying trailing edge, and additionally using a third order polynomial function [5].

Most of the above apply to both modes of operation, LRM and SAR. In this study, we only consider SAR waveforms and therefore use those retrackers which apply to them.

[1] https://sentinels.copernicus.eu/web/sentinel/technical-guides/sentinel-3-altimetry/level-2/re-tracking-estimates/ocean

[2] https://sentinels.copernicus.eu/web/sentinel/technical-guides/sentinel-3-altimetry/level-2/re-tracking-estimates/ocog

[3] https://sentinels.copernicus.eu/web/sentinel/technical-guides/sentinel-3-altimetry/level-2/re-tracking-estimates/ice-sheet

[4] https://sentinels.copernicus.eu/web/sentinel/technical-guides/sentinel-3-altimetry/level-2/re-tracking-estimates/ice

[5] https://sentinels.copernicus.eu/web/sentinel/technical-guides/sentinel-3-altimetry/level-2/re-tracking-estimates/sea-ice

1.4 Problem statement

In satellite altimetry the precision of derived water levels, among other factors, strongly depends on the retracking algorithms used on the returned waveforms (Ridley and Partington, 1988). In the previous section, the concepts of different retracking algorithms were briefly explained. In chapter 3, we perform a preliminary analysis to investigate the performance of such retrackers and their importance to water level retrieval. There are many factors that account for uncertainty in the calculation of water levels, but an error from waveform-retracking, and thus in the range, is particularly influential. In fact, range corrections from retracking methods typically amount to several meters (Martin et al., 1983).

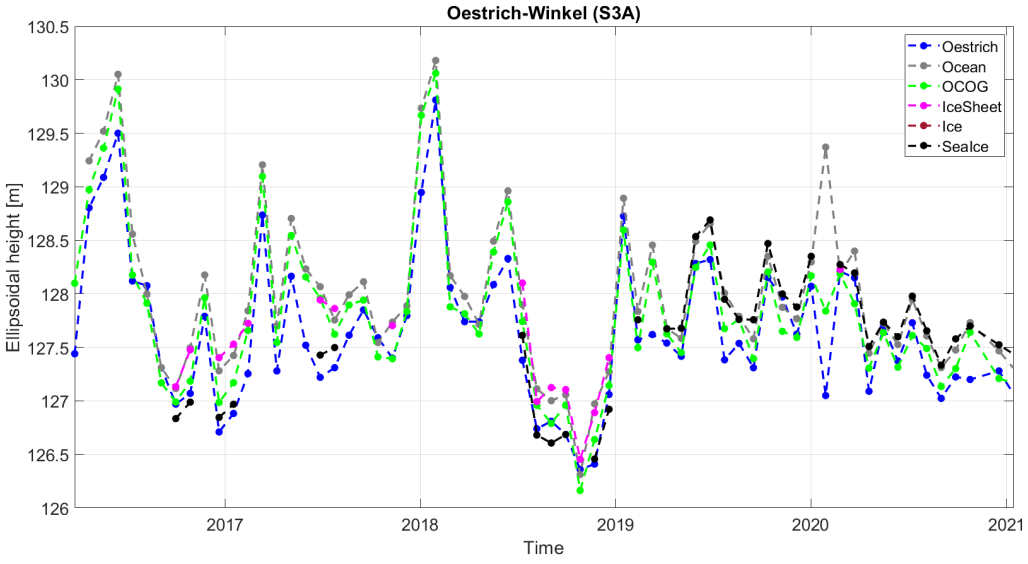

Figure 1.5: *A demostration of the variation between water levels derived from different retrackers*

The differences in water levels that occur as a result of different retracking techniques is presented in figure 1.5. Plotted against the blue in-situ data from the local gauge in Oestrich are the water level timeseries derived from five different retrackers dedicated to the Sentinel-3 mission. What becomes noticeable is the fact that these different retrackers produce clear variations among each other's water levels. For the vast majority of the epochs their differences remain below one meter, yet must be taken seriously nonetheless. Certainly, the arrangement of geophysical corrections also causes variations. However, this issue can be dealt with subsequent to the retracking of waveforms. The assessment and evaluation of retracking algorithms, as well as the designing of new ones, is one of the most open study areas in satellite altimetry. That being considered, research conducted on retrackers' performances and further comprehensive analyses of which still remain insufficient.

Gao et al. (2019) undertake a brief analysis of the Ocean, OCOG and the so-called Threshold retracker on Senintel-3 data, yet come to find no significant differences between their results in the Ebro River basin. In a study over lakes in the USA and Canada, Nielsen et al. (2020) make rather opposing findings, indicating that an empirical retracker delivers significantly better results compared to a physical one. This discovery followed a performance-evaluation of retracked Sentinel-3A data over more than 100 lakes. Furthermore, Shu et al. (2020) compare lake

water levels determined by the standard SRAL SAR retrackers against in-situ water level measurements over ice-covered lakes. Herein, the Sea-ice retracker was surprisingly not capable of providing continuous estimates of lake water levels due to high rate of missing data. Moreover, the remaining retrackers delivered very similar lake water estimates, among which the Ocean retracker revealed the lowest bias with respect to the in-situ data. Both studies however, were done in geographically contrasting settings, implying that their results do not necessarily apply to a general case study. The need for more studies taking into account the neighboring topography, slope conditions of rivers, crossing angles with the satellite's groundtrack and the like, still remain.

Towards developing novel retracking methods for SAR waveforms, Villadsen et al. (2016), to mention one, propose the Multiple Waveform Persistent Peak (MWaPP) retracker. It focuses on a narrowed down portion of the waveform, but also takes the shape of adjacent waveforms into account. The novel method proved to alleviate difficulties from off-nadir bright targets and topographic challenges and showed significantly favorable results over various iconic global rivers and lakes of different hydrological characteristics. Passaro et al. (2020) extend an earlier retracking strategy of theirs called ALES+ to all available altimetry missions including Sentinel-3A/B. In contrast to its predecessor, the further developed ALES+ SAR adopts a rather simplified version of the Brown-Hayne functional form as an empirical retracker to determine the mid-point of the waveform's leading edge. Tested over Sweden's Southwestern coast, the refined retracker's results are quite promising after validation against the local gauge data. The question does arise however, how such a retracker performs over water bodies with other dynamics such as rivers, lakes and reservoirs. In another study, Dinardo et al. (2021) enhance the SAMOSA retracker by taking advantage of the so-called Range Integrated Power (RIP), a new waveform constructed from the integration of the Doppler beams in the range direction. The RIP is converted into a surface backscattering profile which can subsequently be integrated in the SAMOSA retracker. Clear improvements thanks to the refined retracker are limited to coastal zones only, however. In conclusion, analyzing and evaluating SAR waveform retracker's performances, particularly those dedicated to the Sentinel-3 mission, is still not sufficiently studied on, despite of the role retracking plays in satellite altimetry. As mentioned, several studies attempt to design new retracking methods, which on the one hand show promising findings and improvements compared to preceding results, yet on the other hand are oftentimes limited to specific cases of water bodies, geographic locations or altimetry missions.

1.5 Objectives

This study is driven by the aim to better understand the limitations of Sentinel-3 inland altimetry through validation using locally gauged data. Later, we aspire to establish a new methodology towards designing our own retrackers. We use Sentinel-3 Level-2 data containing high-frequency measurements (Ku band) acquired in SAR mode by the S3A and S3B satellites. We focus on a variety of interesting geographic locations within the Rhine River basin representing a multitude of geometric and geomorphological characteristics. To summarize, the objectives of this study can be expressed as follows:

1. Assessing the performance of retrackers and provided geophysical corrections
2. Analyzing waveforms' properties and a-posteriori corrections from in-situ data
3. Introducing stochastic-based retrackers

1.6 Outline

For the continuation of this study, we first provide an overview and description of the data used in this study. In chapter 3 we undertake a preliminary analysis in which the main emphasis for one lies on the performance of retrackers and permutations of geophysical corrections, and for another on the properties of the waveforms themselves in direct comparison with a-posteriori corrections we obtain from in-situ data. In the next chapter, we demonstrate our methodology with the aim to design stochastic-based retrackers following a probability distribution to each bin of the waveform. Subsequently, we present and discuss the results we achieve from the novel retrackers, followed by a summary and conclusion in chapter 5.

Chapter 2

Case study and data

2.1 Case study

Aiming towards properly understanding the limitations of Sentinel-3 inland altimetry, we choose nine different sites within the Rhine river basin (figures 2.1 and 2.2) over which the satellites' measurements will be validated. The Rhine is with a length of around 1250 km one of Europe's longest rivers flowing from the Alps in a northwesterly direction into the North Sea. Today, there are nine sovereign states that lie partly or wholly within its 185000 km^2-large drainage basin, namely Austria, Belgium, France, Germany, Italy, Liechtenstein, Luxembourg, The Netherlands and Switzerland. Together with numerous interconnections, such as channels, tributaries and distributaries, as well as adjacent lakes, the Rhine river basin marks Europe's busiest hydrological artery harboring nearly 50 million people within its boundaries. The Rhine is a classic example of a "multipurpose" waterway, used for transportation, power generation, industrial production, urban sanitation, and agriculture. Furthermore, the Rhine has the longitudinal profile of a textbook river: It drops sharply and flows quickly in the Alpenrhein tributary system following the convergence of its two headstreams, Hinterrhein and Vorderrhein. This initial tributary system is essentially fed by glacial runoff and melting snow from hundreds of tiny rivulets. It becomes slower and braided in its middle reaches of the Oberrhein via Mittelrhein and onto Niederrhein, and finally becomes sluggish as it approaches its delta in the Netherlands (Cioc, 2002).

Out of the nine locations, five are along the Rhine river itself while the other four consist of adjacent lakes and distributaries. The main criteria for the selection of these specific sites are the geometric and geomorphological characteristics, in particular taking into account the topography bordering the water body and the crossing angle of the satellite's groundtrack with respect to the water body.

Table 2.1: *An overview of the chosen virtual stations and their characteristics*

		Sentinel-3A			Sentinel-3B			
Object	Country	Track	Crossing ang.	Coordinates	Track	Crossing ang.	Coordinates	Neighboring topography
Lake Constance	Germany	313	ca. 45	47.7373, 9.1892	700	ca. 90	47.6338, 9.3367	flat
Lake IJssel	Netherlands	672	irrelevant	52.7360, 5.5392	199	irrelevant	52.7360, 5.5392	flat
Lake Zurich	Switzerland	586	ca. 90	47.2293, 8.7039	313	ca. 90	47.2198, 8.9328	mountainous
Oestrich-Winkel	Germany	358	ca. 45	49.9877, 7.9993	-	-	-	relatively flat
Groote Lindt	Netherlands	741	ca. 65	51.8070, 4.5907	672	ca. 70	51.7990, 4.6224	flat
Sankt Sebastian	Germany	-	-	-	313	ca. 20	50.4098, 7.5739	flat
Vuren	Netherlands	672	ca. 90	51.8236, 5.1017	85	ca. 90	51.8191, 5.0519	flat
Mannheim	Germany	313	ca. 0	49.6398, 8.3826	-	-	-	flat
Spay	Germany	-	-	-	358&313	ca. 45	50.2484, 7.6468	flat

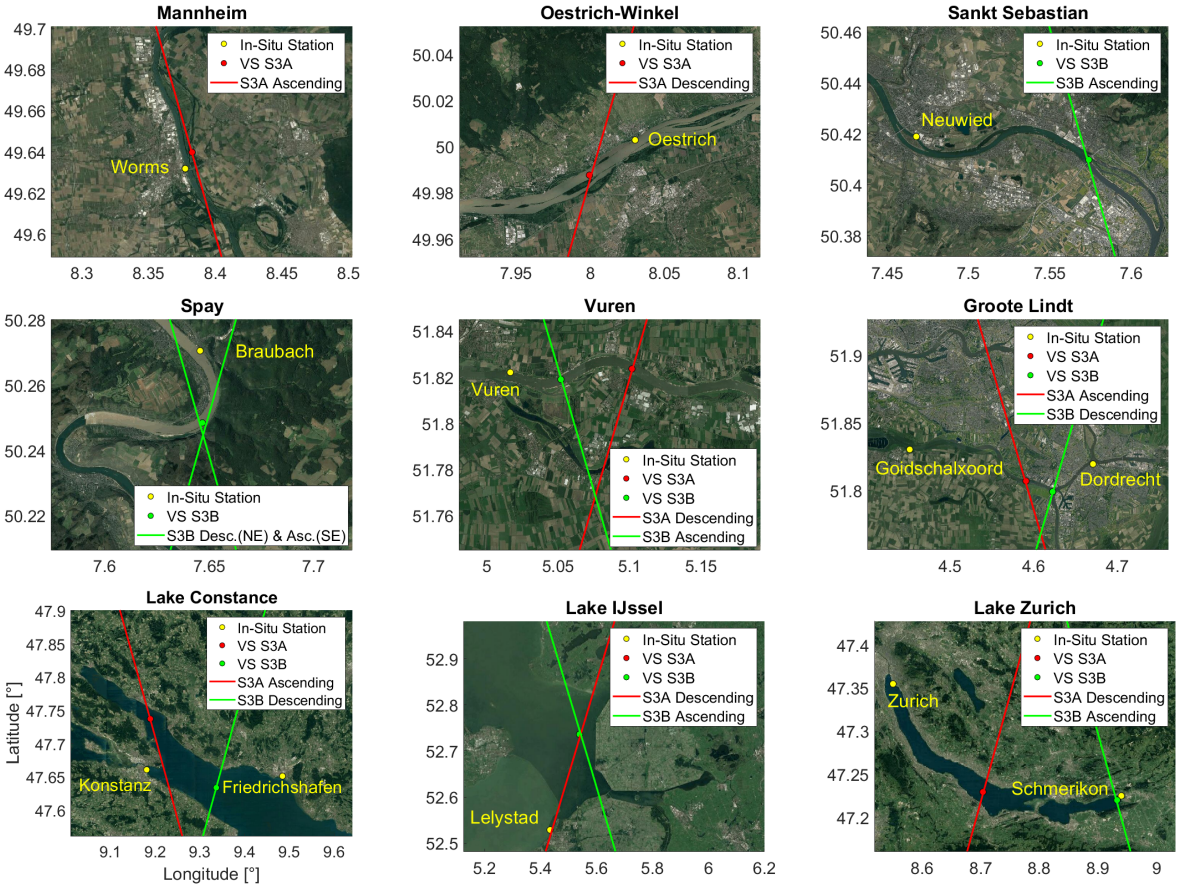

Figure 2.1: *Overview of all virtual stations and nearby validation sites*

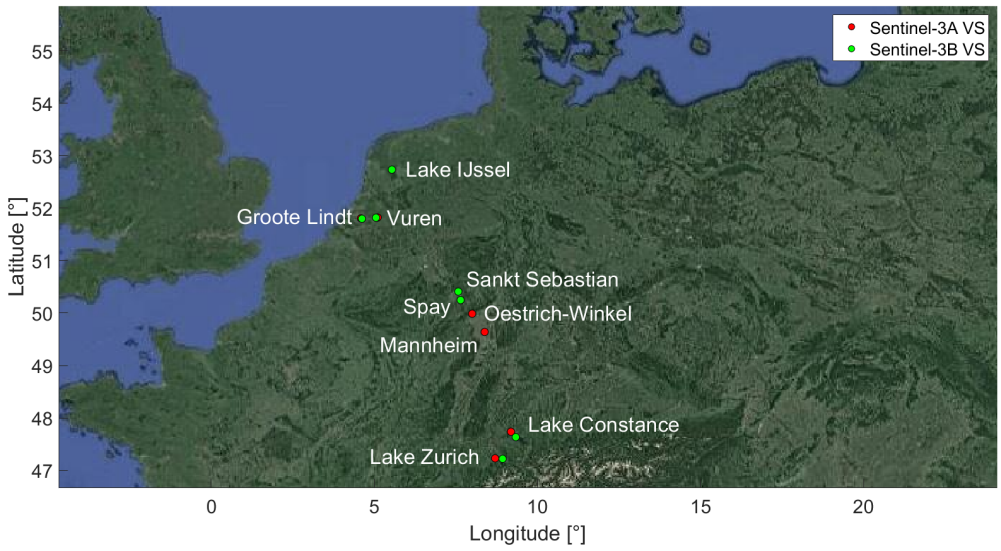

Figure 2.2: *Map displaying all virtual stations*

Table 2.1 lists all the chosen virtual stations for the validation of the altimetric measurements, as well as some information on the satellites' bypasses and the geomorphological characteristics. Furthermore, figure 2.1 depicts the information provided in the table and the nearest validation sites onto tiles of satellite images. Lastly, all virtual stations can be seen in the overview map in figure 2.2.

2.2 Data

2.2.1 Sentinel-3 data

In this study we work with Level-2 altimetry data delivered by the two satellites Sentinel-3A and Sentinel-3B. Sentinel-3 is an ongoing mission by the joint program of ESA and EUMETSAT in which its first satellite (S3A) was launched on 16 February 2016 and the second (S3B) on 25 April 2018. Essentially, the objective of the mission is measuring the sea surface topography, sea and land surface temperature, as well as ocean and land surface color with high accuracy and reliability. Such observations are intended to support ocean forecasting systems, environmental monitoring and climate monitoring. At an inclination of 98.65°, both satellites of the Sentinel-3 mission operate on a near-polar, sun-synchronous orbit in 814.5 km altitude. The orbit's high inclination ensures optimal coverage of ice and snow parameters in high latitudes. To further densify the pattern of coverage, both satellites are offset by a 140° phase. One orbital cycle takes 27 days (Bourg et al., 2021). The spacecraft is equipped with four main instruments:

- OLCI: The Ocean and Land Colour Instrument is a push-broom imaging spectrometer containing five cameras which produces a swath width of 1270 km [1].
- SLSTR: The Sea and Land Surface Temperature Instrument is a conical scanning imaging radiometer that employs an along track scanning dual view technique of 1420 km in nadir and 750 km in backward direction [2].
- SRAL: The SAR Radar Altimeter is a dual-frequency SAR altimeter emitting pulses within the Ku band at 15.575 GHz and C band at 5.42 GHz, respectively. Possible radar measurement modes of the altimeter are the Low Resolution Mode (LRM) and Synthetic Aperture Radar (SAR) mode [3].
- MWR: The Microwave Radiometer is designed to measure brightness temperature at 23.8 GHz and 36.5 GHz. The lower frequency channel is mostly sensitive to atmospheric water vapor while the higher frequency channel is most sensitive to cloud liquid water [4].

In addition, the main instruments of the Sentinel-3 satellites are complemented by three more systems for Precise Orbit Determination (Bourg et al., 2021):

- DORIS: A Doppler orbit radio positioning system
- GNSS: The GNSS component is a GPS receiver which provides precise orbit determination and tracks multiple satellites simultaneously.

[1] https://sentinels.copernicus.eu/web/sentinel/missions/sentinel-3/instrument-payload/olci
[2] https://sentinels.copernicus.eu/web/sentinel/missions/sentinel-3/instrument-payload/slstr
[3] https://sentinels.copernicus.eu/web/sentinel/missions/sentinel-3/instrument-payload/altimetry
[4] https://sentinels.copernicus.eu/web/sentinel/technical-guides/sentinel-3-altimetry/instrument/mwr

- LRR: This is in place to accurately locate the satellite in orbit using a Laser Retro-Reflector system.

Relevant to this study is the Level-2 product from the surface topography mission payload, namely from the SAR Radar Altimeter (SRAL). The Level-0 product is not disseminated to the users and consists of reconstructed and time sorted measurements at full space-time resolution where only few artefacts and errors are removed. Among the SRAL-derived Level-1 products the Level-1A contains unpacked L-0 complex echoes (sorted and calibrated), the Level-1B consists of LRM and SAR averaged measurements (20 Hz) and lastly the Level-1B-S include the regular Level B product, but enriched with SAR expert information. Finally, the Level-2 product provides altimeter range, orbital altitude, time, water vapor from the MWR and geophysical corrections, as well as significant wave height and wind-speed information. More precisely, the SRAL Level-2 products are split in marine and land products. SRAL Level-2 marine products encompass data acquired over open ocean, coastal areas, sea-ice and over near-coastal parts of land whereas SRAL Level-2 land products include the information sensed over land, coastal areas, land ice and inland water bodies (Date, 2016).

SRAL altimeter measurements take place either in Low Resolution Mode (LRM) or in Synthetic Aperture Radar (SAR) mode. The LRM mode is the rather conventional altimeter pulse limited mode which typically interleaves Ku-band and C-band pulses following a sequence of 3 Ku-band / 1 C-band / 3 Ku-band pulses. The pulses are released at a frequency around 1924 Hz to then be processed and averaged on-board generating a returned-power waveform approximately every 50.9 ms. SAR mode however, is a high along track resolution mode based on the concept of Synthetic Aperture Radar processing. Herein, pulses are released at a frequency of about 17800 Hz and by a series of 66, namely 1 C-band / 64 Ku-band / 1 C-band pulses. This series of pulses is called a burst and lasts about 12.74 ms (Date, 2016).

2.2.2 NASADEM

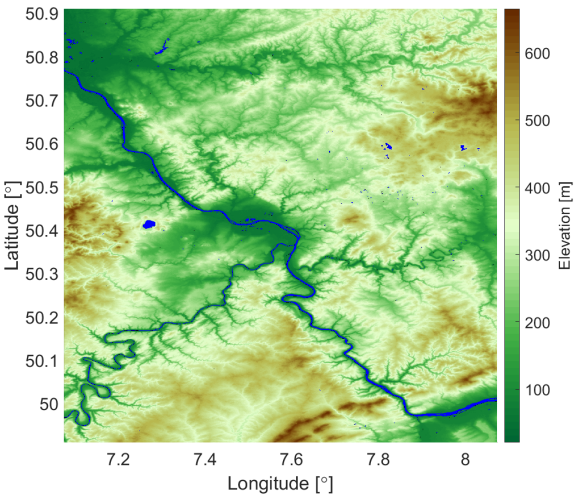

Figure 2.3: *Visualization of the NASADEM in an exemplary region*

NASADEM is a modernized version of the digital elevation model (DEM) generated from the Shuttle Radar Topography Mission (SRTM) alongside all its associated products (Buckley et al., 2020). SRTM is a joint project of the National Aeronautics and Space Administration (NASA), the National Imagery and Mapping Agency (NIMA) and the Deutsches Zentrum für Luft- und Raumfahrt (DLR) which produced the first near-global, high-resolution digital elevation map based on spaceborne single-pass interferometric SAR (Van Zyl, 2001). For the generation of NASADEM, the original SRTM raw signal radar data was reprocessed using improved algorithms and enhanced with data from the ICESat, Geoscience Laser Altimeter System (GLAS) and Advanced Spaceborne Thermal Emission and Reflection Radiometer (ASTER). The latter in particular, were unavailable during the original SRTM processing. After the modernization process, NASADEM delivers a spatial resolution of 30 m and achieves an absolute height of approximately 6.8 m following a global assessment (Rodriguez et al., 2006). Figure 2.3 shows the NASADEM in one of the regions of interest to this study, near Sankt Sebastian, Germany.

2.2.3 Water occurrence mask

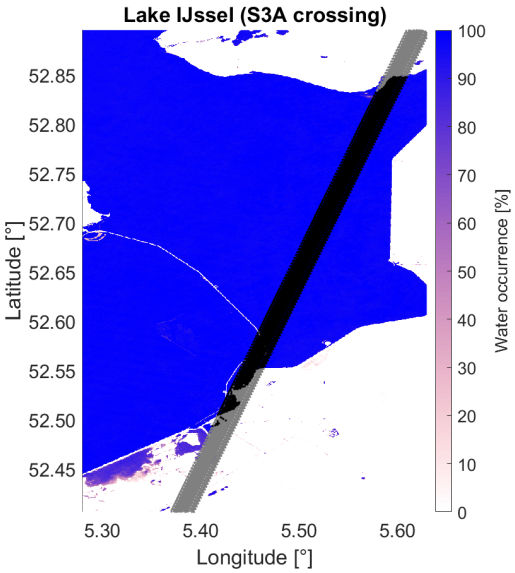

Figure 2.4: *A display of an exemplary water occurrence mask*

In order to omit returned pulses to the altimeter that are reflected from non-water surfaces we make use of water occurrence masks provided and demonstrated in Pekel et al. (2016). Hereby, we only consider those altimetric measurements that take place over surfaces with a water occurrence percentage greater or equal to 50. Figure 2.4 shows a series of Sentinel-3A crossings over Lake IJssel which is depicted by the water occurrence mask. Despite delivering data, measurements over surrounding land masses (gray dots) are omitted for the generation of water levels. Measurements that take place over the lake (black dots) are used for the continuation of this study. As mentioned, only those are chosen over portions of the lake with a water occurrence greater or equal to 50%. This threshold value is solely based on a simple trial and error approach.

2.2.4 In-situ data

In this study we take advantage of in-situ data acquired by local authorities to validate the measurements from the Sentinel-3A and Sentinel-3B satellites. In-situ data from the Netherlands and Switzerland is widely available and simple to access. In Germany, a dense network of gauging stations is in place, however, not accessible to the common user. Following individual requests, data from local authorities can be obtained free of charge.

Table 2.2: *Sentinel-3 validation sites and corresponding virtual station*

Virtual station	Satellite	In-situ station	Sampling rate	Source
Lake Constance	S3A	Konstanz	15min	LUBW
Lake Constance	S3B	Friedrichshafen	15min	LUBW
Lake IJssel	S3A	Lelystad	10min	RWS
Lake IJssel	S3B	Lelystad	10min	RWS
Lake Zurich	S3A	Zurich	10min	BAFU
Lake Zurich	S3B	Schmerikon	10min	BAFU
Oestrich-Winkel	S3A	Oestrich	15min	WSA Rhein
Groote Lindt	S3A	Goidschalxoord	10min	RWS
Groote Lindt	S3B	Dordrecht	10min	RWS
Sankt Sebastian	S3B	Neuwied	15min	WSA Rhein
Vuren	S3A	Vuren	10min	RWS
Vuren	S3B	Vuren	10min	RWS
Mannheim	S3A	Worms	Designated times	WSA Oberrhein
Spay	S3B	Braubach	15min	WSA Rhein
Spay	S3B	Braubach	15min	WSA Rhein

Table 2.2 provides an overview of the in-situ stations used for validating the altimetric measurements over the virtual stations of this study. The abbreviations listed in the source-column correspond to the following authorities:

- LUBW: Landesanstalt für Umwelt Baden-Württemberg [5]
- RWS: Rijkswaterstaat [6]
- WSA: Wasserstraßen- und Schifffahrtsamt [7]

[5] http://udo.lubw.baden-wuerttemberg.de/public/p/pegel_messwerte_leer
[6] https://www.rijkswaterstaat.nl/water
[7] https://www.gdws.wsv.bund.de/DE/startseite/startseite_node.html

Chapter 3

Preliminary analysis

In the first part of this chapter the performances of the retrackers dedicated to the Sentinel-3 data are evaluated. Moreover, for the geophysical corrections such as atmospheric and target-related ones, we use different sources leading to numerous different realizations of water level timeseries. We refer to these realizations as permutations. Furthermore, we analyze and demonstrate the interesting relationship between SAR waveforms' properties of every measured point and the a-posteriori corrections we obtain from local gauge data. This preliminary analysis not only facilitates the process of understanding Sentinel-3's limitations in inland altimetry, but also serves as a motivation to our methodology towards designing stochastic-based retrackers.

3.1 Slope corrections

In the case of the water body being a river, we consider the fact that, depending on the reach length, the slope of the surface can cause the water level to vary by several centimeters to meters. Therefore, for the validation against in-situ data it is necessary to correct the water levels from altimetry with the influence of the slope. For the three virtual stations, Mannheim, Oestrich-Winkel and Spay, we make use of so-called water level profiles provided by the Wasserstraßen- und Schifffahrtsamt (WSA). Water level profiles are orthometric height measurements of the river's surface recorded on boats navigating several reaches of the Rhine at arbitrary epochs. With a sampling distance of around 100 m these water level profiles provide a fairly dense network and turn out to be very useful in terms of determining a precise slope estimate between the local gauge and virtual station.

Figure 3.1 shows all the water level profiles recorded by the boats in three different reaches of the Rhine River. Three of our virtual stations lie in between these navigated reaches which is particularly practical in terms of determining the slope between the altimetric measurement location and local gauge. With the help of the color coding it is interesting to see the gradual decrease throughout the year with higher water levels in the late winter months which are lowered by a few meters over the summer and even more so in autumn and early winter. Most importantly, the figure demonstrates the necessity to account for the influence of river slope. To correct the slope, we compute the minimal distances from the locations of the water level profiles to the local gauge and to the at-nadir locations of the altimetric measurements, respectively. Of the two corresponding locations of water level profiles, we take the mean water level and subtract the one from the other. This results in a height difference between the local gauge and each location of the altimetric measurements. In the other cases, water level profiles

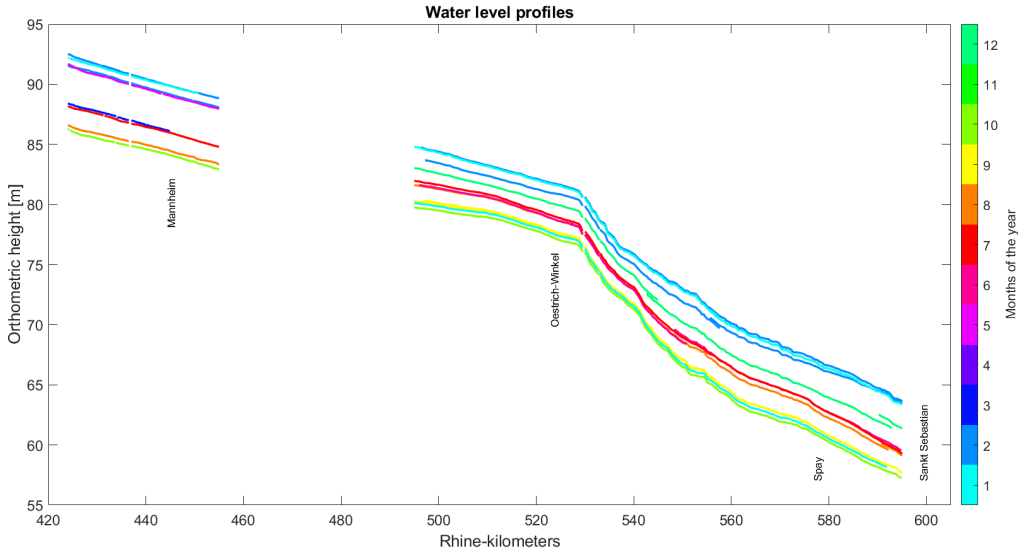

Figure 3.1: *A demonstration of the water level profiles for the three available river reaches*

are not available, for which we simply use a mean slope value from the SWOT River Database (SWORD) [1].

$$\Delta h = s \cdot d \tag{3.1}$$

Equation 3.1 demonstrates the calculation of the height difference of water levels Δh where s is the slope (in m/km) and d is the horizontal distance between the locations of the at-nadir altimetric measurements and the local gauge. In both scenarios the computed height difference is applied to the water levels derived from altimetry.

3.2 Retracker and permutation analysis

In this section, we analyze the retrackers dedicated to the Sentinel-3 mission, as well as the permuted geophysical corrections to the calculated range. Table 3.1 lists all the available options for the geophysical corrections. For the wet and dry tropospheric component, the European Centre for Medium-Range Weather Forecasts (ECMWF) provides corrections based on a model at zero and measurement altitude. Available to the wet tropospheric component are corrections from additional sources such as those determined by the radiometer onboard the satellite. To differentiate between the upper and lower two radiometer-based sources in the table, the latter computes the correction from the brightness temperatures, the Ku-band backscatter coefficient, the sea surface temperature and the lapse rate (decreasing rate of the atmosphere temperature with altitude) while the first is typically used over ocean cases. The composite wet tropospheric correction is computed at the altimeter time-tag from both radiometer and model corrections over areas where the radiometer wet troposphere correction is missing or supposed as invalid

[1] https://www.swordexplorer.com/

due to the proximity of emerged lands or coastal areas. Four options for the ionospheric correction originate from measurements of the altimeter itself. The differences among each other are related to the frequency and operation mode of the altimeter's measurements. The GIM ionospheric correction however was determined and provided by NASA/JPL [2]. The remaining corrections for pole tide and Earth tide solely follow the judgment of Wahr (1985) and Cartwright and Edden (1973), respectively. In table 3.1 the sources in bold letters are assessed as the best based on experts' judgment.

Table 3.1: *A list of all available options for the geophysical corrections*

Wet tropospheric	Dry tropospheric	Ionospheric	Pole tide	Earth tide
ECMWF zero altitude	ECMWF zero altitude	Altimeter cor.: 1 Hz Ku-Band	**Wahr (1985)**	**Cartwright and Edden (1973)**
ECMWF measurement altitude	**ECMWF measurement altitude**	Altimeter cor.: 1 Hz PLRM Ku-Band		
Radiometer cor.: 1 Hz Ku-band		Altimeter cor.: 20 Hz Ku-Band		
Radiometer cor.: 1 Hz PLRM Ku-band		Altimeter cor.: 20 Hz PLRM Ku-Band		
Radiometer cor.(2): 1 Hz Ku-band		**GIM cor. 1Hz**		
Radiometer cor.(2): 1 Hz PLRM Ku-band				
Composite cor.: 1 Hz Ku band				
Composite cor.: 1 Hz PLRM Ku-band				

For simplicity reasons we only visualize numerous timeseries at the Spay (S3B1) virtual station and from the OCOG retracker due to its consistent retrieval of water levels when compared to other retrackers in the course of this study.

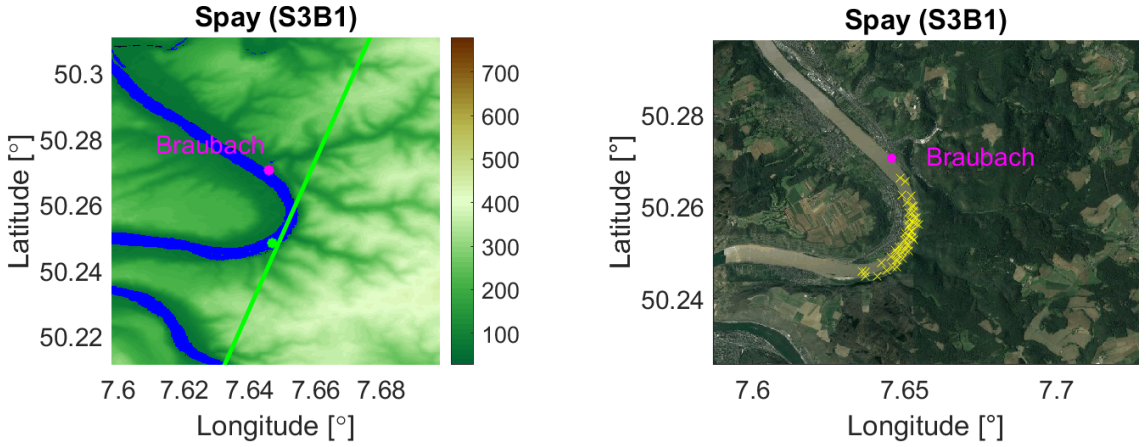

(a) S3B1 groundtrack at Spay

(b) Measurements at Spay

Figure 3.2: *Overview of the groundtrack, at-nadir measurement locations and local gauge at Spay virtual station*

Figure 3.2(a) depicts the Spay virtual station (green dot), the nearest local gauge in Braubach (magenta dot) and the descending Sentinel-3B groundtrack on a digital elevation map. Figure 3.2(b) shows all the at-nadir locations of the altimetric measurements taking place throughout the observation period.

Prior to any analyses, we permute all possible arrangements of geophysical corrections which can be applied to all retrackers. The idea is, despite there being a best permutation of geophysical corrections based on expert-knowledge (bold sources in table 3.1), its water level timeseries does not necessarily yield the best results with respect to referential in-situ data. In figure 3.3 we plot all possible permutations (gray dashed lines) of the OCOG-retracker, which in total

[2]Jet Propulsion Laboratory

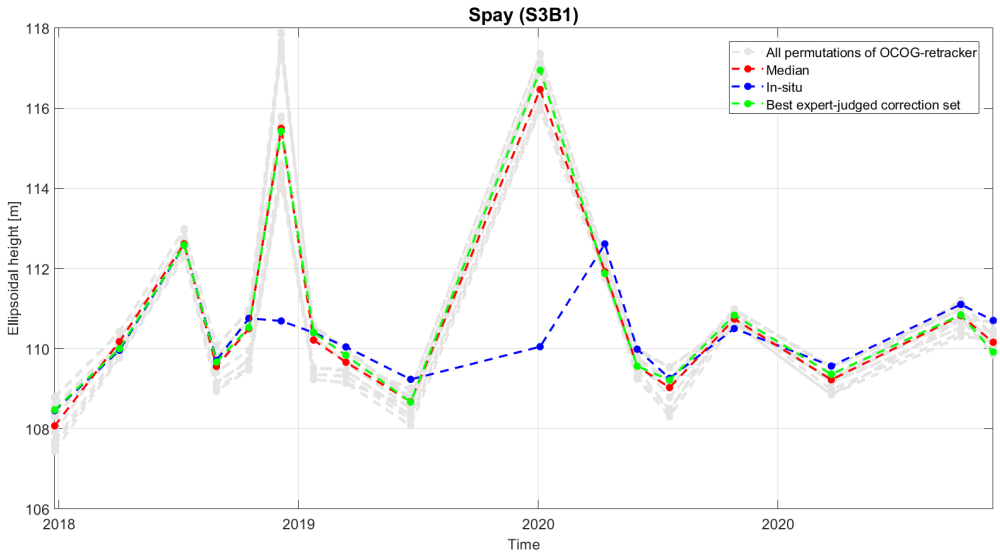

Figure 3.3: *A comparison of in-situ data against several realizations of OCOG-retracked S3B- timeseries*

amount to 48 different realizations. Among them is a permutation whose corrections are based entirely on experts' judgment (green dashed lines).

The blue dashed lines visualize in-situ data acquired at the Braubach gauge a bit further downstream the Rhine River. In addition, we calculate the median water level at every epoch taking into account the high-rate samples of all permutations. In each and every epoch, the median water level may come close to different permutations of geophysical corrections. Nonetheless, we determine the permutation which the median timeseries comes close to the most. To this end, we compute the RMSE between the median timeseries and all permutations of the OCOG-retracker. Based on this metric, the median timeseries most closely resembles the permutation with the following sources for geophysical corrections:

- **Retracker**: OCOG
- **Wet tropospheric**: Radiometer correction(2): 1 Hz Ku-band
- **Dry tropospheric**: ECMWF at zero altitude
- **Ionospheric**: GIM correction: 1 Hz
- **Pole tide**: Wahr (1985)
- **Earth tide**: Cartwright and Edden (1973)

An interesting first finding resulting from figure 3.3 and other river stations examples, respectively, is that the median water level over all permutations nearly resembles the best expert-judged permutation of geophysical corrections. They both show similar behaviors and are only offset to one another by few decimeters at the most. When comparing the sources for the geophysical corrections of each, it becomes clear that the existing differences can be traced back to the wet and dry tropospheric component. For the most part both timeseries are in agreement with the behavior of the in-situ data, likewise revealing differences of up to only a

few decimeters. There are two noticeable exceptions to this statement however, visible in the two largest peaks. At these epochs, in addition to all other realizations, the permutation based on experts' judgment and the median timeseries fail in coming close to the true water level by several meters. As a matter of fact, these offsets amounting to around five and six meters, respectively, must be thoroughly investigated. The width of the gray envelope set up by all the possible permutations demonstrates how permuting geophysical corrections affects the final timeseries. Variations are visible, but remain rather small. From visual inspection, the variation among the permutations of this retracker amount up to approximately three meters at the most. When inspecting the offset between the two largest peaks and the in-situ data however, we can exclude error sources from the geophysical corrections. Such differences of five and six meters in water levels are a result of range errors, in other words from retracking. For this reason, improving retrackers' performances is a crucial measure to reach appropriate altimetry results in every given epoch. This problem will be further emphasized in the continuation of this study.

To go into more detail on the overall performance of retrackers and the applied geophysical corrections, we consider all permutations, this time including those of the remaining retrackers as well. The entirety of these realizations is compared to the local gauge data and assessed based on the following metrics:

- Correlation coefficient (CC)
- Root mean squared error (RMSE)
- Relative bias: RBias $= \frac{\sum_{t=1}^{T}(R_{t,obs} - R_{t,est})}{\sum_{t=1}^{T} R_{t,obs}} = 1 - \frac{\overline{R}_{est}}{\overline{R}_{obs}}$
- Kling-Gupta-Efficiency: KGE $= 1 - \sqrt{(CC-1)^2 + (\beta-1)^2 + (\gamma-1)^2}$

$$\beta = \frac{\overline{R}_{est}}{\overline{R}_{obs}} \text{ and } \gamma = \frac{\sigma_{R_{est}}/\overline{R_{obs}}}{\sigma_{R_{obs}}/\overline{R_{est}}}$$

- Nash-Sutcliffe-Efficiency: NSE $= 1 - \frac{\sum_{t=1}^{T}(R_{t,obs} - R_{t,est})^2}{\sum_{t=1}^{T}(R_{t,obs} - \overline{R}_{obs})^2}$

The correlation coefficient provides an understanding of the level of common information content between the in-situ measurements, R_{obs}, and the altimetry-derived water levels R_{est}. It is, however, insensitive to the amplitude and mean value (Lorenz et al., 2014). The RMSE describes the square root of the variance of the residuals. It quantifies an absolute measure of fit between the referential in-situ and altimetric data. In principle, it describes how close the two timeseries are to each other. The RBias delivers information on the relative difference between the long-term mean of both the in-situ data and the altimetric data. The KGE combines statistical quantities such as the correlation, bias and variability in a balanced manner and has been widely used for calibration and evaluation of hydrological models in the recent past (Liu, 2020). Often considered as similar to KGE is the NSE. It is very sensitive to the overall agreement between the in-situ and altimetry-derived data, in particular taking into account the phase, amplitude and mean. When these parameters are in full agreement with each other, the NSE equals to 1. From here it ranges downward to -∞ (Lorenz et al., 2014). Following the

exemplary scenario at Spay (figure 3.3) we determine the best-performing out of the 240 permutations based on these five metrics and plot them against the in-situ data and against each other (see figure 3.4).

Table 3.2: *Best permutations of Spay example*

Metric	Quantity	Retracker	Wet tropo.	Dry tropo.	Iono.	Pole tide	Earth tide
CC	0.9539	Ocean	Rad. cor.(2)	ECMWF meas. alt.	GIM	Wahr (1985)	Cartwright and Edden (1973)
RMSE	0.3157	Ocean	Rad. cor.(2)	ECMWF zero alt.	GIM	Wahr (1985)	Cartwright and Edden (1973)
RBias	0.0001	OCOG	ECMWF zero alt.	ECMWF zero alt.	SRAL	Wahr (1985)	Cartwright and Edden (1973)
KGE	0.9389	Ocean	Rad. cor.	ECMWF meas. alt.	GIM	Wahr (1985)	Cartwright and Edden (1973)
NSE	0.8988	Ocean	Rad. cor.(2)	ECMWF zero alt.	GIM	Wahr (1985)	Cartwright and Edden (1973)

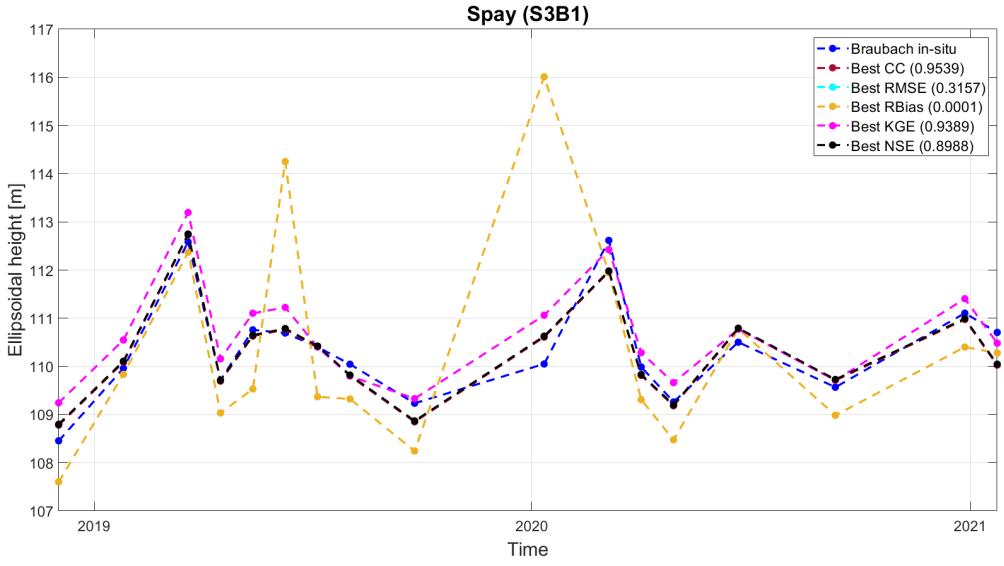

Figure 3.4: *Best performing permutations at Spay virtual station*

Simply from a visual inspection of figure 3.4 it becomes noticeable that, in this scenario, these four of the five realizations outperform the vast majority of the OCOG permutations and the median water level timeseries in figure 3.3. The aforementioned range error from OCOG-retracking clearly does not make an appearance among the other four permutations of figure 3.4. The permutation resulting from the best relative bias (yellow) shows a similar behavior as seen in figure 3.3, which does not come to our surprise since it corresponds to an OCOG-permutation. It is indeed unexpected however, to see this permutation assessed as the best in terms of its relative bias to the in-situ data as it shows two big outliers and a general offset to all other timeseries. After further investigation, it could be concluded that this is a rather coincidental outcome in which the long-term mean of both the local gauge data and the best permutation by relative bias are nearly equal. To figure out the reason behind these considerable outliers, we focus on the component we presume to be the origin, namely the retrackers.

To this end, figure 3.5 visualizes the Ocean- and OCOG-retracking gates in the waveform for the epoch in which the huge outlier (near 2020 mark) occurs. This investigative waveform-level approach will be further elaborated and demonstrated in the following section and chapter. Nonetheless, what the figure demonstrates is the fact that the two retracking gates are

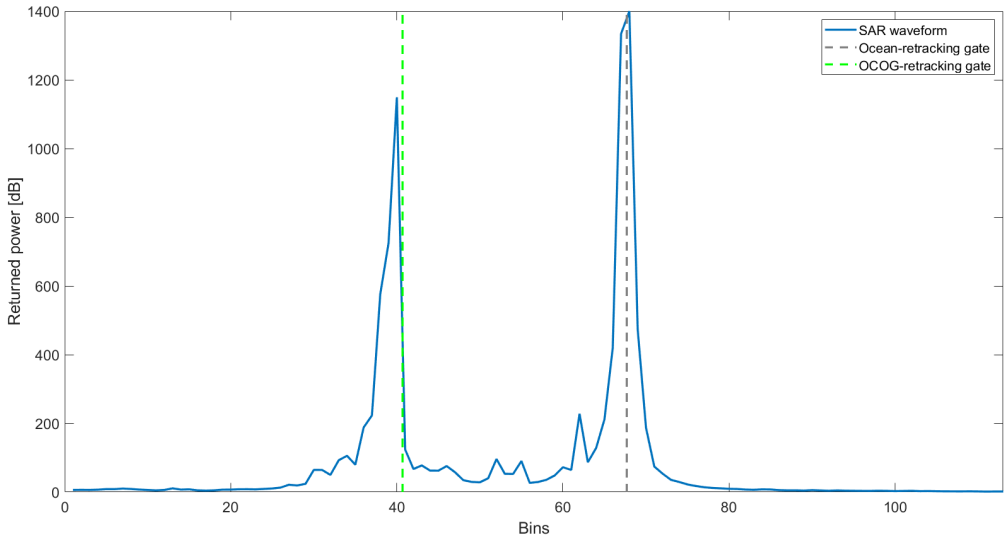

Figure 3.5: *A visualization of the Ocean- and OCOG-retracking gates on a waveform level*

nearly 27 bins apart. This is a critical difference, as when converted into meters this value corresponds to around 12.6 m. To be noted at this point is that all timeseries in figure 3.3 and 3.4 are downsampled ones. Therefore, the water levels of each epoch represent the median of all measurements during the satellite's bypass. In this case, there is one other measurement which took place in the same epoch. Herein though, the Ocean- and OCOG-retrackers are nearly in agreement in terms of the computed retracking gates, and are subsequently only offset to one another by less than 1 bin on a waveform level. Consequently, for the outlier-epoch the median (effectively the mean in this case) of the two offsets between the retracking gates is equal to around 13.5 bins. Metrically speaking, this is an offset of around 6.3 m which corresponds to the offset of the outlier-epoch visible in figure 3.4. Interestingly, the best permutations based on the remaining metrics are all derived from the Ocean-retracker. Table 3.2 lists the arrangement of geophysical corrections to make up the corresponding permutations.

From table 3.2 and figure 3.4 it becomes noticeable that, for this example, the best RMSE- and NSE-permutations are the same. Also, the best permutation in terms of the correlation coefficient only differs from those two by the wet tropospheric component, in which the ECMWF model at measurement altitude is chosen. Based on experts' judgment, this exact correction is considered the most suitable for the wet and dry tropospheric component. Therefore, it is quite interesting to see that the ECMWF model at measurement altitude only occurs twice in table 3.2. For the wet tropospheric component, the radiometer-determined corrections mainly prove to be the best in the given example. SRAL simply signifies that the correction for the ionospheric component is determined by the altimeter itself.

As these findings only represent one scenario, we conduct this investigation over a variety of river and lake stations listed in chapter 2 to decide whether there is an evident winner among the retrackers and applied sets of geophysical corrections. Therefore, we again determine the best-performing permutations based on the metrics above and with respect to the in-situ data. To draw a conclusion on the overall winner, we record the best permutations determined by all five metrics and repeat this process for all river and lake cases. Hereinafter, we count the

occurrences of each unique permutation in the recordings and define the best as the highest number. Based on this approach the overall best-performing permutations for the river and lake cases can be seen in table 3.3.

Table 3.3: *Overall best performing permutation for river and lake cases*

	Retracker	Wet tropo.	Dry tropo.	Iono.	Pole tide	Earth tide
Rivers	OCOG	Rad. cor.(2)	ECMWF zero alt.	SRAL	Wahr (1985)	Cartwright and Edden (1973)
Lakes	OCOG	Rad. cor	ECMWF zero alt.	SRAL PLRM/GIM	Wahr (1985)	Cartwright and Edden (1973)

There are some notable takeaways from these assessments. Firstly, as briefly mentioned, the best expert-judged set of geophysical corrections, and in fact the choice of the retracker itself, do not necessarily produce the water level timeseries with the least bias with respect to the local gauge data. For the entirety of lake and river cases, the expert-judgment for the choice of the retracker is confirmed (OCOG). The geophysical corrections however, differ from the experts' choice for the most part. Secondly, from figures 3.3 and 3.4, as well as from table 3.2 one can tell the important role geophysical corrections play in water level retrieval. Height differences between different permutations amount to a few meters in some epochs which can be traced back to the choice of the permuted correction sets. In essence, corrections for dry tropospheric range delay of the radar pulse are the most crucial due to their relatively high magnitude of up to 2.3 m. To a lesser extent, the corrections for the wet tropospheric and ionospheric range delay are also important counting magnitudes up to several decimeters. Consequently, these corrections are the most permuted among all the realizations. The remaining corrections for pole tide and Earth tide follow the judgment of Wahr (1985) and Cartwright and Edden (1973), respectively.

3.3 Reverse retracking approach

In the previous section, we demonstrated, among other aspects, that the choice of the retracker and source for the geophysical corrections plays a key role in the retrieval of correct water levels. Permuting the arrangement of these delivers a unique realization of water levels (see gray dashed lines in figure 3.3). In principle, this means for each permutation there is a unique offset between its determined water level and the true value from the local gauge data. In the continuation of this study, we refer to the height differences between the altimetry-derived and in-situ water levels as a-posteriori corrections.

In this section, we perform a reverse retracking approach to better understand how these a-posteriori corrections could be applied on a waveform level and their relationship to the waveform's properties of the same measurement epoch. At this point it must be stated that we assume, for one, the a-posteriori corrections to be legitimate and, for another, the geophysical corrections to be error-free. That being considered, we solely project the a-posteriori corrections onto the range. This approach can be seen as reverse retracking in the sense that in-situ data is available and can be used to correct the initially determined retracking gate in the waveform. The main idea is to determine the offsets that exist between the altimetric and the in-situ time series. For this matter, sampled altimetric data points must correspond to in-situ data points of approximately the same epoch or else one can not assume the offset to be true. Therefore, the in-situ data is linearly interpolated not only to the union of both time series, but also with

respect to the mean altimetric acquisition times of each cycle. Consequently, for any given cycle in the altimetric time series, there are several sampled points that now can be compared to individual interpolated in-situ data points of the same epoch.

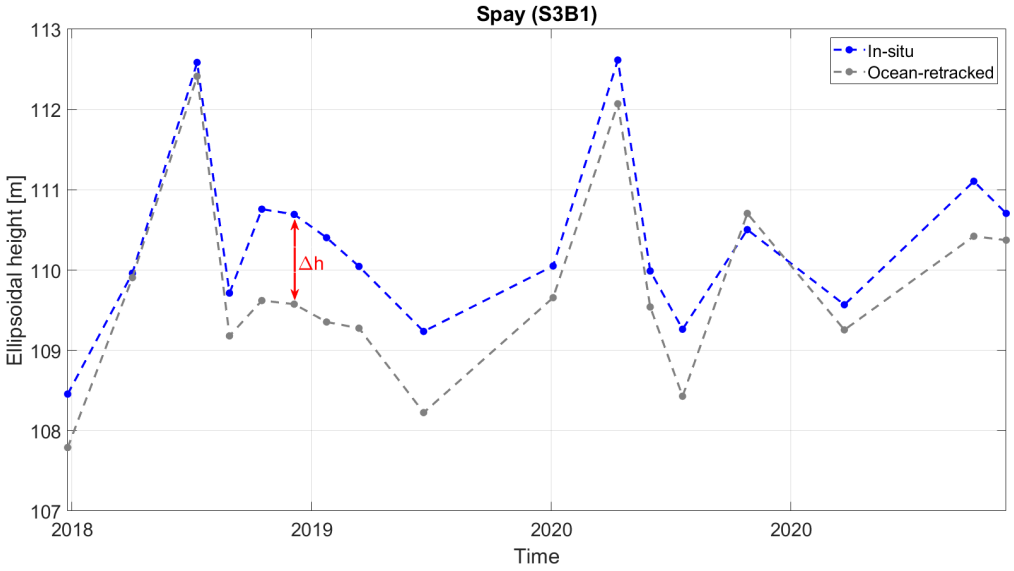

Figure 3.6: *Demonstration of individual height differences between in-situ and altimetric data*

Figure 3.6 shows a considerable example of the height differences, indicated by the red double-arrow. Since in most cases, nearby in-situ data is available and offers a high sampling rate of 15 minutes, we can appropriately interpolate to the timestamps of the altimetric timeseries and compare each measurement to the gauged data. Now that we have correctly obtained the differences between the water levels of altimetric and in-situ time series, the next step is to convert them into bins.

$$\Delta b = \frac{2\Delta h}{t_{pulse} \cdot c} \tag{3.2}$$

The conversion of the aforementioned differences into bins (see equation 3.2) is a necessary measure in order to regard them as corrections on a waveform level. In equation 3.2 Δh is the difference in water levels of mutual epochs, whereas t_{pulse} and c represent the travel time of the pulse and the speed of light, respectively. Figure 3.7 demonstrates the a-posteriori correction to the Ocean-retracking gate for the corresponding epoch highlighted in figure 3.6. In this example the Ocean-retracking gate is situated slightly behind the main peak of the waveform. The a-posteriori corrected range gate however, is placed right at the beginning of the waveform's leading edge. Typically, a range gate as such is very reasonable for water level retrieval in satellite altimetry. To what extent the a-posteriori corrections yield the correct bin for water level retrieval, or in other words the probability for each bin of the waveform, is central to this study and will be further discussed in chapter 4.

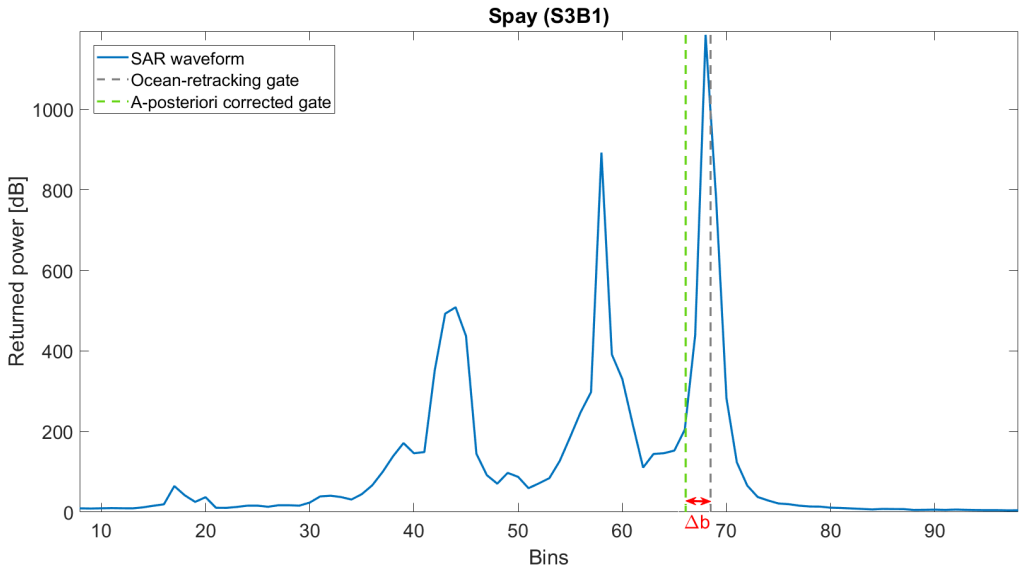

Figure 3.7: *A-posteriori correction from in-situ data applied on waveform level*

3.4 Analysis of the a-posteriori corrections and waveform properties

As previously discussed, there is an offset between altimetric measurements of the water level and the corresponding in-situ data point which is unique to each epoch and especially to every single permutation (Δb on a waveform level). To better understand the magnitude and general behavior of the a-posteriori corrections (Δb) with respect to the waveform's properties in the same epoch, we abstract Δb into statistical parameters. These are computed for each measurement of a satellite's bypass across all permutations of a specific retracker. In other words, for each retracker the amount of data points resulting from the process of abstracting, corresponds to the number of all epochs (see figures 3.11 to 3.12). The statistical parameters we compute are the following:

- **Standard deviation** of a-posteriori corrections (Δb)

  Generally, the standard deviation is a parameter describing the variation or dispersion of data, in particular from its mean value. In this case, the standard deviation of the a-posteriori corrections represents their stability across all permutations of a retracker for a given measurement index in the satellite's bypass.

- **Median** of a-posteriori corrections (Δb)

  The median can be described as the "middle" value of a data set. It basically separates the higher half of the data from the lower and is insusceptible to large outliers. In our analysis the median is useful to represent the overall performance of the retracker. As permutations of the same retracker will only show small variations among each other but follow similar trends, the median a-posteriori correction therefore rather focuses on the retracker itself.

Furthermore, we compute the following waveform properties:

- **Peakiness** of the waveform

  Peakiness gives an indication of the waveform shape (Boy et al., 2021) and, in principle describes the sharpness of the signal. It is defined as the ratio between the maximum of the signal and the sum of power over all bins, which can be seen in equation 3.3. The higher the peakiness, the sharper the waveform and vice versa.

$$\text{Peakiness} = \frac{Max(W_i)}{\sum_{i=1}^{n} W_i} \tag{3.3}$$

  where W_i is the power corresponding to the i-th bin and n is the number of measured data within the entire waveform.

- **Kurtosis** of the waveform

  Kurtosis describes the combined weight of a distribution's tails relative to the center of the distribution and thus is an indication for the shape of a probability distribution. Typically, kurtosis is computed as follows:

$$\text{Kurtosis} = \frac{\frac{1}{n}\sum_{i=1}^{n}(W_i - \overline{W})^4}{\left(\frac{1}{n}\sum_{i=1}^{n}(W_i - \overline{W})^2\right)^2} \tag{3.4}$$

  where $\overline{W}$ represents the mean value of all sampled waveform powers.

- **Maximum power** of the waveform

  Maximum power describes the highest value of power in the waveform and therefore also the main peak value itself.

- **Relative bias** between sinc^2 and the waveform

  Boy et al. (2021) suggest that a waveform with a peakiness ratio between 0.5 and 1 resembles the form of the sinc^2 function. We further investigate this statement and use the relative bias between the waveform itself and sinc^2 as yet another waveform property. In order to accurately fit the function to the waveform, it is shifted by the bin-value of the waveform's peak in x-direction whereas the amplitude of the function simply corresponds to the maximum value of the waveform.

  Figure 3.8 demonstrates how a sinc^2 function is fitted to an exemplary SAR waveform. Although indiscernible from the figure, both peaks coincide and establish an appropriate basis for the aforementioned relative bias (see equation 3.5).

$$\text{RBias} = \frac{\sum_{i=1}^{n} W_i - \text{sinc}^2(i)}{\sum_{i=1}^{n} \text{sinc}^2(i)} \tag{3.5}$$

  Equation 3.5 describes the calculation of the relative bias between the sinc^2 function and the SAR waveform. The summed difference between the waveform and the sinc^2 function

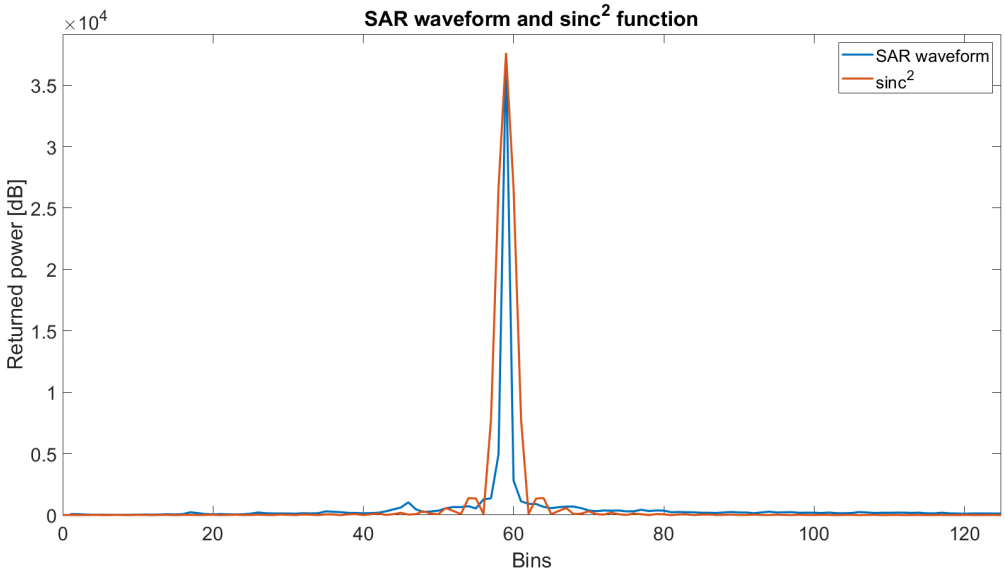

Figure 3.8: *Exemplary SAR waveform and corresponding sinc^2 function*

in the numerator is the key element of this equation. When both signals are in high-level of agreement with each other, the relative bias becomes significantly small due to the division of the sinc^2 signal. Conversely, when both signals deviate considerably to each other, the numerator is larger and the relative bias likewise. We therefore expect waveforms of higher aforementioned peakiness to reveal low relative biases to the sinc^2 signal.

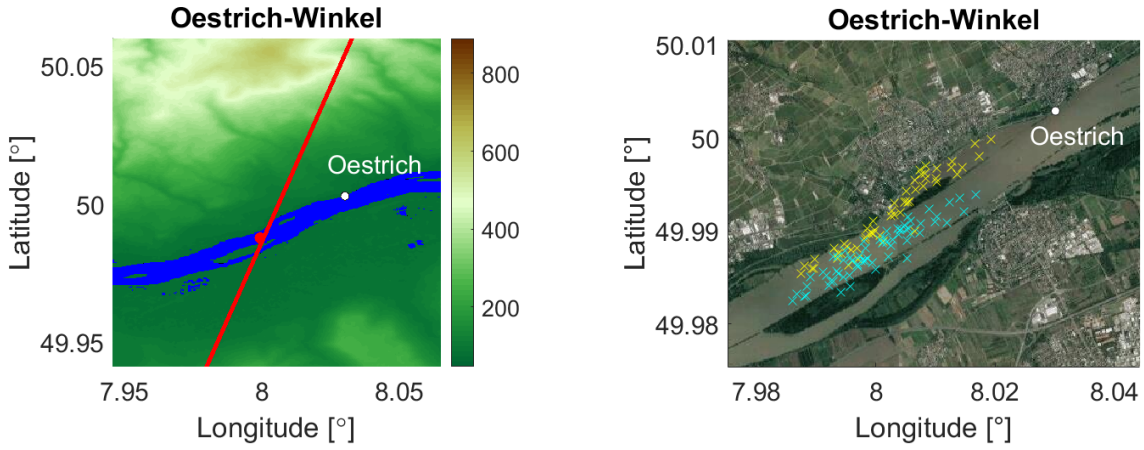

(a) S3A groundtrack at Oestrich-Winkel

(b) Measurement near river bank and middle

Figure 3.9: *Overview of the groundtrack, local gauge and at-nadir measurement locations at Oestrich-Winkel virtual station*

Figures 3.10 to 3.12 provide a demonstration of the link between the mentioned parameters for each retracker and waveform properties. Moreover, some of the scatter plots are between different waveform properties themselves to better comprehend their characteristics (figure

3.12 right side). All figures show a scatter plot for measurements over the side of the water body (here near the river bank) and for ones over the middle. In this case, we visualize the characteristics derived from the Sentinel-3A level-2 data at the Oestrich-Winkel virtual station. Figure 3.9(a) depicts the Oestrich-Winkel virtual station (red dot), the nearest local gauge (white dot) and the descending Sentinel-3A groundtrack on a digital elevation map. In figure 3.9(b) we differentiate between altimetric measurements near the river banks (yellow markers) and towards the middle of the river (cyan markers) since the following analysis is conducted in the same manner. Due to the crossing scenario of the S3A groundtrack at Oestrich-Winkel we receive a decent amount of information for presentation purposes. Following the plots limited to the Oestrich-Winkel case, we focus on the entirety of all virtual stations and visualize the results in a comparable overview (figures 3.13 to 3.20).

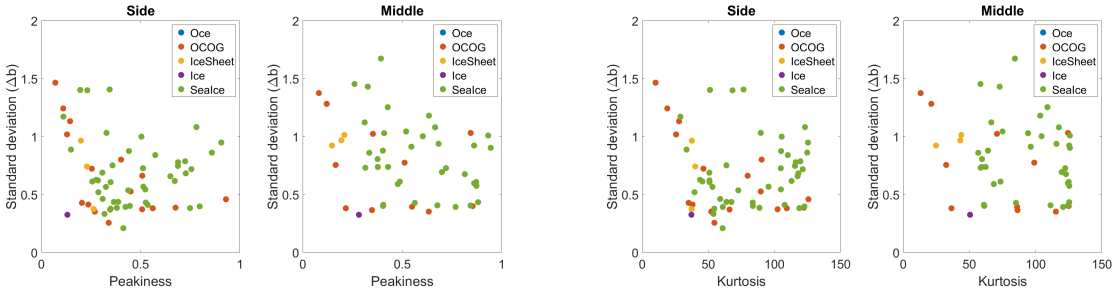

Figure 3.10: *Scatter plots between peakiness/kurtosis and the standard deviation of a-posteriori corrections*

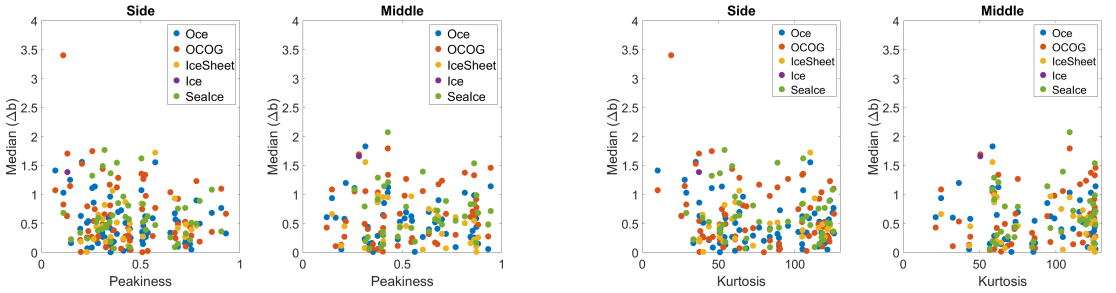

Figure 3.11: *Scatter plots between peakiness/kurtosis and the median of a-posteriori corrections*

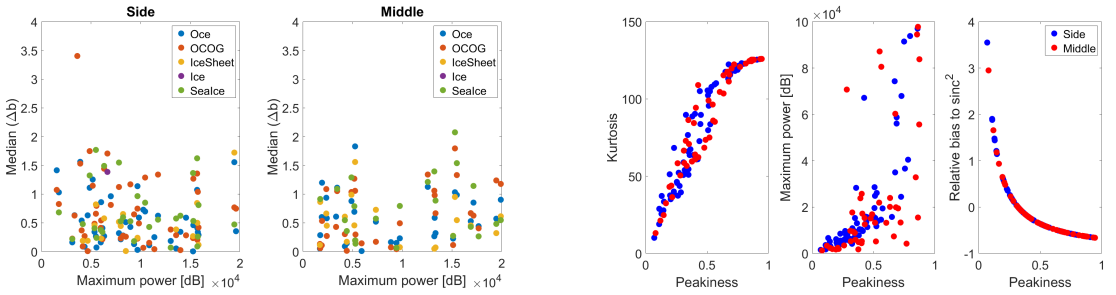

Figure 3.12: *Scatter plots between maximum power and median of a-posteriori corrections (left) and other waveform properties against each other (right)*

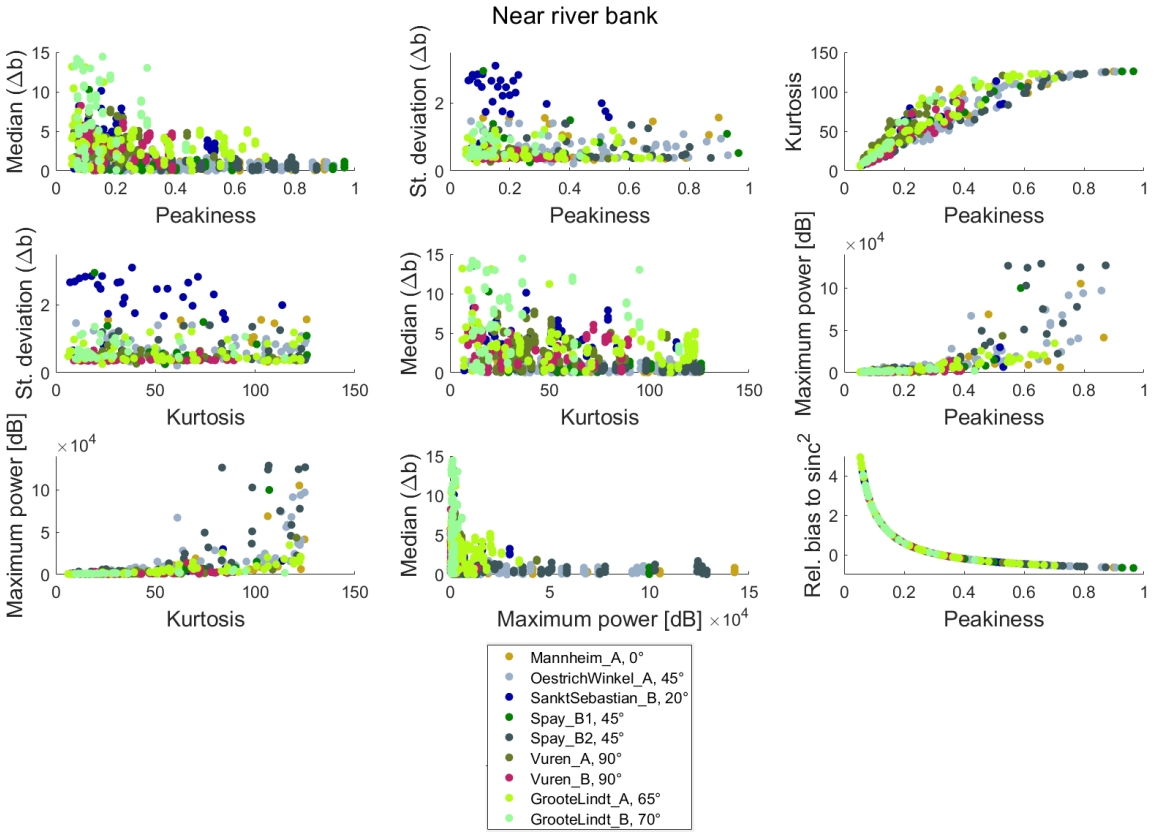

Figure 3.13: *Addressed statistics for all cases near the river bank*

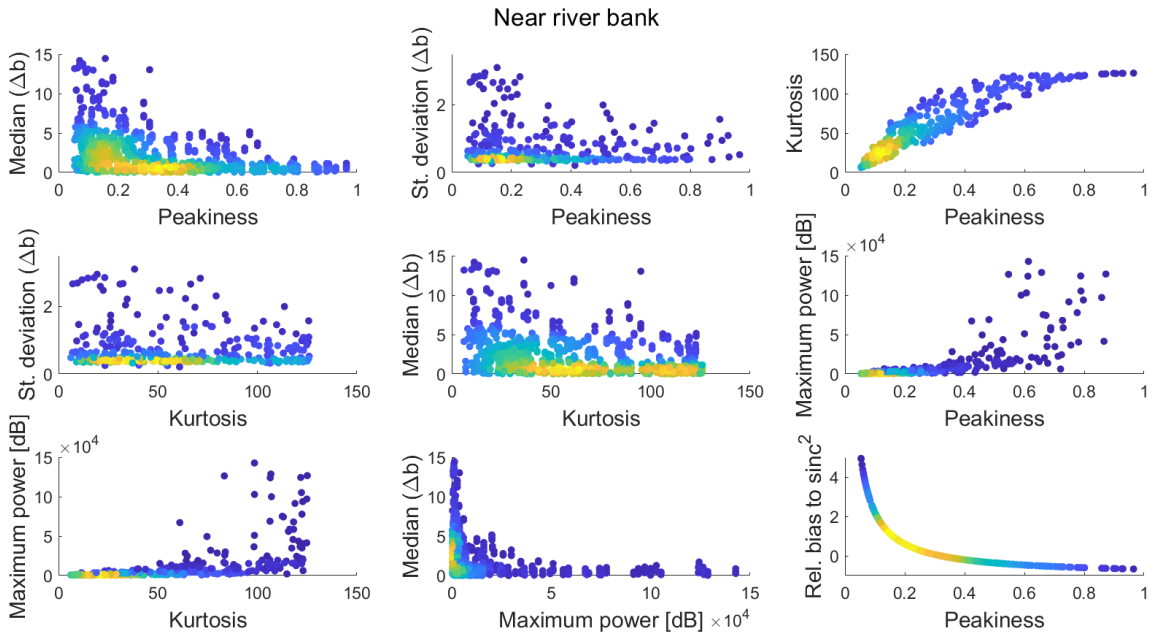

Figure 3.14: *Density plot for all cases near the river bank*

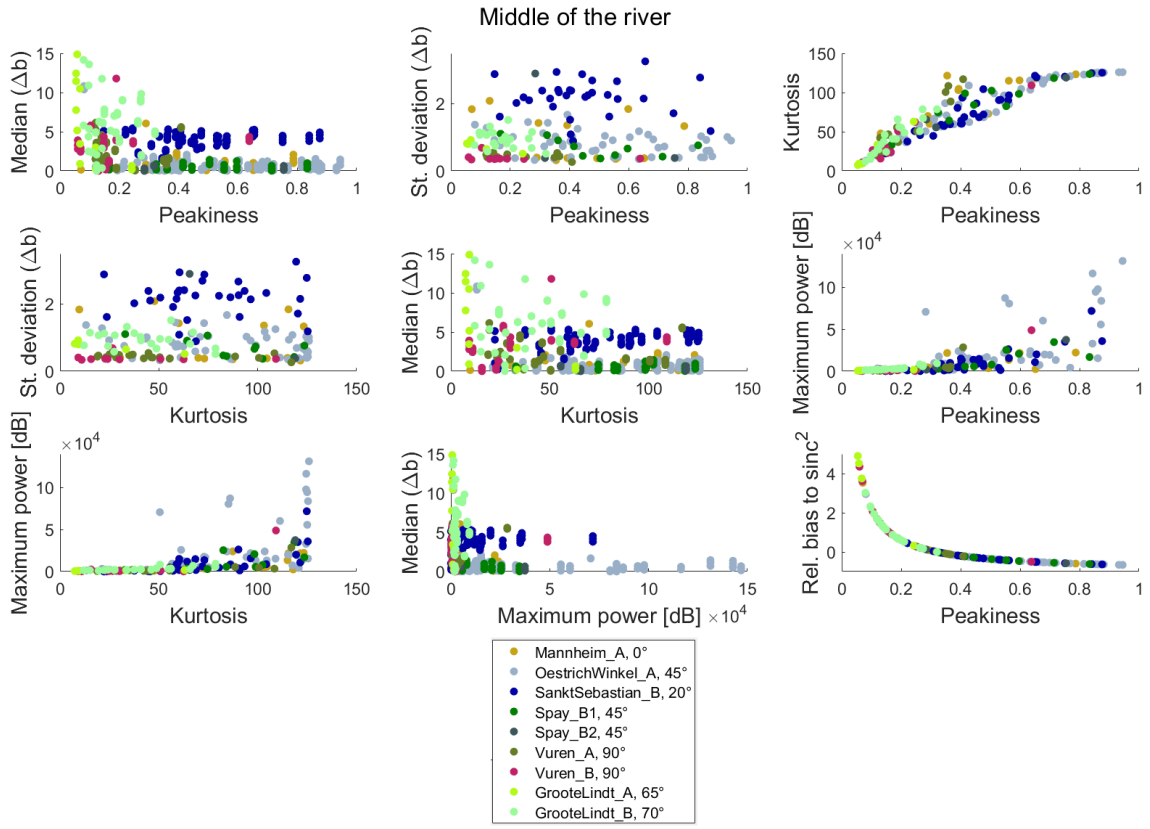

Figure 3.15: *Addressed statistics for all cases in the middle of the river*

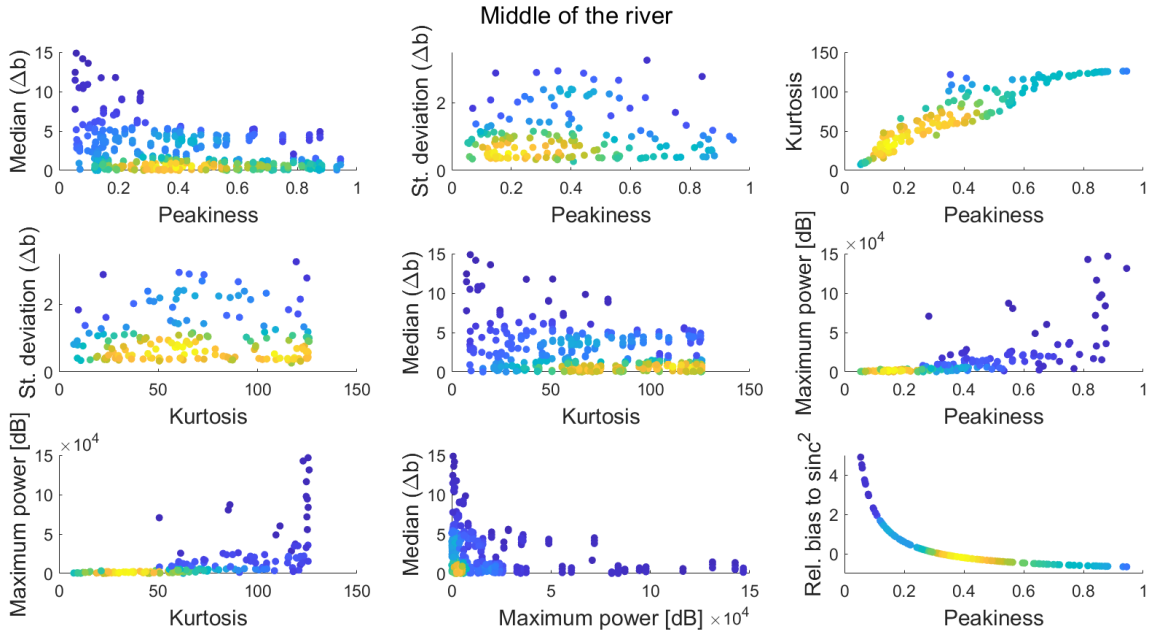

Figure 3.16: *Density plot for all cases in the middle of the river*

Figure 3.10 shows scatter plots for peakiness and kurtosis against the standard deviation of the a-posteriori corrections. When comparing the left and right subplots, a very similar behavior in the distribution of data points becomes noticeable. This, in general, is an early indicator for a positive correlation between the peakiness and kurtosis of a waveform. From closer inspection, there is an interesting arrangement of data points in all subplots, namely a constant alignment of which around a standard deviation of 0.4. This especially persists throughout the entire peakiness/kurtosis range. Since the retracking gate is a constant quantity among permutations of the same retrackers, we assume this systematic behavior to occur from this source. In addition, as previously discussed, the standard deviation of a-posteriori corrections represents their stability across all permutations. Therefore, this systematic alignment essentially demonstrates a very specific stability around the value of 0.4. The distribution of the remaining data points hardly follows any certain pattern. To a lesser extent some higher standard deviations do occur in lower peakiness and kurtosis ranges, in particular for the side of the river. Herein, it becomes slightly noticeable that there is a concentrated portion of data points. This finding is emphasized in the density plot of figure 3.14 taking into account all river stations. Hereby, the yellow color-coding represents the highest density of data points while the dark blue color-coding stands for the lowest density. The respective density plots for the side of the river reveal a downward behavior in which higher standard deviations of the a-posteriori corrections mainly occur in lower ranges of peakiness and decrease throughout the x-axis. In the middle of the river however (figure 3.16), this decreasing trend is not as prominent as near the river bank. This comes to show that waveforms returned to the altimeter from the middle of the river are, for one, peakier and, for another, show smaller standard deviations of the a-posteriori corrections. The previously addressed systematic alignment of data points with constant standard deviation also occurs in all plots which we attributed to the mutual range gate of specific retrackers.

The color-coding in figures 3.10 to 3.12 categorizes the five available retrackers. However, those plots involving the standard deviation of the a-posteriori corrections do not visualize data points corresponding to all retrackers. Initially, we expected all data points from the five retrackers to coincide due to their exact same sets of geophysical corrections, making the color-coding in figure 3.10 rather questionable. After close inspection, it could be concluded that, as a matter of fact, they all do coincide. The different colors can be simply traced back to the incapability of some retrackers to determine a retracking gate in the given waveform. Only the Ice-retracker delivered a unique data point in this case as it retrieved just one water level in the given observation period where all other retrackers failed to.

By determining the median a-posteriori corrections, we initially expected a visual representation of retrackers' performances since the small variations to the water levels from geophysical corrections would not impact the offset between altimetry-derived and true water level very much. Figure 3.11 depicts side by side the peakiness and kurtosis of waveforms against their respective median a-posteriori corrections. It is rather difficult to assume any retracker-related behaviors. For one, the median a-posteriori corrections of the Ocean and IceSheet retracker tend to remain the lowest within the given peakiness/kurtosis range whereas those of the OCOG and SeaIce retrackers partly show higher median bins. For another, the corrections of the Ice retracker are hardly represented at all due to its incapability to determine a retracking gate for this case scenario.

When comparing the scatter plots in figure 3.11 it becomes noticeable that for the vast majority of peakiness/kurtosis ranges the median correction remains under 2 bins corresponding to

0.94 m. The plot for the side of the river shows a higher density in lower peakiness ranges whereas the middle of the river produces rather evenly distributed data points. This however, can not be said about the scatter plots involving kurtosis. Herein, the lower ranges are nearly equally conglomerated for the side of the river and even less so for the middle of the river although we expect the opposite. There even seems to be a slight upward trend, implying that the higher waveform's kurtosis gets, the larger the a-posteriori median corrections become. This finding rather opposes our previous understanding. However, under consideration of the measurements' locations over the middle part of the river, it is possible that this behavior is related to the proximity to a river island or other disturbing surface elements (see figure 3.9(b)). The respective density plots for all river stations in figures 3.14 and 3.16 once again reveal the overall behavior of these parameters scattered against each other. For the most part, they oppose the behavior of the Oestrich-Winkel case and show a clear downward trend with higher a-posteriori corrections for low peakiness values and a decrease the closer peakiness gets to 1. The role of the measurement index within a satellite's bypass also is evident from the density plots. Near the river bank, highest accumulations of median a-posteriori corrections are found in significantly lower ranges of peakiness and kurtosis than over the middle part of the river. This confirms our presumption that less peaky and more noisy waveforms originate from the side of the river as opposed to the middle part. Lastly, comparing the right and left hand sides of figure 3.11 it seems that plotting kurtosis against the median a-posteriori correction demonstrates a rather misleading behavior for this scenario. As mentioned, it is quite likely that the upward distribution of data points in the middle of the river is related to the nature of that specific reach of the river. On the other hand though, one can conclude that kurtosis does not represent crucial waveform characteristics as well as the previously discussed peakiness.

Plotting the maximum power of waveforms against the median a-posteriori corrections is yet another interesting analysis to support similar findings to the above. In the Oestrich-Winkel case of figure 3.12, for the two sampled locations over the Rhine River near Oestrich-Winkel the behavior of both scatter plots does not present many notable takeaways. To mention one though, the occurrence of data points on the left hand side is rather shifted toward lower power values. This implies that near the river banks waveforms' peaks tend to be smaller in amplitude and somewhat cause median a-posteriori corrections to be high. Then again, we expect peakier waveforms to show high values in maximum power and at the same time smaller a-posteriori corrections. In the density plots of figures 3.14 and 3.16 the respective plot meets our expectation even more than for other parameters. The main difference between the side of the river and its middle part is the vertical extent of the highest accumulation of data points. Near the river bank the turquoise to yellow color-coding in very low maximum power ranges takes the shape of a vertically oriented oval. Over the middle part of the river, this high accumulation rather corresponds to a filled circle yielding smaller a-posteriori corrections than its counterpart in the low maximum power ranges.

Now, we refer to the three mentioned waveform properties and their relationships toward each other (figure 3.12 right hand side). Therefore, the scatter plots in the addressed figure and the following representing the entirety of all river stations do not take the a-posteriori corrections into account, but better demonstrate the characteristics of the waveforms returned from the two sampled locations over the river. As addressed earlier, peakiness and kurtosis maintain a near-linear relationship with each other. In this case, it is more important to mention the occurrence of data points in lower peakiness and kurtosis ranges for both measurement indexes in the satellite's bypass. To this end, we analyze the density plots of the two. Comparison shows that the highest density (yellow color-coding) of data points is shifted more toward

the lower peakiness and kurtosis ranges for river bank scenarios than for the middle of the river. For reference, when we inspect the subplot of peakiness against kurtosis for both river-scenarios, we detect a small accumulation hardly exceeding a peakiness value of 0.2 and a kurtosis value of 50 near the river bank. The counterpart in the middle of the river, reveals a high accumulation for both indicators slightly exceeding a peakiness value of 0.4 and kurtosis value of approximately 75, respectively. This further underlines the previous statement that near the river banks waveforms are typically noisier and less peaky.

Another scatter plot among waveform properties is demonstrated in the middle of figure 3.12 (right side). Among both color-codings it becomes noticeable that the relationship between peakiness and maximum power behaves almost exponentially. However, the peakier the waveform is, the less data points there are. The highest concentration of data points is in the lower range of peakiness and maximum power. This is even more noticeable in the plot for returned waveforms near the river bank which goes along with our expectations and previous findings. In the density plots, the highest data accumulations also differ from one to another in their horizontal extent, when comparing the figures for the side and middle part of the river. Near the river bank, data points tend to conglomerate in lower ranger of peakiness and thus maximum power as opposed to over the middle.

At last, we scatter peakiness against the relative bias of the waveform to the sinc^2 function (figure 3.12, right hand side). Both the side and the middle of the river reveal an exponential curve in which the scattered data points hardly deviate perpendicular to the trend. The figure demonstrates that the peakier a waveform gets, the lower the relative bias becomes. However, toward very high peakiness values, the relative bias overshoots 0. This can be traced back to the fact that peakiness of 1 corresponds to a dirac signal. Since the relative bias is closest to zero the more the waveform resembles the sinc^2 function, and not the dirac signal, we see a deviation in opposite direction between the waveform and the fitted function. Somewhat difficult to discern from the figure, the density of scattered data points shows an accumulation in lower ranges of peakiness for the side of the river. However in this case, these correspond to near-zero relative biases and therefore not meeting our expectations. For the middle part of the river, the data points are rather distributed across the curve. From inspecting the density plots, the relative bias clearly yields accumulated near-zero values around an 0.4-centered peakiness range for the middle of the river whereas the accumulation near the river bank is centered around a peakiness value of 0.2 and relative bias of 1.5.

To briefly address the behavior of scattered data points related to specific virtual stations, we refer to figures 3.13 and 3.15. Herein, each color represents a different virtual station. The angle included in the legend indicates the crossing angel of the satellite's groundtrack with respect to the water body. From both the figures near the river bank and over the middle of the river, one can discern that the Sankt Sebastian and the two Groote Lindt cases, reveal the highest median and standard deviation of a-posteriori corrections compared to the others. To a lesser extent, this also applies to both Vuren cases. From our study, we can confirm that in these specific cases there is a considerable bias between the altimetric water level and in-situ timeseries which comes to explain this finding. This bias is assumed to be related to an imprecise application of slope corrections. As visualized in figure 3.1, those reaches of the Rhine near Sankt Sebastian are considerably steep. As opposed to other reaches however, water level profiles do not exist here for which reason we can only apply an averaged value provided by the SWORD database. Moreover, the two Dutch river cases experience large tidal fluctuations which seem

to be differently captured by the downsampled altimetric and in-situ measurements, subsequently causing a periodic bias. Among the cases with the lowest median and standard deviation of a-posteriori corrections are Mannheim, Oestrich-Winkel and the two Spay cases. These virtual stations present rather favorable scenarios and hence deliver better results.

To conclude, one of the main takeaways from the scatter plots representing the river stations is the fact that waveforms echoed to the altimeter from situations near the river bank are noisier, less favorable in terms of peakiness and kurtosis, and subsequently go hand in hand with higher a-posteriori corrections to the retracking gates. As elaborated, the situation for sampled points over the middle part of the river is vice versa. In the following, we demonstrate the same scatter plots for the entirety of lake stations and the corresponding density plots.

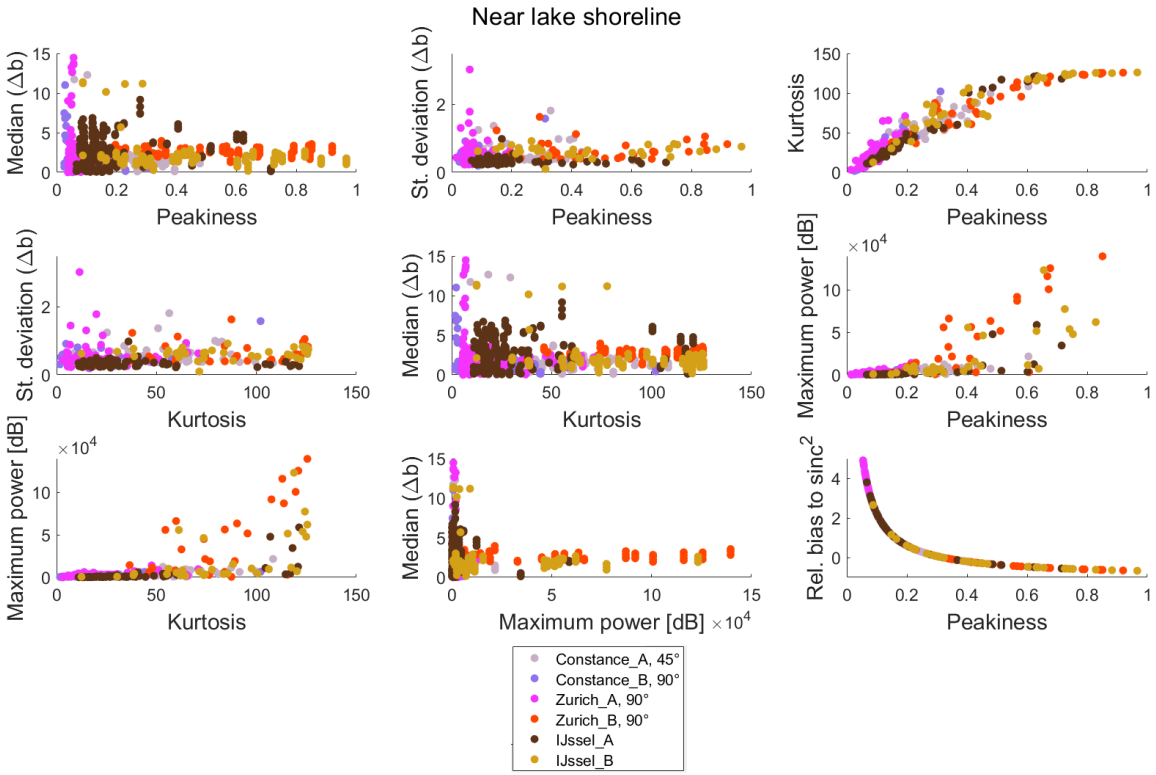

Figure 3.17: *Addressed statistics for all cases near the lake's shoreline*

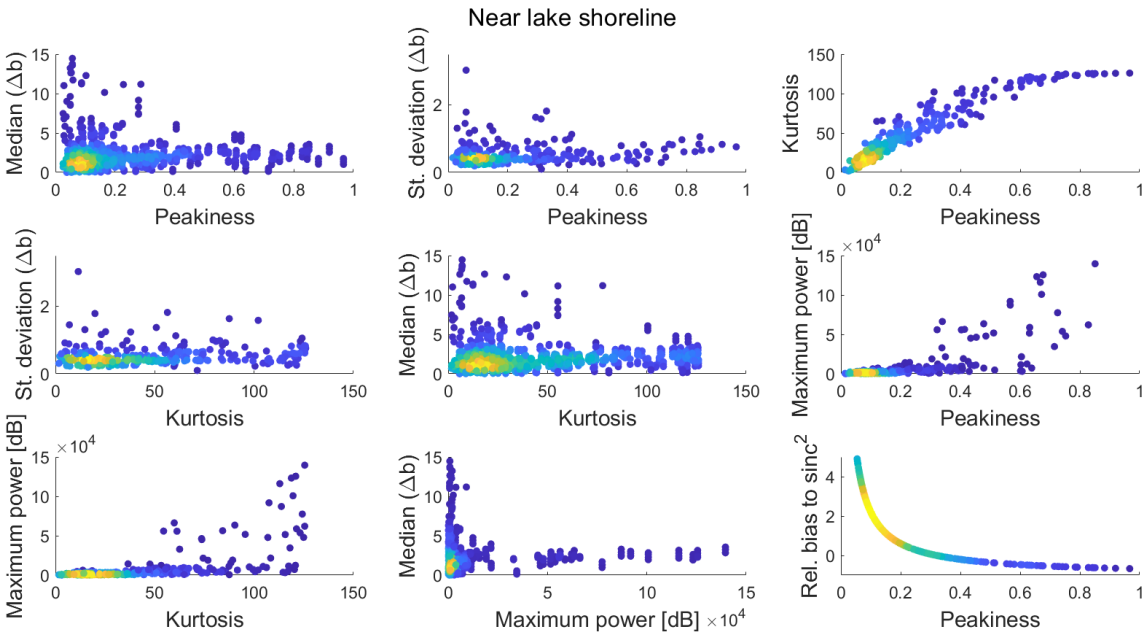

Figure 3.18: *Density plot for all cases near the lake's shoreline*

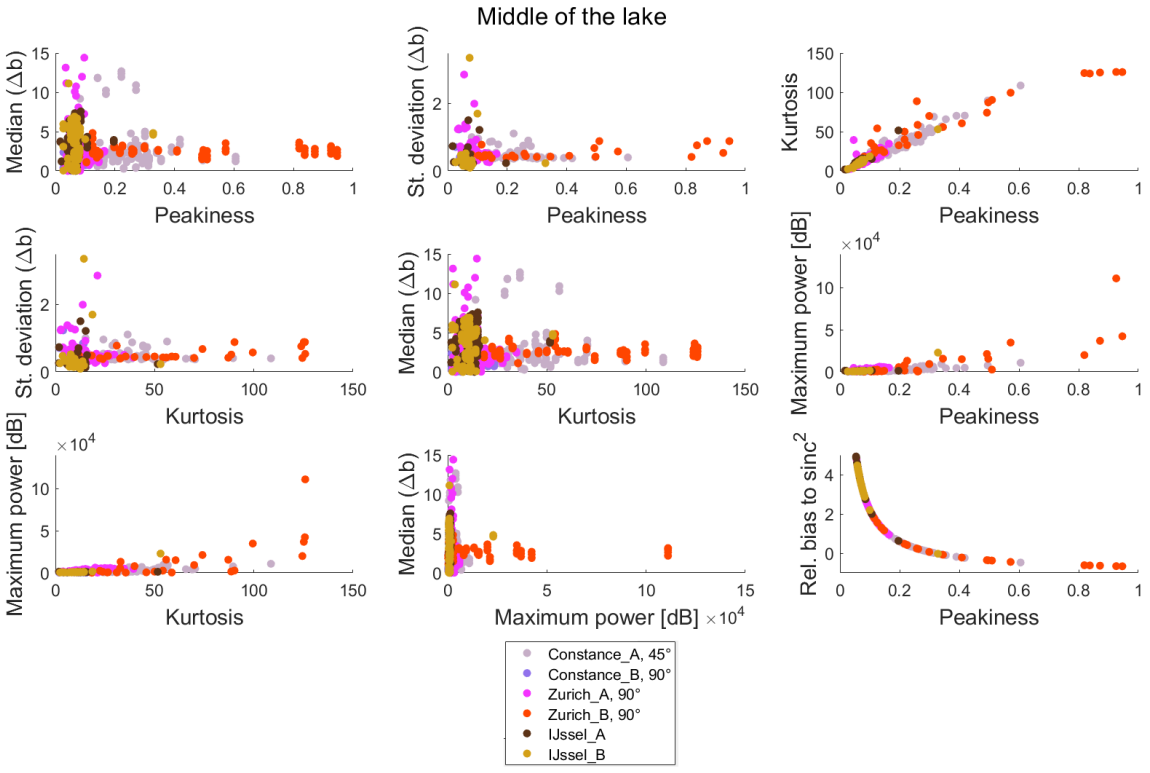

Figure 3.19: *Addressed statistics for all cases in the middle of the lake*

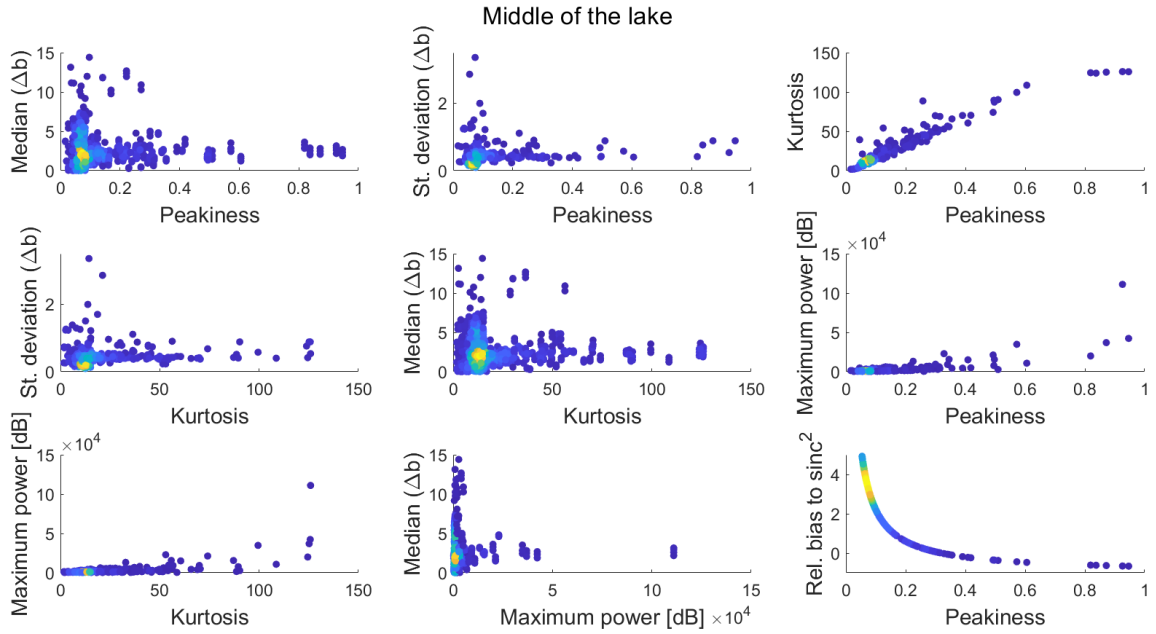

Figure 3.20: *Density plot for all cases in the middle of the lake*

Figures 3.17 to 3.20 refer to all lake cases and deliver some additional information to that revealed by the river cases. First, we briefly go into detail about the individual cases. Based on the distribution of median (Δb), it appears that Lake IJssel (S3A), and to some extent Lake Zurich (S3A), receive higher a-posteriori corrections. In fact, in both cases the data points hardly reach out into peakiness ranges of higher values (figure 3.17). Interestingly, over the middle part of Lake IJssel, the data points derived from both satellites do not spread out to ranges of higher peakiness, as opposed to near the shoreline. In general, higher a-posteriori corrections in the Lake IJssel case can be attributed to the fact that it is a human-controlled lake which regularly fluctuates. Here the same issue arises, that the downsampled in-situ and altimetric measurements capture the regulated water levels differently and causes a bias. Lake Constance shows the most favorable results in both sampling scenarios. Some behaviors of the scattered data resemble the figures of river cases, such as higher median/standard deviation (Δb) in lower ranges of peakiness, yet decrease in higher ranges of peakiness. Also, the standard deviation (Δb) shows the same aforementioned constant alignment of data along the x-axis of the respective subplots.

In the density plots (figures 3.18 and 3.20) it is interesting to see that the scattered data does not look necessarily more favorable for the middle of the lake. The findings in the river scenarios, such as a left-shifted accumulation on the x-axis and higher range of accumulation on the y-axis near the shoreline do not significantly occur with respect to the density plots over middle parts of the lake. The conclusion is rather the contrary. This can especially be seen in the plots involving peakiness where many scattered points reach high values near the lakes shoreline while those over the middle of the lake remain relatively low. Only few data points in the scatter plots over the middle of the lake reach higher peakiness and also kurtosis values. Boy et al. (2021) elaborate with the help of the same two crossing scenarios of both Sentinel-3 satellites over Lake Constance as in this study, that waveforms' shape and particularly their peakiness are mainlky impacted by the water body's illuminated surface and its roughness

within. Waveforms as a result of echos from larger, uninterrupted surfaces tend to resemble those over oceans and hence are less peaky. Vice versa, echos from smaller sections of lakes, and thus closer to the shoreline, generate waveforms of higher peakiness. As a matter of fact, this is what becomes clear when comparing the peakiness-related scatter plots between near-shoreline and lake-middle observations.

In the beginning of this chapter we evaluated the performances of the retrackers dedicated to the Sentinel-3 mission and the geophysical corrections which in combination is what we refer to as permutations. Each was assessed based on the five metrics: CC, RMSE, RBias, KGE and NSE. Over the entirety of river and lake stations, the OCOG-retracker proved to be the best-performing one, which occurred the highest number of times among the given metrics and for all cases. Moreover, it was interesting to see that the arrangement of geophysical corrections based on experts' judgment rater deviated from the results following our assessment. Hereby, it was not the suggested ECMWF model at measurement altitude for the wet and dry tropospheric components, but corrections determined by the onboard radiometer and from the ECMWF model at zero altitude, respectively. For the ionospheric components, the suggested GIM corrections share the stage with those determined by the altimeter (one of which in pseudo low resolution mode). Later on, we conducted an analysis involving specific SAR-waveform properties and a-posteriori corrections, which refer to the waveform-level projection of the offset between altimetric and in-situ water level timeseries at every epoch. Among many findings, there were two main takeaways from the analysis. For one, waveforms with high values in peakiness, kurtosis and maximum power essentially required smaller a-posteriori corrections to the initial retracking gates. Conversely, waveforms with low values in the mentioned parameters due to multi-peaks and noise received significantly larger a-posteriori corrections. For another, it was shown that for river cases, the a-posteriori corrections to the initial retracking gates in waveforms resulting from measurements over the middle are in their entirety smaller than those from over the side of the river. For lakes, the situation tends to be the opposite in which waveforms generated from echos over the middle of the lake resemble those of ocean surfaces and hence are considerably noisier. Consequently, the a-posteriori corrections are in their entirety larger than those coming from near-shoreline measurements.

Among all the components that make up a permutation, retrackers have the most significant impact on the final water level. Determining the correct retracking gate in the waveform is therefore central to water level retrieval and can cause variations of up to several meters with respect to the timeseries of other retrackers. Although it was revealed in our assessment that the OCOG-retracker performed the best for the entirety of river and lake cases, it still produced vast outliers in specific epochs when compared to the true water level and to that determined by the other retrackers (figures 3.3 and 3.4). As a matter of fact, Jiang et al. (2020) conclude from their study that the OCOG-retracker is unable to handle multi-peak waveforms. This comes to show that retrackers all have a considerable uncertainty level of their own and encounter challenges for different types of waveforms. As listed in chapter 1, the retrackers dedicated to the Sentinel-3 mission mainly use empirical or analytical modeling algorithms as well as the waveform's physical properties to determine the mid-point of the leading edge and thus the correct water level. In the following chapter we introduce a retracker in three realizations based on a stochastic approach.

Chapter 4

Stochastic retracker

In the previous chapter, we make use of a-posteriori information in the form of corrections to the retracking gate on a waveform level. Herein, we made two decisive assumptions:

1. The corrections obtained from in-situ data are legitimate
2. The corrections can be projected onto the range, assuming that the geophysical corrections are error-free

Following the reverse retracking approach one open question arises however. Despite the local gauge data being assumed as correct, do the a-posteriori corrections to the respective retracking gates really yield an appropriate new gate for the retrieval of water levels? For instance, based on our knowledge in satellite altimetry, a-posteriori corrections to a retracking gate that land on a bin of the trailing edge or thermal noise portion of the waveform would not be considered as plausible. This idea drives us to describe any part of a given waveform in terms of its probability to be most ideal for water level retrieval. Later, we take this a step further and design our own stochastic-based retrackers.

Our aim is to assign a probabilistic estimate to every bin of the waveform. In other words, these probabilities indicate how likely it is that the corrected range gate marks the correct range between the satellite's altimeter and the Earth's surface from which we derive the water level. Following a similar approach presented in Gao et al. (2019), we at first narrow down the entire waveform to a smaller, yet more useful portion of the signal. By doing so, we assume water level derivations from the thermal noise and trailing edge sections of the waveform to be unreasonable and hence we omit them from further considerations. To gain an estimate over the approximate center-bin of the narrowed down portion, we use a DEM and the altitude of the satellite. This estimate corresponds to the range from the satellite to its instantaneous location on the Earth's surface. We approximate the current elevation by interpolation and subtract it from the satellite's altitude. Beforehand, it must be assured that the subtraction takes place in a mutual reference frame (namely the ellipsoid), in which case the exact geoid heights are added to the interpolated elevation. In the next step, the rough range estimate is converted into bins and can now be visualized on a waveform level. To set up the aforementioned portion of the waveform, we define a bufferzone around the previously estimated range gate. During its development, the NASADEM was meant to meet requirements for a vertical error of up to 16 m (Buckley et al., 2020). We see this quantity as an appropriate benchmark value to establish the bufferzone. 16 m corresponds to 34.1570 bins which will be the width of the buffer zone centered at the DEM-based range gate.

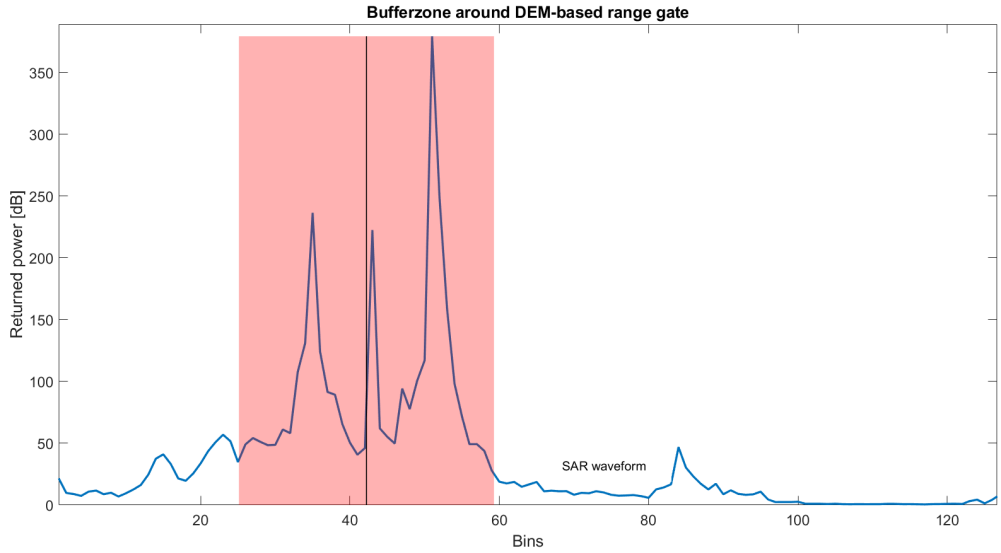

Figure 4.1: *Bufferzone (red patch) around the DEM-based range gate*

Figure 4.1 visualizes the bufferzone with its center-bin corresponding to the DEM-based range gate. Now that the bufferzone is defined, we aspire to assign a probability to each waveform-bin located within it.

4.1 Empirical waveform-based distribution

In this approach we define our own probability distribution which focuses more on the properties of the waveform itself, rather than fitting a known probabilistic distribution. More precisely, it is important to emphasize those parts of the waveform that are central to water level retrieval such as the steepest part of the leading edge and the peak. To this end, we consider the individual waveform itself as well as its first derivative. The first derivative is useful in the sense that its peaks represent the steepest part of the waveform's leading edges. We present three different strategies to assign the probabilities using both the waveform itself and its first derivative:

1. Addtion of of both signals (rtADD)
2. Multiplication of both signals (rtMULT)
3. Maximum of both signals (rtMAX)

Note that all of the methods above are performed on an elementwise basis between the waveform and its first derivative. While using the first derivative of the waveform, we take the absolute values instead of the original signal as below-zero values would not significantly contribute to this approach.

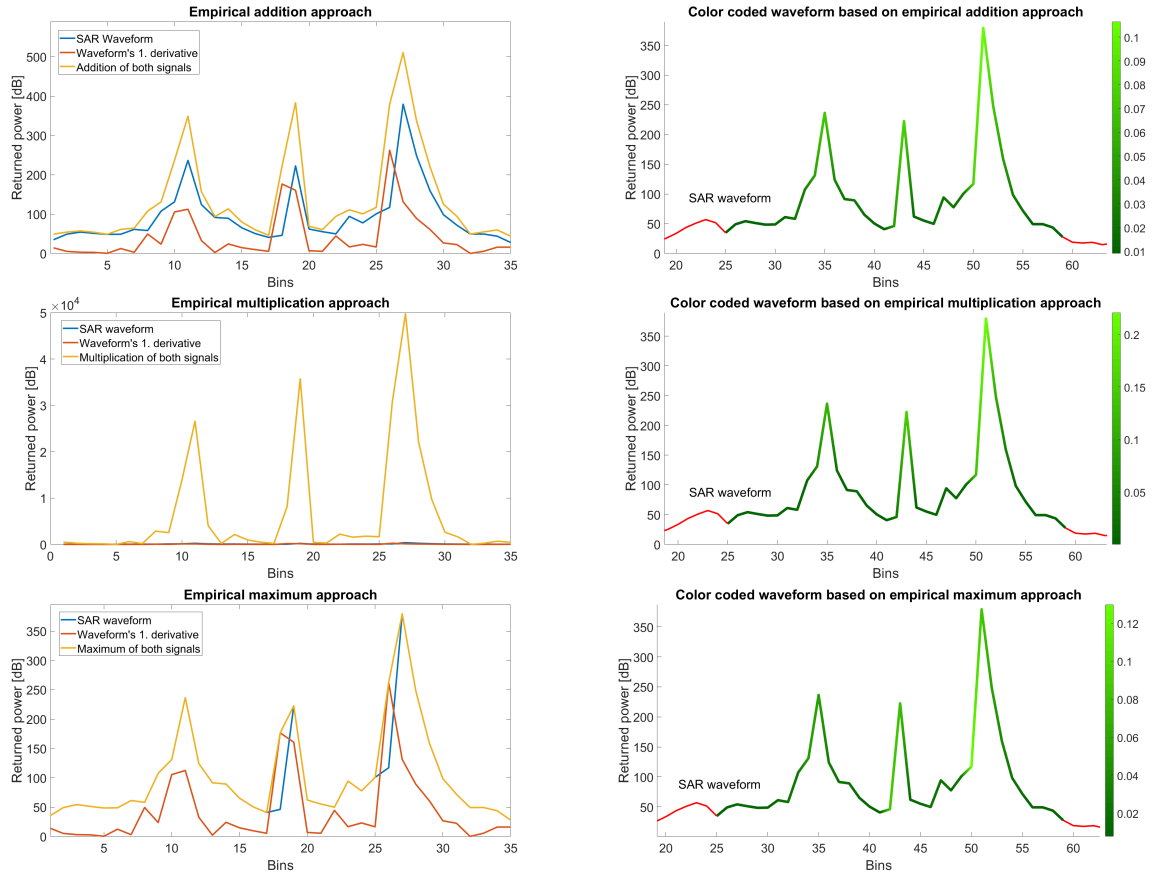

Figure 4.2: *Empirical addition approach and resulting color coded waveform*

The left half of figure 4.2 demonstrates for all three strategies the original waveform (blue) within the bufferzone, together with its first derivative (red) and the resulting signal (yellow). The latter is the basis for the probability distribution which in the right half of figure 4.2. Herein, the red portions of the signal are those excluded by the bufferzone and the variation of green tones indicate the assigned probabilities with dark green corresponding to lower and light green to higher values. Note that the resulting yellow signal on the left hand side is normalized to represent proper probabilities. From the color-coding in the addition-based approach it becomes apparent that, in particular, leading edges and the peaks receive higher probabilities compared to the troughs and trailing edges of the waveform. Due to the fact that both signals were simply added, smaller peaks are not neglected, but rather amplified and therefore given more of a chance to signify the correct range. In the empirical multiplication approach, the original waveform and its first derivative are multiplied. Hence, the resulting signal is strongly amplified, so much so that all three signals can not be visualized in one single figure. In particular, those parts of the waveform which were initially higher in power are now clearly exaggerated. Consequently, in the color-coded waveform, peaks receive the highest probabilities relative to their surroundings. Leading edges also receive significantly high probabilities, but remain somewhat smaller. In the final approach, we use the maximum of both signals. On an elementwise basis, the greater value of the waveform and its first derivative are taken to define the corresponding point of the resulting signal. The reason for this approach is the fact that peaks in the first derivative occur approximately one bin prior to the original waveform's peak and therefore, give the leading edge significant importance. It also enlarges the width

of the resulting signal's peak on the left hand side. This is particularly noticeable in the color coded waveform. At the beginning of the leading edges, the probabilities are the highest and even decrease a little towards the peaks. Furthermore, the trailing edges show considerably low probabilities.

4.2 Relationship between probabilities of retracking gates and RMSE

Prior to proceeding with our stochastic retrackers and the generation of water levels, we briefly analyze the relationship between the previously distributed probabilities and the corresponding permutation's RMSE with respect to the in-situ data. These probabilities are obtained from the new retracking gates after having been a-posteriori corrected (as demonstrated in chapter 3). This should, for one, give a first indication of the probability distribution's quality and, for another, serve as a motivation to the concept of stochastic-based retrackers. Assuming our proposed probability distributions to all bins of the waveform are reasonable, we expect the RMSE to decrease as the probability rises. This is due to the fact that the a-posteriori corrected retracking gate should land on a bin that, at best, retrieves the correct water level. Conversely, small deviations from the most ideal bin for water level retrieval caused by individual corrections for permutations, would show slightly higher RMSE.

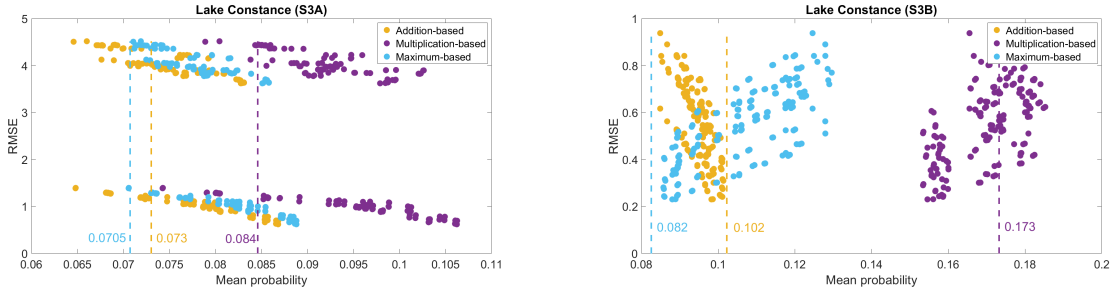

Figure 4.3: *Two exemplary scatter plots between the mean probability of each permutation against their RMSE with respect to the in-situ data*

Figure 4.3 demonstrates scatter plots between the aforementioned parameters for a Sentinel-3A and Sentinel-3B virtual station over Lake Constance. Herein, each scattered data point corresponds to one permutation of the 240 for which we determine the mean probability over all measurement epochs. The colors represent the three strategies for assigning the probabilities. In addition, we also mark the mean probability of the initial Ocean-retracking gate (before a-posteriori correction) by the dashed vertical lines. The example on the left presents a very favorable scenario with a downward behavior as we expected and even a clear delineation of the three probability distribution approaches. Evidently, there is a huge vertical gap between the data points. This can be traced back to the individual retrackers as they determine different retracking gates among each other. In this case, the Ocean- and OCOG-retracker account for the scattered data points in the lower half of the left figure whereas the IceSheet- and SeaIce-retrackers make up the ones in the upper half. The remaining Ice-retracker fails to deliver retracking gates at this virtual station and is thus not represented at all in figure 4.3. Moreover, the distribution of scattered data makes a first indication of the quality of the three probability assignment approaches. To start, the addition- and maximum-based approaches show

a very similar behavior in which the latter tends to achieve slightly higher probabilities. The multiplication-based distribution is horizontally offset to the other two and thus reaches higher probabilities for nearly equal RMSE. As a matter of fact, this is an intuitive finding since the peaks in the waveform receive very high probabilities due to the multiplication of the wavefrom and its first derivative. In the other two approaches the probabilities are distributed more evenly across the waveform. It is noticeable however, that the horizontal range of mean probabilities in the multiplication-based approach is significantly larger than that of the others which is also related to its probability distribution. Namely, when retracking gates are just slightly offset to the main peak of the waveform, the obtained probabilities quickly drop as only the peak is considerably amplified.

In the right half of figure 4.3 the distribution of scattered data is significantly different. At first sight, the most noticeable difference is the behavior of multiplication- and maximum-based data points. Hereby, they rather increase in RMSE with growing mean probabilities which completely opposes our expectations. There is an evident horizontal offset between the two, which in this case does not refer to the determined retracking gates anymore, but is related to the quality of the probability distribution approach. Between the two, the multiplication-based achieves higher mean probabilities and therefore might yield better results later on. The addition-based approach however, reveals a similar behavior to the left hand figure in which it meets our expectations (scale differences to be noted). It is to some extent difficult to conclude beforehand whether the quality of the three approaches is highlighted by higher probabilities themselves. As demonstrated in figure 4.3 (right), increasing probabilities do not necessarily go hand in hand with decreasing RMSE. Therefore, it is not the achievement of higher probabilities, but rather its link to decreasing RMSE that yields an appropriate distribution which was shown by the addition-based approach in both subplots. Consequently, we presume the addition-based approach to present the most suitable basis for stochastic retracking.

On another note, we shall not neglect the possibility to determine the probability of the initial retracking gates before undergoing the a-posteriori correction. As addressed earlier, the dashed vertical lines in figure 4.3 mark the mean probabilities of the Ocean-retracking gates over all measurement epochs for the three distribution approaches. Under the assumption of our proposed probability assignment across the waveform being appropriate, this approach can be seen as an additional method of validation. In particular where in-situ measurements are unavailable this approach provides an option to assess the results from altimetry-derived water levels based on the probabilities their individual retracking gates obtain in the waveform. The two exemplary subplots reveal that, for the most part, the mean probabilities of the initial retracking gates lie either centered or left-oriented with respect to the cluster of data points from the same distribution approach. The only exception to this statement is the mean probability of the Ocean-retracking gate in the addition-based approach on the right side of figure 4.3. Hereby, it lies slightly ahead of the corresponding cluster. The other cases show good examples however, of the reverse retracking we performed in chapter 3. Namely, large portions of the scattered data points in figure 4.3 lie ahead of the corresponding dashed lines and thus reveal higher achieved probabilities. We expect such a finding since a-posteriori correcting the initial retracking gates should yield higher probabilities in the waveform due to their agreement with the true water level.

In conclusion, the demonstrated relationship between the probabilities and the RMSE with respect to the true water level, as well as the relatively low probabilities of the initial retracking gates, drives us to design stochastic retrackers based entirely on the probability assignment within the wavefrom. In particular the addition-based approach proves that retracking gates of higher probabilities yield smaller RMSE over the entirety of the timeseries. In the upcoming sections it will be revealed which of the aforementioned approaches present themselves as the most suitable for the retrieval of correct water levels.

4.3 Retracker

Following the brief analysis and the assignment of probabilities to each bin of the waveform, the stochastic retrackers determine the retracking gate based on equation 4.1:

$$\text{bin}_{\text{retracker}} = \text{argmax}(P) \tag{4.1}$$

In the equation above, the new retracking gate corresponds to the bin of the highest probability (P) in the waveform. Now that a new retracking gate has been determined, we correct the derived range with the best expert-judged set of geophysical corrections to obtain the final water level from our three approaches.

4.4 Visual presentation and analysis of new retrackers' performances

In this section, we visualize the water level timeseries obtained from the three new retracking methods alongside those from the initial five retrackers, as well as the local gauge data. For each of the timeseries derived from the initial retrackers, the best expert-judged set of geophysical corrections listed in chapter 3 is applied. In this way, we can compare the timeseries from the new retrackers to these on a visual and numerical basis, in particular with respect to the referential in-situ data by calculating some of the metrics presented in chapter 3. We divide this section into two parts, corresponding to river and lake cases as preliminary analyses indicated that the two present different behaviors and characteristics.

4.4.1 River cases

Figures 4.4 to 4.12 show the water level timeseries for the initial retrackers dedicated to the Sentinel-3 mission, the new retrackers presented in this study's methodology and the nearest in-situ data. From a first visual inspection, the timeseries generated from the new retrackers, for the most part, are fit quite well to the timeseries of the initial retrackers and to that of the in-situ data. This is particularly the case at virtual stations Oestrich-Winkel (S3A), Spay (S3B1), Spay (S3B2), Mannheim (S3A) and Vuren (S3A) (figures 4.4, 4.5, 4.6, 4.7 and 4.9). Small deviations among each other and especially with respect to the in-situ data do occur yet remain fairly low for the aforementioned cases.

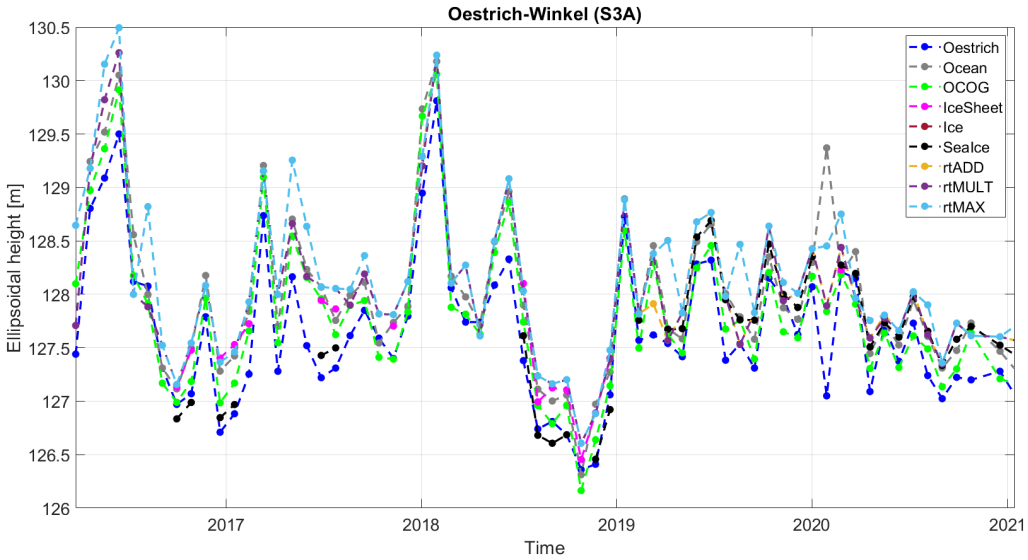

Figure 4.4: *Oestrich-Winkel (S3A): Water level timeseries from the new retracking methods, the old retracking methods and in-situ data*

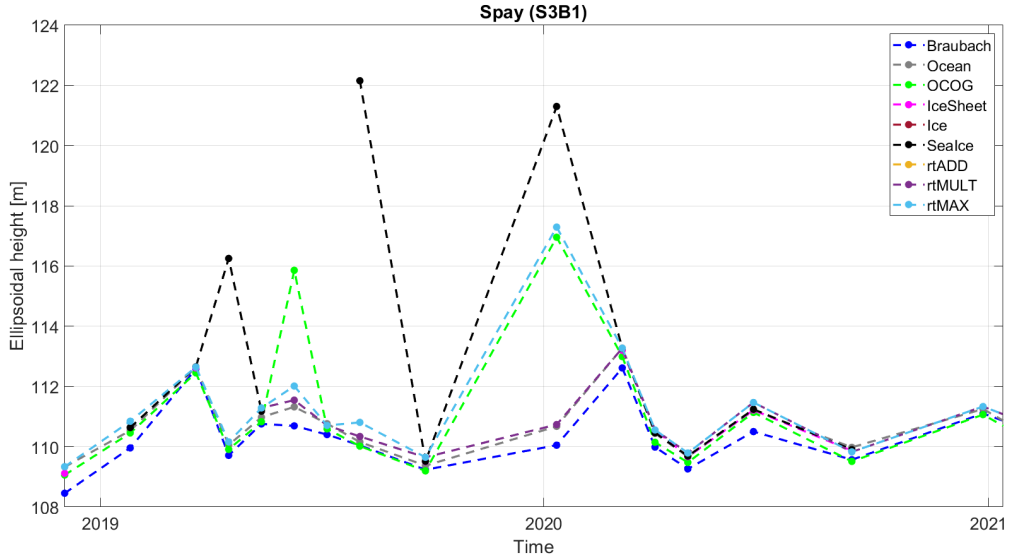

Figure 4.5: *Spay (S3B): Water level timeseries from the new retracking methods, the old retracking methods and in-situ data*

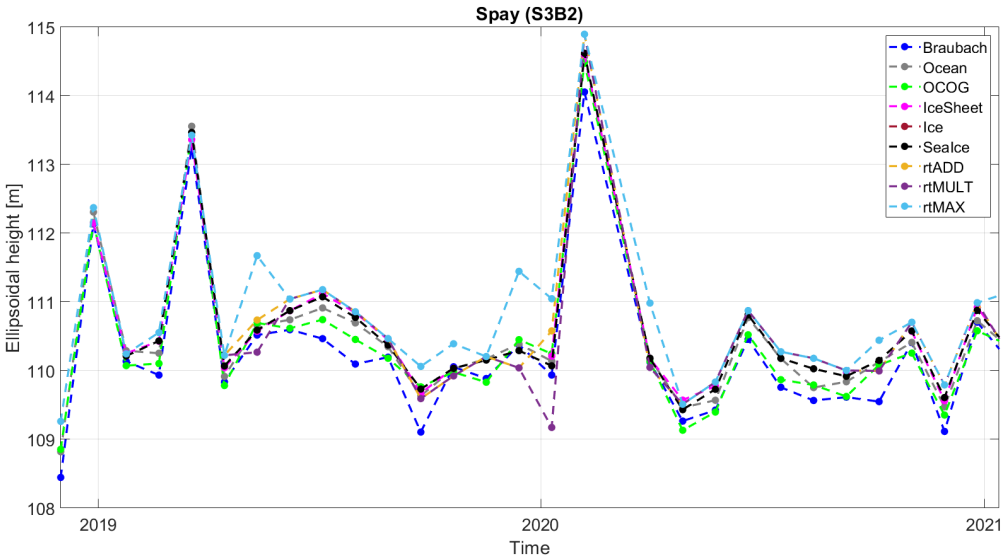

Figure 4.6: *Spay (S3B): Water level timeseries from the new retracking methods, the old retracking methods and in-situ data*

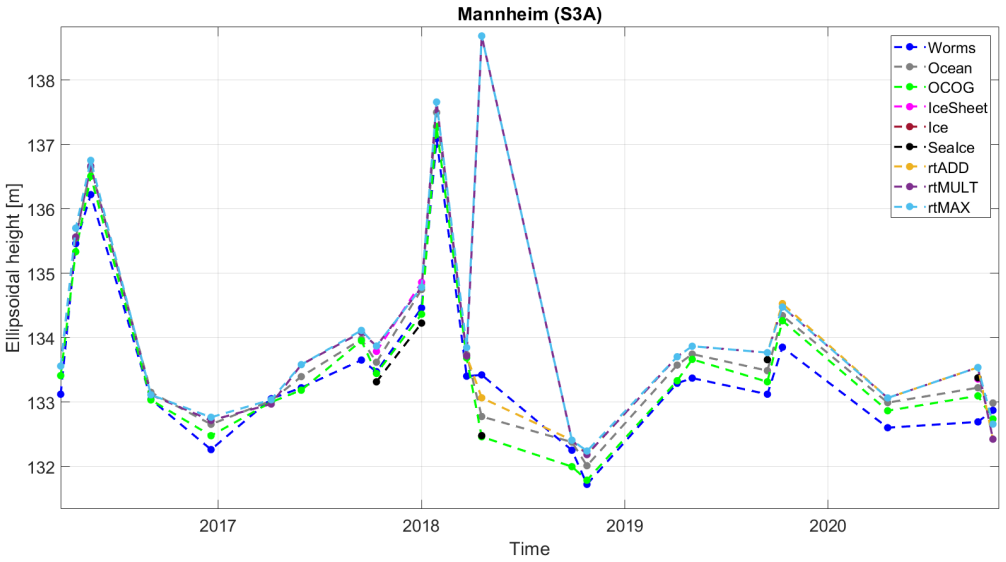

Figure 4.7: *Mannheim (S3A): Water level timeseries from the new retracking methods, the old retracking methods and in-situ data*

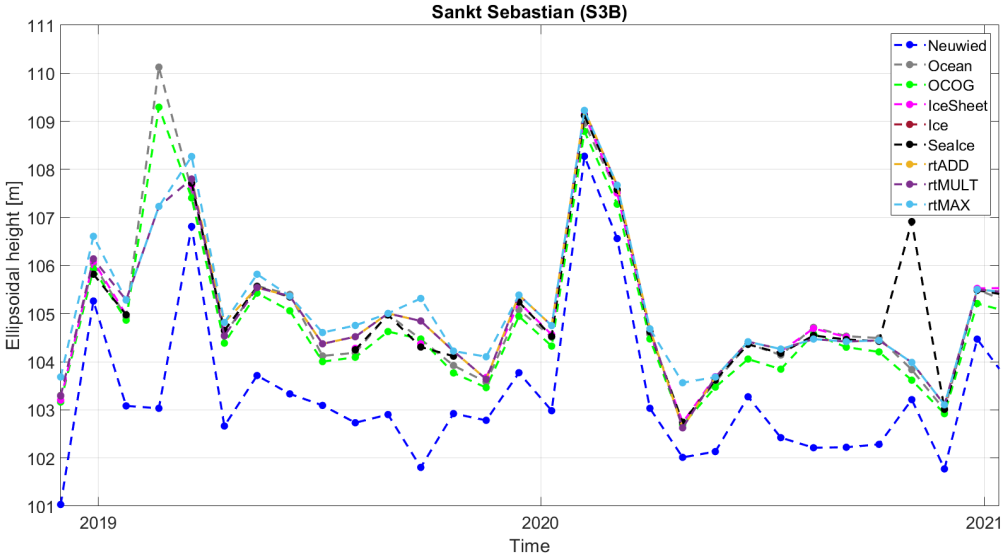

Figure 4.8: *Sankt Sebastian (S3B): Water level timeseries from the new retracking methods, the old retracking methods and in-situ data*

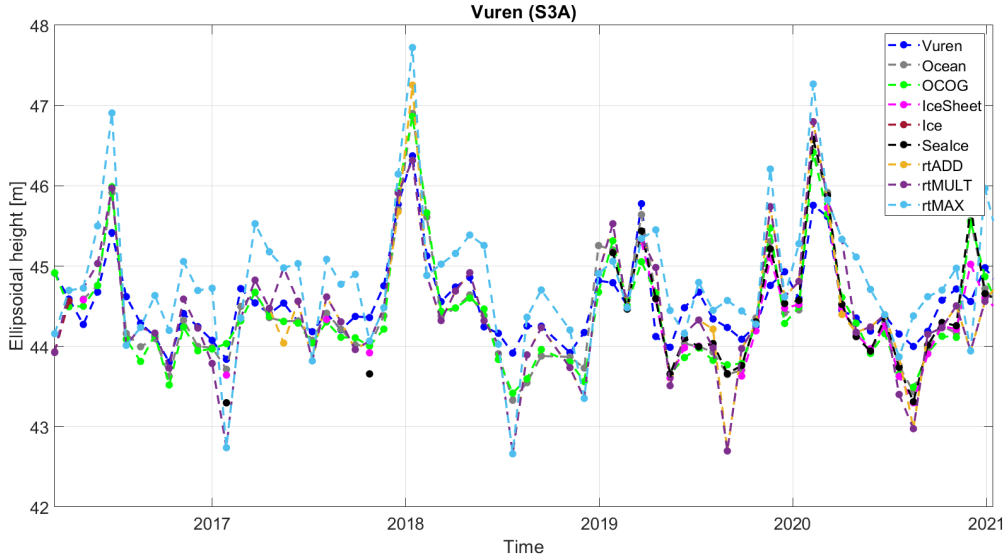

Figure 4.9: *Vuren (S3A): Water level timeseries from the new retracking methods, the old retracking methods and in-situ data*

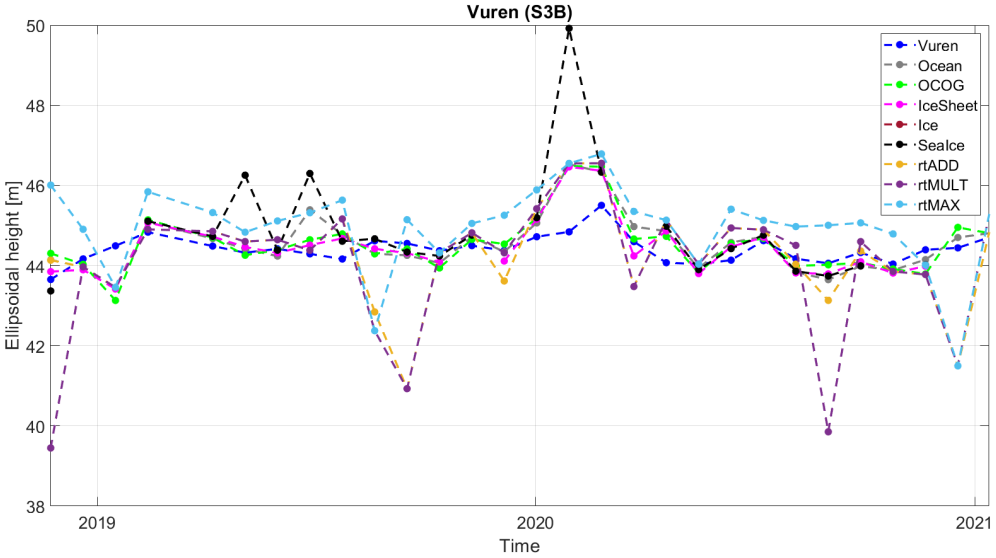

Figure 4.10: *Vuren (S3B): Water level timeseries from the new retracking methods, the old retracking methods and in-situ data*

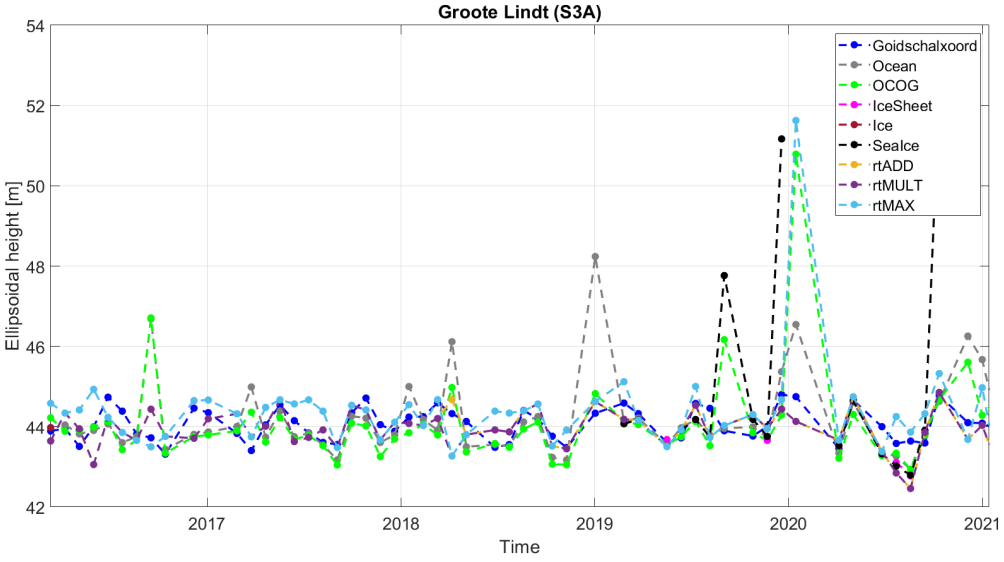

Figure 4.11: *Groote Lindt (S3A): Water level timeseries from the new retracking methods, the old retracking methods and in-situ data*

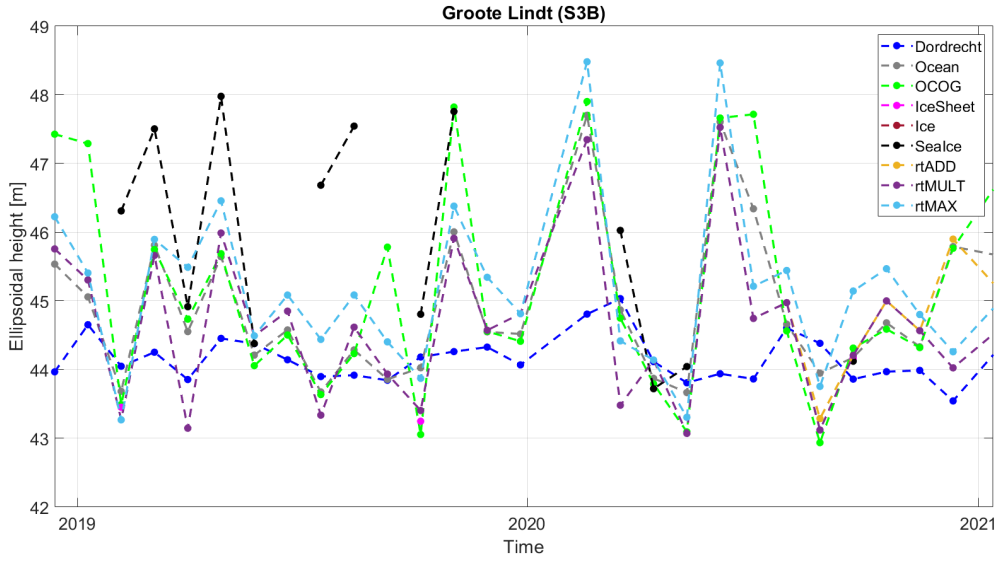

Figure 4.12: *Groote Lindt (S3B): Water level timeseries from the new retracking methods, the old retracking methods and in-situ data*

From the same first inspection a few considerable flaws become apparent as well. For one, some of the aforementioned timeseries which in the entirety show a well-fit behavior, also reveal crucial outliers. In figure 4.4 near the 2020 mark, all three of the new retrackers, and in particular the maximum-based retracker, show a large offset to the valley of the corresponding in-situ data. In fact, the water level according to the maximum-based retracker rose with respect to the preceding epoch rather than resulting in a valley. It is safe to say that in this epoch, the water levels were not only retrieved with a considerable offset, but also clearly demonstrate false dynamics of the river. Interestingly though, the Ocean-retracker captures this trend falsely as well and the remaining initial retrackers beside OCOG seem to fail in providing a water level in this epoch. In the other exemplary virtual stations, Spay (S3B1), Spay (S3B2), Mannheim (S3A), Vuren (S3A) and Vuren (S3B) (figures 4.5, 4.6, 4.7, 4.9 and 4.10), it is again the maximum-based retracker that shows either the largest considerable peaks offset to the in-situ timeseries or the most persistent offsets throughout the timeseries.

Furthermore, we must discuss the huge outliers that occur in some of the figures, such as in the peak of figure 4.5 near the 2020 mark and the maximum in figure 4.7 between 2018 and 2019. For the Spay case (S3B1), the huge outlier among two others from the initial retrackers, comes from the maximum-based retracking method. It yields an offset to the in-situ data of approximately seven meters, which can be attributed to a range/retracking error with high confidence. In the Mannheim (S3A) timeseries, the maximum-based retracker accounts for the large outlier, but also coincides with the outlier from the multiplication-based (dashed burgundy lines) retracker. To investigate the origin of this huge error, we have a closer look at the waveform of this very epoch and show the retracking gates of interest.

Both sides of figure 4.13 clearly delineate the origin of the large outliers in the Mannheim (S3A) and Spay (S3B1) timeseries. Subfigure 4.13(a) reveals the maximum-based retracking gate to lie on a minor peak towards the beginning of the waveform whereas the addition-based and Ocean-retracking gates are situated near the highest and thus main peak of the waveform.

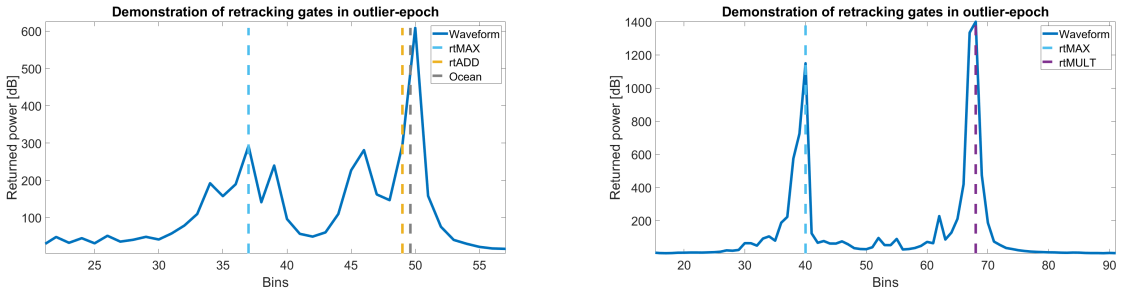

(a) Mannheim (S3A) (b) Spay (S3B1)

Figure 4.13: *Investigation of two timeseries outliers on a waveform level*

This visualization explains the offset occurring in the timeseries. More precisely, the timeseries shows that the addition-based retracker comes closer to the in-situ data than the Ocean-retracker does for the given epoch, even if not by much. Also this can be seen on a waveform level where the addition-based retracker determines a gate closer to the bin of half-height and steepest part of the leading edge, respectively. Likewise, subfigure 4.13(b) depicts a similar scenario in the sense that the maximum-based retracker finds another peak prior to highest and main peak of the waveform. This time, the smaller peak has a very significant height and prominent shape, unlike in subfigure 4.13(a). In theory, the maximum-based retracker performs as it should by finding this peak. In the beginning of this chapter we particularly explain that every peak should be given a chance to be appropriate for water level retrieval. However, with the help of in-situ data we can assure that retracking gates closer to the latter and thus main peak yield better results. To summarize this finding, the results in the water level timeseries and waveform representations of specific epochs demonstrate the maximum-based retracker's susceptibility to smaller yet considerable peaks and even noise. This occurs more than in the addition- and multiplication-based retracking methods since these strongly amplify the leading edge and maximum of the waveform's main peak, giving lower peaks less of a chance.

The remaining virtual stations that have either only been mentioned briefly or were left out, such as Sankt Sebastian (S3B), Vuren (S3B) and Groote Lindt (S3A and S3B) (figures 4.8, 4.10, 4.11 and 4.12), reveal rather complicated results. To start, in the Sankt Sebastian case, there is a persistent offset between the local gauge and the all altimetry-derived timeseries. In specific epochs, for instance towards the end of 2020, these offsets amount to nearly three meters. Considering that this offset persists for the majority of the timeseries, one can conclude this error to be of systematic nature. One possible explanation is that the slope estimate applied to the altimetric timeseries is not precise enough to enable an appropriate comparison basis. Namely, at the Sankt Sebastian virtual station we do not have access to water level profiles reaching to the local gauge. Consequently, we simply use the averaged data for the entire reach provided by the SWOT river database. For other virtual stations where we apply the averaged slope value, such as Vuren and Groote Lindt, this would not be as crucial since those lower reaches of the river are rather flat. Near Sankt Sebastian however, slopes play a significant role due to the great topographic decline of the region (see chapter 3). Nonetheless, what we can take from this figure is that all retrackers, for the most part, perform similarly well with respect to each other. In fact, in specific epochs the new retrackers seems to perform slightly better than the initial ones (see peak shortly after 2019 mark in figure 4.8).

As mentioned above, the maximum-based retracker produces the most visible offset in the Vuren (S3A) timeseries. To be precise, visual inspection concludes that multiple peaks and troughs are further amplified in the maximum-based timeseries. To some extent, this finding also applies to the timeseries of the multiplication- and addition-based retrackers. To generalize, the greater in amplitude a peak or trough is in the local gauge data, the larger are the offsets to the altimetry-derived water levels. Similar findings can be made nearby under the Sentinel-3B crossing (see figure 4.10) with the difference that the multiplication-based retracker seemingly performs the worst among the new ones. This statement can be supported by the large reoccurring outliers in its timeseries.

The two virtual stations at Groote Lindt, are definitely interesting and likewise quite complicated. Under the Sentinel-3A crossing, the water levels from the new retrackers visibly resemble the local gauge data more than those from the initial retrackers. In particular, some peaks with considerable offsets to the gauge data can be seen in the Ocean, OCOG and SeaIce timeseries. Among the new retrackers there is only one such outlier of similar gravity, produced by the maximum-based retracker. Otherwise, the given timeseries follow similar trends. Under the Sentinel-3B crossing the situation appears to be more complex and does not leave a lot of room for analysis. To some extent, the initial retrackers fail to retrieve water levels in every epoch. The new retrackers do deliver water levels in every epoch, yet do not necessarily yield better results. In essence, all retrackers in this scenario produce water levels with high fluctuations and offsets with respect to the in-situ data. Perhaps, the conclusion from this figure is that altimetry-derived water levels and the in-situ measurements can not be brought to a comparable basis. This could be related to the fact that the Dordrecht gauge is too far from the at-nadir locations of the altimetric measurements and experiences different river dynamics. Namely, the section of the water body where the altimetric measurements take place is fed by the Dordtsche Kil from the South and the Oude Maas from the East. The Dordrecht gauge on the other hand, experiences contributions from the Noord River, the Beneden Merwede and the Wantij stream. According to the SWOT river database, there is no slope between the at-nadir locations of the altimetric measurements and the Dordrecht gauge. Nevertheless, there are some evident dynamics occurring in the region that complicate this case.

4.4.2 Lake cases

Figures 4.14 to 4.19 show the water level timeseries for the few lake cases of this study, including the same initial and new retrackers, as well as the corresponding local gauge measurements. From first visual inspection, all cases beside Lake Constance (S3A), show high variability and near-constant offsets to one another. To begin, the Lake Constance (S3A) case in figure 4.14 shows an overall appropriate timeseries for all retrackers under the neglect of three big outliers. Variability seemingly occurs with fairly low intensity. The new retrackers for the most part perform well with respect to the in-situ data, yet do reveal some deviations up to two meters in specific epochs. To some extent, this can also be detected among the initial retrackers, but in general they appear to follow the local gauge data slightly better than the water levels of the new retrackers. Following a similar in-depth analysis as in the previous subsection, it will be interesting to see the difference between the fairly small and the huge outliers on a waveform level. Previously, we showed that outliers of large magnitudes, such as the one near the 2019 mark in figure 4.14, originate from less peaky waveforms or even from multi-peaks. This

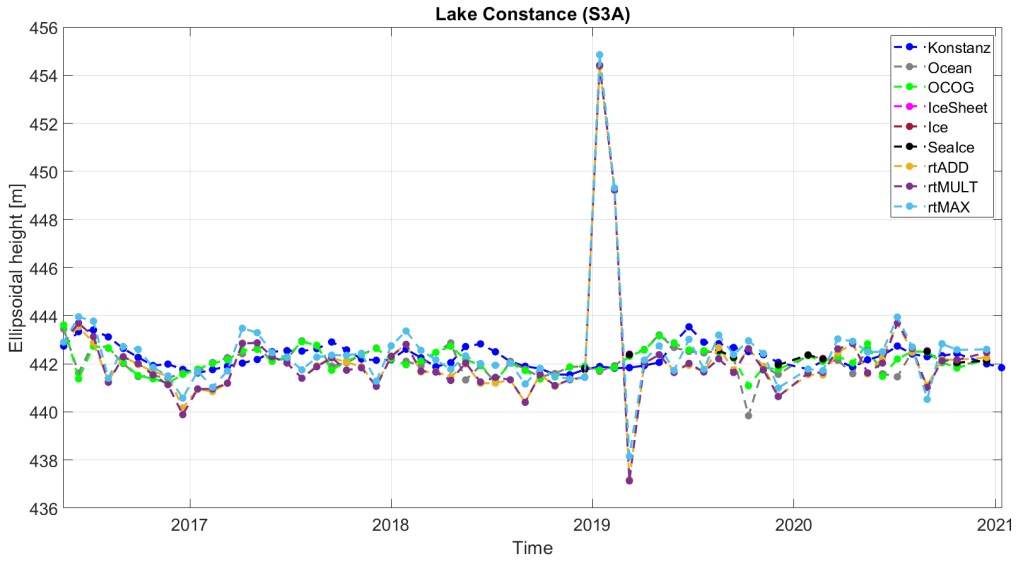

Figure 4.14: *Lake Constance (S3A): Water level timeseries from the new retracking methods, the old retracking methods and in-situ data*

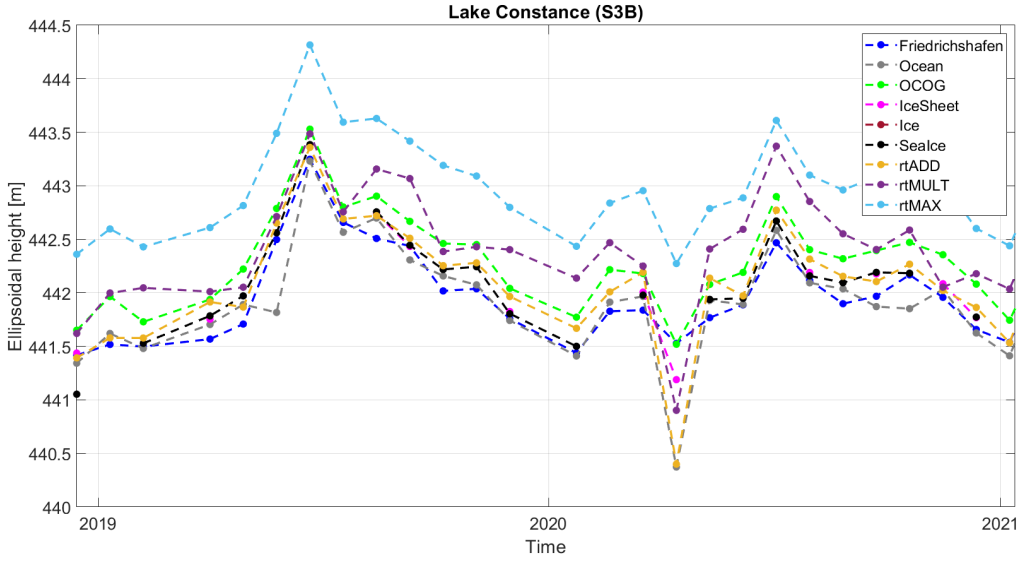

Figure 4.15: *Lake Constance (S3B): Water level timeseries from the new retracking methods, the old retracking methods and in-situ data*

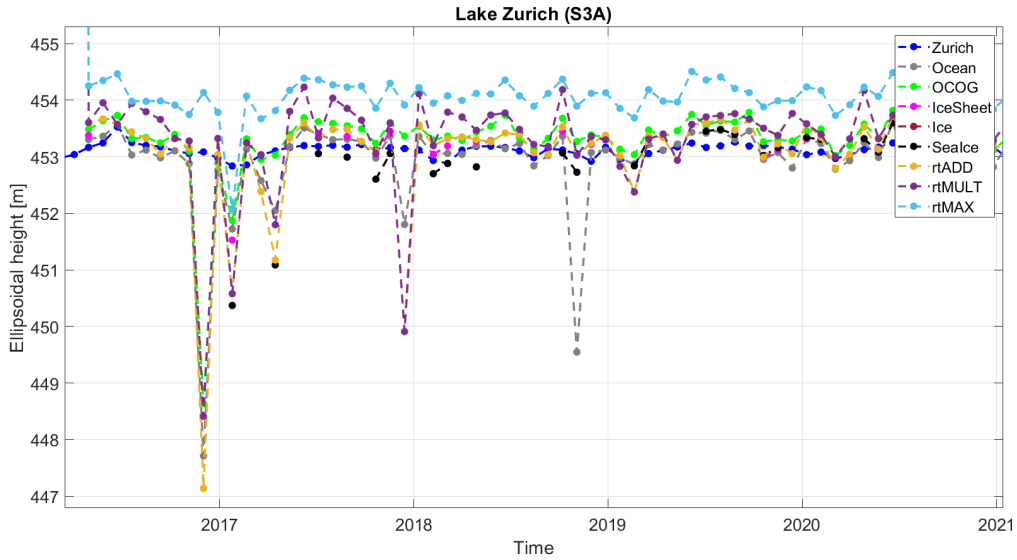

Figure 4.16: *Lake Zurich (S3A): Water level timeseries from the new retracking methods, the old retracking methods and in-situ data*

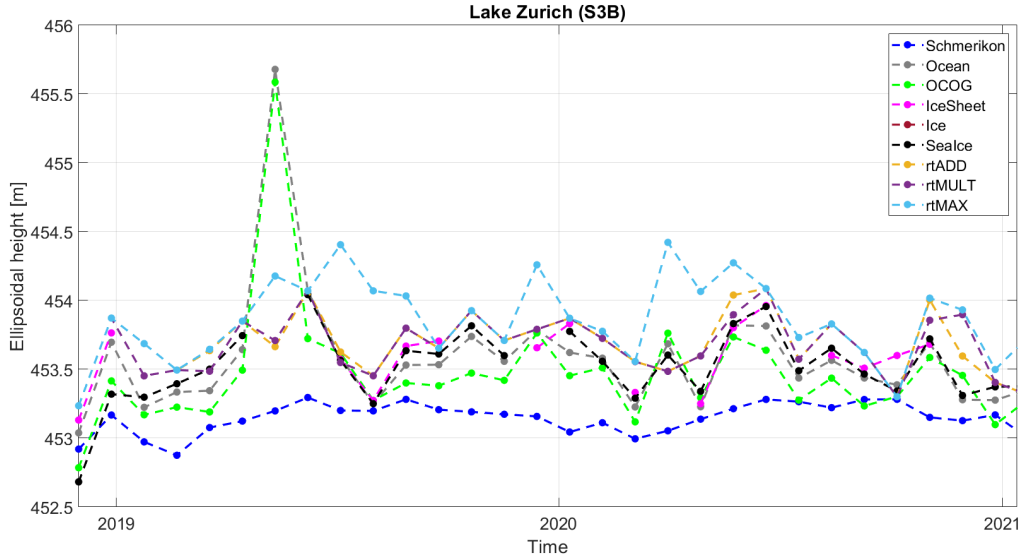

Figure 4.17: *Lake Zurich (S3B): Water level timeseries from the new retracking methods, the old retracking methods and in-situ data*

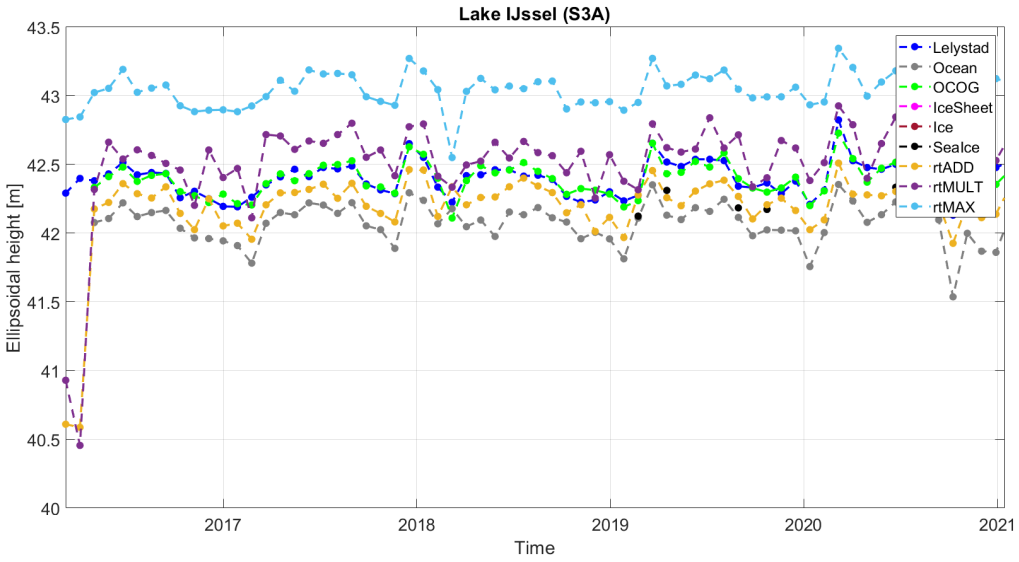

Figure 4.18: *Lake IJssel (S3A): Water level timeseries from the new retracking methods, the old retracking methods and in-situ data*

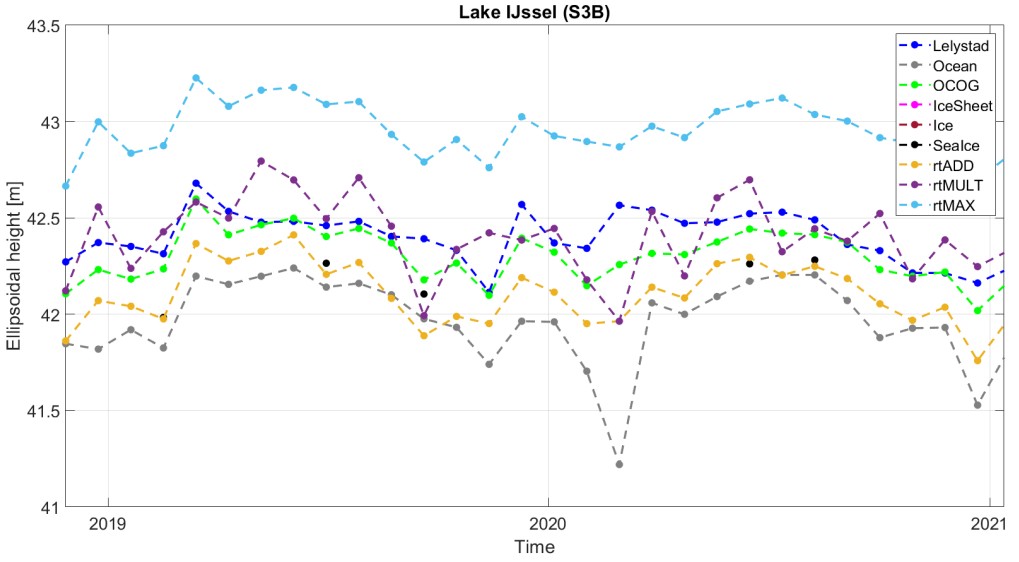

Figure 4.19: *Lake IJssel (S3B): Water level timeseries from the new retracking methods, the old retracking methods and in-situ data*

is also the case for the huge peak in the Lake Constance (S3A) case. Now, we visualize the waveform and some retracking gates in the small outlier-epoch near the 2017 mark.

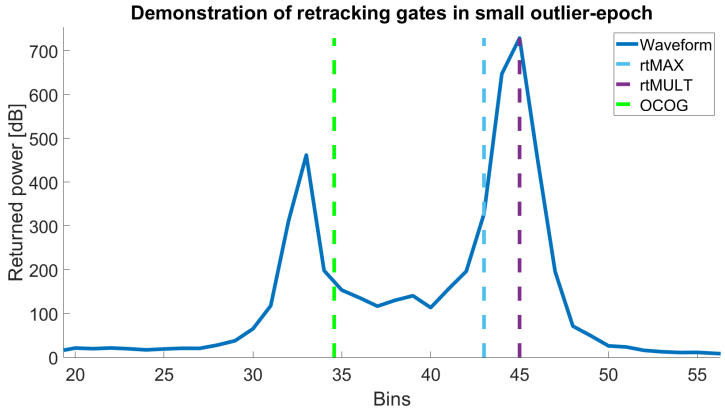

Figure 4.20: *Investigation of small outlier near 2017 mark*

Based on general knowledge in satellite altimetry, figure 4.20 does not necessarily deliver a clear explanation for the small outlier occurring near the 2017 mark. In fact, from this figure one would assume the maximum- and multiplication-based retrackers to produce water levels with less of an offset to the in-situ data as their gates are situated by the leading edge and maximum of the main peak, respectively. The addition-based retracking gate coincides with that of the multiplication-based retracker in this figure. The OCOG-retracking gate is, for one, shifted in bin-direction by around ten counts from the main peak and, for another, placed behind the minor peak, namely on its trailing edge. Therefore, one would not expect the OCOG-derived water level to be more precise in this epoch. However, what becomes noticeable when investigating all waveforms of that specific epoch is that they vary significantly in size and shape, hence delivering fluctuating water level estimates within one satellite crossing. Therefore, some water levels are higher and some remain lower. All of the above timeseries are downsampled for visualization purposes and reveal the median water level of every epoch. In this epoch, there were 28 measurements. Consequently, noisy waveforms and multi-peaks have a considerable influence on the median. One can conclude that this offset does not occur for every measurement and that the water level in this epoch derived from the OCOG-retracker performed better throughout all the measurements of this cycle.

In the remaining lake cases there is an interesting reoccurring characteristic in the maximum-based water level timeseries. In some cases more than the other, the maximum-based retracker produces water levels with near-constant offsets mostly around a meter to the in-situ data and a few of the other graphs. This can particularly be seen in the Lake Constance (S3B), Lake Zurich (S3A) and Lake IJssel (S3A & S3B) cases (figures 4.15, 4.16, 4.18 and 4.19). Evidently, this characteristic is of systematic nature. In the previous subsection we explain that the maximum-based retracker is especially susceptible to waveforms of lower peakiness and multi-peaks when it comes to water level retrieval. The fact that this constant offset occurs in four of the lake cases supports our previous statement because many of the waveforms returned to the altimeter over lakes are considerably low in peakiness and reveal multi-peaks. This can be attributed to the surface roughness of large lakes which resemble the behavior of the open ocean (Boy et al., 2021). The initial retrackers and the other two new retrackers appear to perform better against

waveforms returned to the altimeter from lake surfaces. Overall, they follow similar trends and reveal comparable variability.

To stress some further flaws of the new retrackers, the Lake Zurich (S3A) case demonstrates several outliers visible as deep valleys in the timeseries (figure 4.16). Among them, the most notable outliers are derived from the mulitplication- and addition-based retrackers and are apparent between the 2017 and 2018 marks. These epochs are also dominated by noisy waveforms with multi-peaks where the median water level calculation remains erroneous. Nonetheless, in the same epochs outliers of somewhat lesser intensity also occur in the water level timeseries from the initial retrackers. This comes to show that the given retrackers have trouble dealing with waveforms of lower peakiness and with multi-peaks. In the Lake Zurich (S3B) case, it appears that most retrackers fail to resemble the trend of the in-situ water levels. This is particularly interesting since this case would presumably present a favorable validation scenario due to the proximity of the virtual station to the local gauge in Schmerikon. The two figures representing Lake IJssel (figures 4.18 and 4.19) are much alike each other and therefore can briefly be analyzed together. What stands out the most is the fact that different retrackers generate water levels with nearly constant offsets to one another. In both cases the OCOG-retracked timeseries resembles the in-situ data the most. All the other graphs however depict offsets beginning at a few decimeters and ending around one meter. The largest offsets are produced by the maximum-based retracker (higher than in-situ water levels) and by the Ocean-retracker (lower than in-situ water levels). The variability for the most part is seemingly low though. To explain these offsets one must comprehend the complex scenario at Lake IJssel. The local gauge is located in Lelystad by the weir which regulates the water flowing into the lake. The altimetric measurements take place over a large portion of the lake, many of which are more towards the middle of the lake. Hence, waveforms returned to the altimeter are very likely to be noisy and dominated by multi-peaks. Moreover, with the lake's dynamics being regulated, it is possible that there are even some surface elevation differences due to sudden influxes of water volumes propagating through the water body.

4.5 Validation

Now that new retrackers' performances have been thoroughly analyzed and assessed on a visual level we need to express some of these findings in numbers. To this end, we calculate some of the metrics presented in chapter 3 again for the OCOG-, Ocean- and all the new retrackers to obtain a direct comparison and overlook. Herein, we follow the suggestion presented in Lorenz et al. (2014) to limit our comparison to the correlation coefficient, the relative bias (also known as percentage bias) and the Nash-Sutcliffe-Efficiency. According to their assessment, this setup provides a sufficient and balanced overview on the quality of the generated water level timeseries with respect to the local gauge data. We omit the IceSheet, Ice and SeaIce retrackers from this comparison as they fail to provide an appropriate amount of water level estimates throughout the study period. In the previous section it was partly discernible that water levels from these retrackers only appear at arbitrary epochs, if at all. Therefore, providing a statistic for these retrackers would be a misleading quantification due to the lack of data.

Figures 4.21, 4.22 and 4.23 present a graphic overview of the retrackers' performances based on the correlation coefficient, relative bias and Nash-Sutcliffe-Efficiency for each virtual station. In each figure, the color coding is adjusted as such that the blue cells correspond to good, the

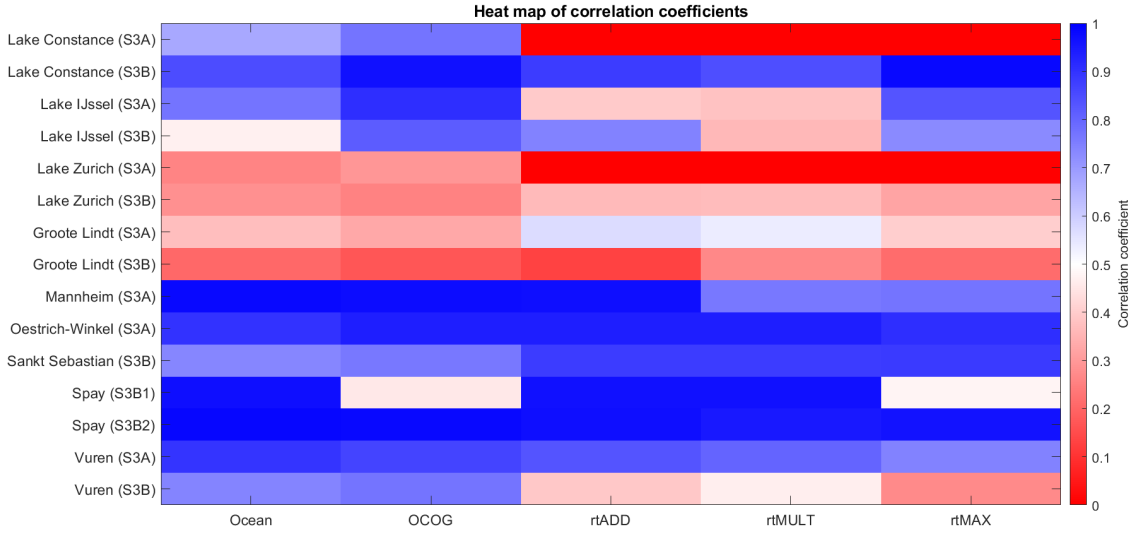

Figure 4.21: *A heat map of correlation coefficients for designated retrackers and all virtual stations*

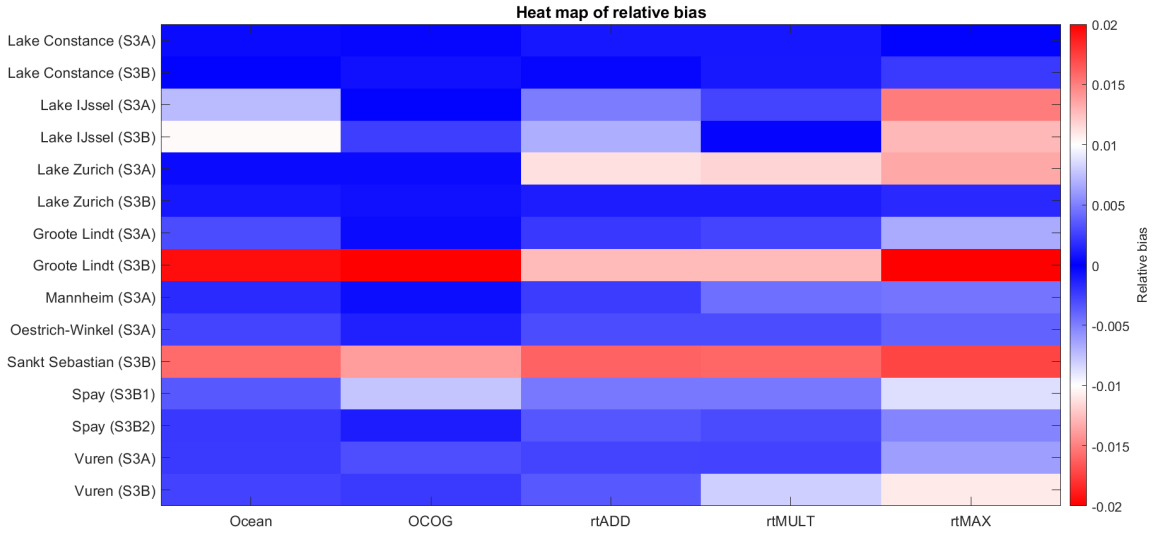

Figure 4.22: *A heat map of relative biases for designated retrackers and all virtual stations*

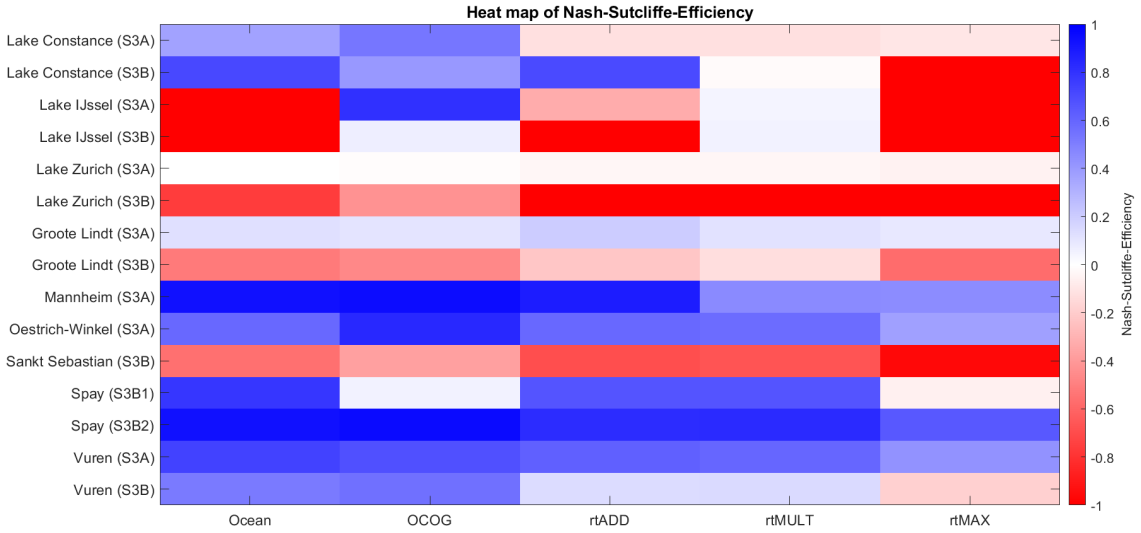

Figure 4.23: *A heat map of Nash-Sutcliffe-Efficiencies for designated retrackers and all virtual stations*

white to mediocre and the red to poor performances. In the heat map presenting the correlation coefficients (figure 4.21), it becomes noticeable that there are a few virtual stations where all retrackers perform very similar. Firstly, both Lake Zurich and Groote Lindt cases reveal near-zero or below zero correlations (beyond the color scale). This quantification goes hand in hand with our visual analysis from the previous section where we elaborated that mostly all retrackers have trouble retrieving the correct water level. Interestingly, the addition-based and multiplication-based retrackers come out with a medium-level performance in the Groote Lindt (S3A) case and thus clearly outperform the other retrackers of poor performance. This was also detected in the water level timeseries in figure 4.11 where many of the given retrackers produced huge individual outliers apart from the addition- and multiplication-based. Secondly, the previous statement can be turned around in the sense that in other examples, all retrackers perform similarly well. This can be seen in the Lake Constance (S3B), Oestrich-Winkel, Sankt Sebastian, Spay (S3B2) and Vuren (S3A) cases. In these cases it is also discernible from the timeseries that variability among the given graphs remains relatively low and with respect to the in-situ data. It is, in particular, interesting to see that the retrackers' timeseries to are fairly high-correlated with the local gauge data in the Sankt Sebastian case. Here, figure 4.8 demonstrates a considerable offset between the altimetric and in-situ water levels. This comes to show that the correlation coefficient only provides common information between the two, and is less sensitive to the amplitude and mean value. Over Mannheim, the Ocean-, OCOG- and addition-based retrackers achieve very high correlations to the in-situ data whereas the remaining two reveal correlations between 0.7 and 0.8. It is very likely that these lower correlations are related to the huge outlier occurring in their water level timeseries. In both Lake IJssel cases the performances among retrackers appear to vary the most in the heat map. What becomes clear however, is that the OCOG and maximum-based retrackers produce water levels with highest correlations to in-situ data when compared to the others. Finally, the most evident variation in performances can be taken from the Lake Constance (S3A) case. Here, the initial two retrackers' water levels correlate on a medium-high level with the in-situ data whereas all new retrackers reveal near-zero to negative correlations. To a less drastic extent this can also

be detected at Lake Zurich (S3A). In both cases the initial retrackers either produce no huge outliers or at least with lesser amplitude than those of the new retrackers.

In the heat map of the relative biases presented in figure 4.22, two cases immediately stand out where all retrackers perform similarly poor. For one, the Groote Lindt (S3B) case shows fairly high to very high relative biases and, for another, the Sankt Sebastian case also reveals fairly high values. For Sankt Sebastian this can be explained by the evident constant offset between the altimetric and in-situ timeseries. This was not taken into account by the calculation of the correlation coefficient, but clearly impacts the relative bias in this figure. In the Groote Lindt (S3B) scenario, there partly is a persistent offset on the one hand, and on the other hand there are vast outliers to the referential in-situ data among the Ocean-, OCOG- and maximum-based retrackers. Outliers do also occur from the addition- and multiplication-based retrackers, but remain lower in amplitude which explains the lighter color coding in the figure. Quite astoundingly, both Lake Constance cases demonstrate very low relative biases even though, especially among the new retrackers, a few big outliers can be seen. One can only assume that they do not affect the long-term mean enough to make a difference. Interestingly, in the Lake IJssel cases, the situation for the new retrackers is reversed to the heat map of the correlation coefficients. The maximum-based retracker produces the largest relative bias, and the remaining two perform well. Only the OCOG retracker can compete with these two according to figure 4.22. In the Mannheim case, the previous finding can be confirmed that the long-term mean is not affected enough by the occurring individual outlier. The OCOG-retracker does produce the water level timeseries with the least relative bias to in-situ data, yet the difference to the remaining retrackers is not as significant as highlighted in the correlation coefficients. Oestrich-Winkel is a case where the two heat maps and the timeseries in figure 4.4 are in agreement that the given retrackers perform decently to well with slight advantage from OCOG. Finally, the remaining virtual stations from Spay and Vuren all reveal medium-low to low relative biases with the exception of the maximum-based retracker in Vuren (S3B). This finding was made in the previous section as well where we address the fact that the maximum-based retracker shows near-constant biases to the other altimetric and locally gauged water levels. Among these, the tendency for better performances is shifted more towards the initial retrackers.

In the last heat map presented in figure 4.23 there are a few similar findings at first sight, but some other characteristics in the color coding arise that seem less conclusive. Similar are those in the bottom half of the heat map for stations Mannheim to Vuren (S3B). Here, the aforementioned tendencies of the initial retrackers performing better than the new ones persist (Sankt Sebastian and OCOG-NSE excluded). Just as in figure 4.22, Sankt Sebastian shows lacking quality assessed by the NSE. Oestrich-Winkel again proves to be a very favorable case in general, where all retrackers perform decently with a slight advantage from OCOG. In the top half of the heat map, Lake Constance (S3A) clearly shows a big advantage of the initial retrackers over the new ones. This finding at least, agrees to the heat map of correlations coefficients. However, the Lake Constance (S3B) case evidently opposes the previous to figures stating that multiplication- and maximum-based retrackers clearly underperform with low and very low NSE values, respectively. This does demonstrate a plausible finding though as the NSE essentially takes into account the phase, amplitude and mean value which all deviate to certain extents from the in-situ data (see figure 4.15). A similar statement can be made for the Lake IJssel cases, with the difference that the initial retrackers do not perform well either. Only the OCOG-retracker reveals high NSE values in the Lake IJssel (S3A) case. In the Lake Zurich (S3A) case there seem to be hardly any variations among the NSE values reached by all given retrackers which is rather confusing due to the outlying peaks of the timeseries in figure 4.16. From

the Lake Zurich (S3B) case in figure 4.17 and the current heat map, one can see that no retracker particularly performs well. Highlighted are the new ones which clearly underperform in contrast with the initial ones. At last, the variation among NSE values for the Groote Lindt case are alike those presented in the heat map of relative biases. The difference to mention here is that for the Groote Lindt case the retrackers' performances are assessed as moderately high as opposed to fairly high in relative biases. This also applies to the other Groote Lindt case, yet in the opposite direction. Namely, relative biases formerly assessed as fairly low are moderately low in figure 4.23.

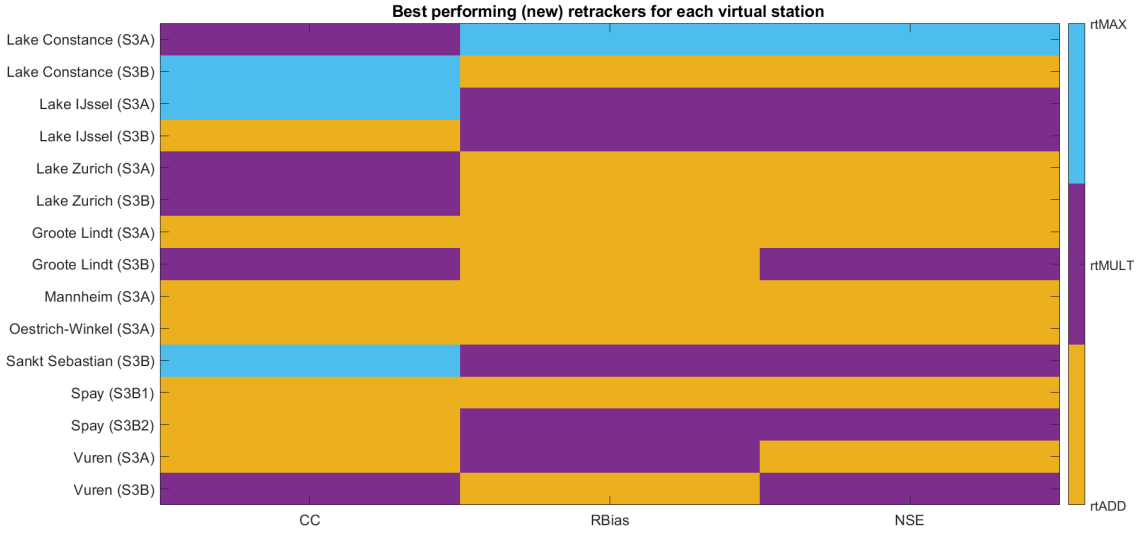

Figure 4.24: *A visual presentation of the best (new) retrackers for each virtual station based on the three given metrics*

To conclude this chapter, we first determine the best retracker among the new ones presented in this study and, second, conduct a direct comparison to the initial retrackers. To this end, based on the three metrics, we color-code the best retracker for each virtual station. Figure 4.24 depicts this overview for the new retrackers designed in this study and figure 4.25 puts them to the test against the initial retrackers, Ocean and OCOG. In figure 4.24 it becomes very clear that the addition-based retracker is the overall winner among the new ones. This does not come to our surprise as its water level timeseries mostly had the least considerable outliers and quite decently followed the in-situ data in many cases. To a lesser but not insignificant extent, the multiplication-based retracker is also highlighted a fair amount times in figure 4.24. In last place is the maximum-based retracker, yet it is highlighted a few times as well in terms of a best performance. However, when exactly inspecting the figure, it becomes clear that the maximum-based retracker only stands a chance in the rather complicated scenarios, where the other retrackers have trouble, likewise.

Now against Ocean and OCOG presented in figure 4.25, the new retrackers do not show a dominating appearance anymore. One can discern from the figure the quality of the OCOG-retracker which is assessed as the best at least once in almost all virtual stations. Highlighted a decent amount of times is also the Ocean-retracker and thus remains overall better than the new retrackers of this study. Nonetheless, the new retrackers more or less share the stage among each other when it comes to their performances against the initial retrackers as they are

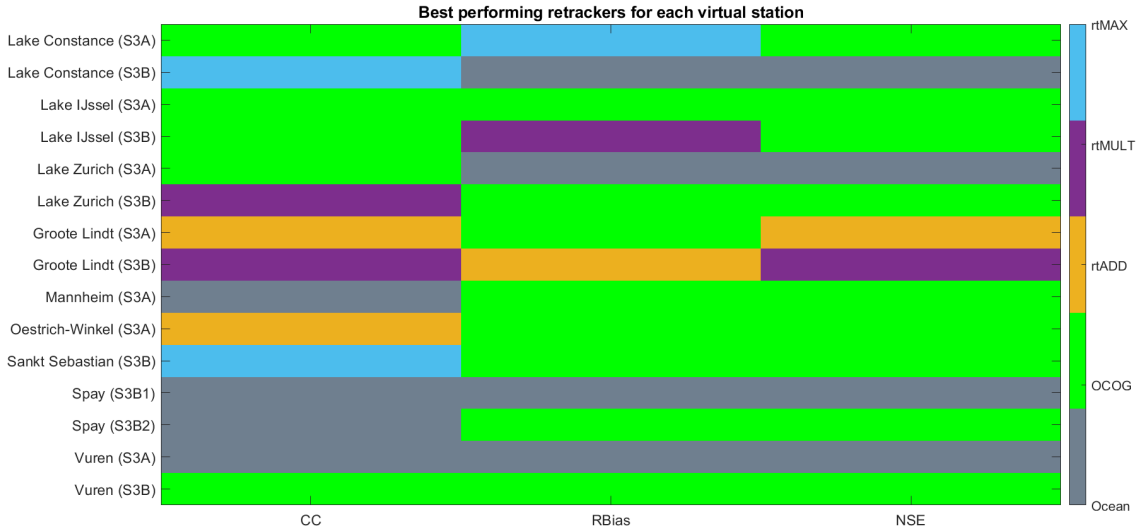

Figure 4.25: *A visual presentation of the best overall retrackers for each virtual station based on the three given metrics*

all highlighted a comparable amount of times. Some of which occur, again, at virtual stations where all retrackers seem to have trouble accurately retrieving water levels. However, the addition-based retracker does get highlighted in the Oestrich-Winkel case which underlines its great performance since this case was a rather favorable one for all retrackers. Likewise, in the Groote Lindt (S3A) case, it even appears to be the clear winner based on the correlation coefficient and the NSE.

In conclusion, the previous two figures demonstrate that the new retrackers do outperform the initial retrackers for some of the more complicated virtual stations. What these figures do not show though, is how close the call was for the determination of the best-performing with respect to successive ranks. For this question, the heat maps and water level timeseries were plotted earlier. Herein, the new retrackers oftentimes prove to keep up with the Ocean- and OCOG-retrackers, but undergo a slight disadvantage. Not to mention the fact that the three remaining retrackers dedicated to the Sentinel-3 mission in most cases fail to provide consistent water level estimates. Consequently, it is safe to say that the new retrackers are far more suitable for the presented case studies than the Ice-, SeaIce- and IceSheet-retrackers and stand a chance against the Ocean-/OCOG-retrackers in many other cases.

Chapter 5

Conclusion and outlook

In this study, which was driven by the aim to better understand the limitations of Sentinel-3 inland altimetry by means of validating its measurements over the Rhine, we conducted a thorough preliminary analysis which subsequently lead us to our presented methodology. Herein, we designed three new stochastic-based retrackers to compete against the ones dedicated to the Sentinel-3 mission.

In our preliminary analysis we first made some very interesting discoveries when it comes to the performances of retrackers and the applied geophysical corrections. Following an extensive assessment of all possible permutations of each and every given retracker with respect to the local gauge data, we confirmed the presumption that the best expert-judged set of geophysical corrections does not necessarily yield the best results. As a matter of fact, over the entirety of river and lake cases, which were investigated separately, our outcome demonstrates the ECMWF-model at zero altitude to be the most favorable for the largest signal delay component, the dry troposphere. For the other two considerable components, the wet troposphere and ionosphere, it was interesting to see that corrections determined by the radiometer and altimeter themselves were preferred over the expert-judged models. The GIM-model although does share the stage with the corrections from the altimeter in pseudo low resolution mode for the ionospheric component which would comply with the experts' judgment. The OCOG-retracker indeed proved to deliver the best results with respect to the in-situ data which further agrees with the experts' judgment.

In the continuation of chapter 3 we presented a reverse retracking approach in the sense that we use the given in-situ data to determine the offset to each altimetry-derived measurement of every epoch. Under the assumption that these offsets are legitimate, they could be seen as an a-posteriori correction which we projected onto the range estimate between the altimeter and the target, in other words on a waveform level. Using the median and standard deviation of these a-posteriori corrections over all permutations of each retracker and notably for each sampling point in a satellite's bypass, we analyzed the relationship they have to waveform properties of the same epoch. Firstly, a clear trend became apparent that peakier waveforms need corrections of lesser magnitude whereas lower ranges of peakiness/kurtosis values yield higher a-posteriori corrections to the respective retracking gates. It was also interesting to see the role the water body itself plays. Namely, for river cases we demonstrated that measurements near the banks return noisier waveforms than towards the middle of the river. Therefore, the a-posteriori corrections to the retracking gates were higher. Other indicators such as the maximum power of waveforms and the relative bias to the sinc^2-function lead to the same conclusions. For the lake cases, the situation proved to be vice versa. The middle part of lakes seems to resemble ocean surfaces more than near-shoreline waters and therefore turns the aforementioned findings around.

Later, we presented three stochastic-based retrackers in the sense that the retracking gates should lie on the highest probability assigned to each and every bin of the waveform. To distribute the probabilities across all bins of the waveform, we considered three empirical approaches that take both the waveform itself and its first derivative into account: Addition, multiplication and maximum of both signals. The general idea of all three approaches is to emphasize critical parts of the waveform which are central to water level retrieval in satellite altimetry. The water levels we retrieve from the three new retrackers were plotted against the in-situ data and the Ocean- and OCOG-retrackers for a visual comparison. In many cases, all retrackers were in agreement for the most part of the timeseries. However, the new ones occasionally revealed big outliers which are attributed to the fact that, especially from the maximum-based retracker, less peaky waveforms and multi-peaks within impact the new retrackers' performances more than the initial ones. Among the new retrackers the addition-based outperformed the others and proved to be the most favorable. The multiplication-based retracker however, also showed a decent level of suitability after being highlighted quite a few times as the best-performing. The maximum-based retracker is the odd one out which not only in the timeseries but also in the heat maps and overview of best-performances presented the least favorable results. We put all new retrackers of this study to the test against the Ocean- and OCOG-retrackers and conclude that they only perform better over certain virtual stations, in particular those where all retrackers had trouble resembling the local gauge data. However, the heat maps in chapter 4 demonstrated that the new ones do keep up with Ocean and OCOG-retrackers and only undergo a slight disadvantage. In most cases the slight disadvantage was traced back to some individual outliers where the new retrackers were more susceptible to noisy waveforms and multi-peaks than the initial ones.

5.1 Outlook

All in all, the new stochastic-based retrackers of this study proved to be very suitable for water level retrieval and keep up with the performances of the Ocean- and OCOG-retrackers despite their slight disadvantage toward them. At last, it essentially comes down to the few large outliers they produce and a small bin-difference among the determined retracking gates. In the cases where the performances were nearly equal, it is a matter of one or two bins that leads to varying water levels. Further optimization would therefore require investigating which bin precisely yields the correct one for water level retrieval starting from the bottom of the leading edge and ending at the peak of the waveform. Subsequently, such information could be taken into account and further emphasized by the empirical approaches. The other aspect in need for optimization is the significant occurrences of large outliers from noisy and multi-peak waveforms. The new retrackers would need to be more robust towards waveforms with such properties or else their usability over lakes and complicated river scenarios will be questionable. In this case, it is very likely that a combination of the three new retrackers or more would ignore outlying retracking gates and determine a more appropriate median one instead. In the future, stochastic approaches should be taken more into consideration due to the presented relationship between assigned waveform-bin probabilities and RMSE to the local gauge data. Stochastic approaches could provide a new era of retracking methods when investigated and enhanced thoroughly.

Bibliography

Ablain, M., Legeais, J., Prandi, P., Marcos, M., Fenoglio-Marc, L., Dieng, H., Benveniste, J. and Cazenave, A. (2017), Satellite altimetry-based sea level at global and regional scales, *in* 'Integrative study of the mean sea level and its components', Springer, pp. 9–33.

Biancamaria, S., Lettenmaier, D. P. and Pavelsky, T. M. (2016), The SWOT mission and its capabilities for land hydrology, *in* 'Remote sensing and water resources', Springer, pp. 117–147.

Bosseler, B., Salomon, M., Schlüter, M. and Rubinato, M. (2021), 'Living with urban flooding: A continuous learning process for local municipalities and lessons learnt from the 2021 events in Germany', *Water* **13**(19), 2769.

Bourg, L., Bruniquel (ACRI-ST), J., Morris, H., Dash (University of Southampton), J., Preusker (FUB), R. and Dransfeld (ESA), S. (2021), 'Copernicus Sentinel-3 OLCI Land User Handbook'.

Boy, F., Crétaux, J.-F., Boussaroque, M. and Tison, C. (2021), 'Improving Sentinel-3 SAR Mode Processing Over Lake Using Numerical Simulations', *IEEE Transactions on Geoscience and Remote Sensing* **60**, 1–18.

Brönmark, C. and Hansson, L.-A. (2002), 'Environmental issues in lakes and ponds: current state and perspectives', *Environmental conservation* **29**(3), 290–307.

Buckley, S., Agram, P., Belz, J., Crippen, R., Gurrola, E., Hensley, S., Kobrick, M., Lavalle, M., Martin, J., Neumann, M. et al. (2020), 'NASADEM User Guide v1', *National Aeronautics and Space Administration: Washington, DC, USA* .

Cartwright, D. and Edden, A. C. (1973), 'Corrected tables of tidal harmonics', *Geophysical journal international* **33**(3), 253–264.

Chelton, D. B., Ries, J. C., Haines, B. J., Fu, L.-L. and Callahan, P. S. (2001), Satellite altimetry, *in* 'International geophysics', Vol. 69, Elsevier, pp. 1–ii.

Cioc, M. (2002), *The Rhine: an eco-biography, 1815-2000*, University of Washington Press.

Date, E. (2016), 'GMES space component sentinel-3 payload data ground segment products definition document'.

Deng, X. (2003), Improvement of geodetic parameter estimation in coastal regions from satellite radar altimetry, PhD thesis, Curtin University of Technology Bentley, Australia.

Dinardo, S., Fenoglio-Marc, L., Becker, M., Scharroo, R., Fernandes, M. J., Staneva, J., Grayek, S. and Benveniste, J. (2021), 'A RIP-based SAR retracker and its application in North East Atlantic with Sentinel-3', *Advances in Space Research* **68**(2), 892–929.

Donlon, C. J., Cullen, R., Giulicchi, L., Vuilleumier, P., Francis, C. R., Kuschnerus, M., Simpson, W., Bouridah, A., Caleno, M., Bertoni, R. et al. (2021), 'The Copernicus Sentinel-6 mission: Enhanced continuity of satellite sea level measurements from space', *Remote Sensing of Environment* **258**, 112395.

EUMETSAT (2019), *Principles of measuring the oceans from space*, chapter 3.

Field, C. B., Barros, V., Stocker, T. F. and Dahe, Q. (2012), *Managing the risks of extreme events and disasters to advance climate change adaptation: special report of the intergovernmental panel on climate change*, Cambridge University Press.

Fu, L.-L. and Cazenave, A. (2000), *Satellite altimetry and earth sciences: a handbook of techniques and applications*, Elsevier.

Fu, L.-L., Christensen, E. J., Yamarone Jr, C. A., Lefebvre, M., Menard, Y., Dorrer, M. and Escudier, P. (1994), 'TOPEX/POSEIDON mission overview'.

Gao, Q., Makhoul, E., Escorihuela, M. J., Zribi, M., Quintana Seguí, P., García, P. and Roca, M. (2019), 'Analysis of retrackers' performances and water level retrieval over the ebro river basin using sentinel-3', *Remote Sensing* **11**(6), 718.

Ho, S. (2017), 'Introduction to transboundary river cooperation: actors, strategies and impact'.

Jiang, L., Nielsen, K., Dinardo, S., Andersen, O. B. and Bauer-Gottwein, P. (2020), 'Evaluation of Sentinel-3 SRAL SAR altimetry over Chinese rivers', *Remote Sensing of Environment* **237**, 111546.

Lillibridge, J., Smith, W. H., Sandwell, D., Scharroo, R., Lemoine, F. and Zelensky, N. (2006), '20 Years of Improvements to GEOSAT Altimetry', *ESA Special Publication* **614**, 75.

Liu, D. (2020), 'A rational performance criterion for hydrological model', *Journal of Hydrology* **590**, 125488.

Lorenz, C., Kunstmann, H., Devaraju, B., Tourian, M. J., Sneeuw, N. and Riegger, J. (2014), 'Large-scale runoff from landmasses: a global assessment of the closure of the hydrological and atmospheric water balances', *Journal of Hydrometeorology* **15**(6), 2111–2139.

Marth, P. C., Jensen, J. R., Kilgus, C. C., Perschy, J. A., MacArthur, J. L., Hancock, D. W., Hayne, G. S., Purdy, C. L., Rossi, L. C. and Koblinsky, C. J. (1993), 'Prelaunch performance of the NASA altimeter for the TOPEX/Poseidon project', *IEEE Transactions on Geoscience and remote sensing* **31**(2), 315–332.

Martin, T. V., Zwally, H. J., Brenner, A. C. and Bindschadler, R. A. (1983), 'Analysis and retracking of continental ice sheet radar altimeter waveforms', *Journal of Geophysical Research: Oceans* **88**(C3), 1608–1616.

Nielsen, K., Andersen, O. B. and Ranndal, H. (2020), 'Validation of Sentinel-3A based lake level over US and Canada', *Remote Sensing* **12**(17), 2835.

Passaro, M., Restano, M., Sabatino, G., Orrú, C. and Benveniste, J. (2020), The ALES+ SAR service for Cryosat-2 and Sentinel-3 at ESA GPOD, *in* 'OSTST 2020'.

Pekel, J.-F., Cottam, A., Gorelick, N. and Belward, A. (2016), 'High-resolution mapping of global surface water and its long-term changes', *Nature* **540**, 418–422.

Prigent, C., Papa, F., Aires, F., Rossow, W. B. and Matthews, E. (2007), 'Global inundation dynamics inferred from multiple satellite observations, 1993–2000', *Journal of Geophysical Research: Atmospheres* **112**(D12).

Ridley, J. and Partington, K. (1988), 'A model of satellite radar altimeter return from ice sheets', *Remote Sensing* **9**(4), 601–624.

Robinson, I. S. (2004), *Measuring the oceans from space: the principles and methods of satellite oceanography*, Springer Science & Business Media.

Rodriguez, E., Morris, C. S. and Belz, J. E. (2006), 'A global assessment of the SRTM performance', *Photogrammetric Engineering & Remote Sensing* **72**(3), 249–260.

Shu, S., Liu, H., Beck, R. A., Frappart, F., Korhonen, J., Xu, M., Yang, B., Hinkel, K. M., Huang, Y. and Yu, B. (2020), 'Analysis of Sentinel-3 SAR altimetry waveform retracking algorithms for deriving temporally consistent water levels over ice-covered lakes', *Remote Sensing of Environment* **239**, 111643.

Stammer, D. and Cazenave, A. (2017), *Satellite altimetry over oceans and land surfaces*, CRC press.

Tapley, B. D., Born, G. H. and Parke, M. E. (1982), 'The Seasat altimeter data and its accuracy assessment', *Journal of Geophysical Research: Oceans* **87**(C5), 3179–3188.

Toreti, A., Bavera, D., Acosta Navarro, J., Cammalleri, C., de Jager, A., Di Ciollo, C., Hrast Essenfelder, A., Maetens, W., Magni, D., Masante, D., Mazzeschi, M., Niemeyer, S. and Spinoni, J. (2022), 'Drought in Europe August 2022'.

Tourian, M. J. (2013), *Application of spaceborne geodetic sensors for hydrology*.

Tourian, M. J., Elmi, O., Shafaghi, Y., Behnia, S., Saemian, P., Schlesinger, R. and Sneeuw, N. (2022), 'HydroSat: geometric quantities of the global water cycle from geodetic satellites', *Earth System Science Data* **14**(5), 2463–2486.

Van Zyl, J. J. (2001), 'The Shuttle Radar Topography Mission (SRTM): a breakthrough in remote sensing of topography', *Acta Astronautica* **48**(5-12), 559–565.

Verron, J., Bonnefond, P., Andersen, O., Ardhuin, F., Bergé-Nguyen, M., Bhowmick, S., Blumstein, D., Boy, F., Brodeau, L., Crétaux, J.-F. et al. (2021), 'The SARAL/AltiKa mission: A step forward to the future of altimetry', *Advances in Space Research* **68**(2), 808–828.

Villadsen, H., Andersen, O. B., Stenseng, L., Nielsen, K. and Knudsen, P. (2016), The Multiple Waveform Persistent Peak (MWaPP) Retracker for SAR waveforms, *in* 'ESA Living Planet Symposium 2016'.

Wahr, J. M. (1985), 'Deformation induced by polar motion', *Journal of Geophysical Research: Solid Earth* **90**(B11), 9363–9368.

Appendix A

Presentation of the remaining virtual stations

To complement the scatter plots between the a-posteriori corrections and the waveform properties in chapter 3, we present the remaining virtual stations in this appendix.

A.1 River cases

Spay (S3B1)

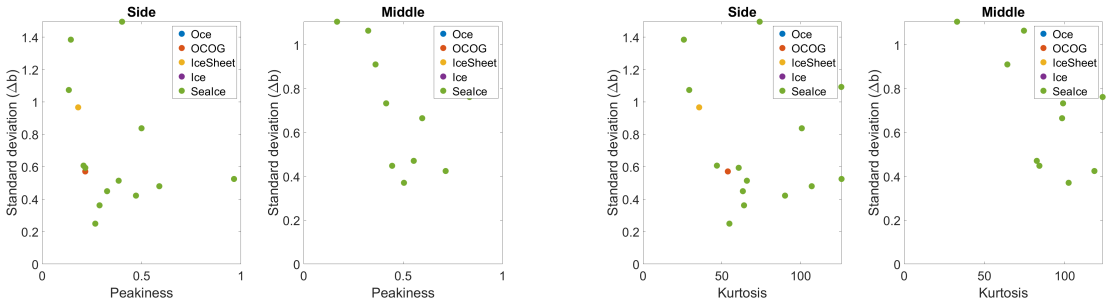

Figure A.1: *Spay (S3B1): Peakiness/kurtosis against standard deviation of a-posteriori corrections*

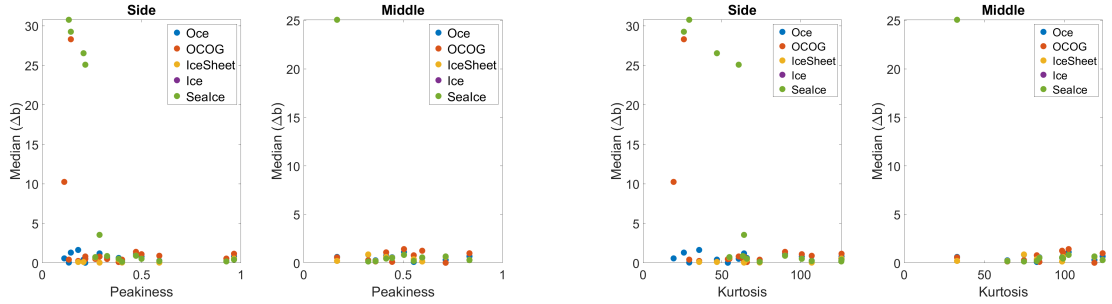

Figure A.2: *Spay (S3B1): Peakiness/kurtosis against median of a-posteriori corrections*

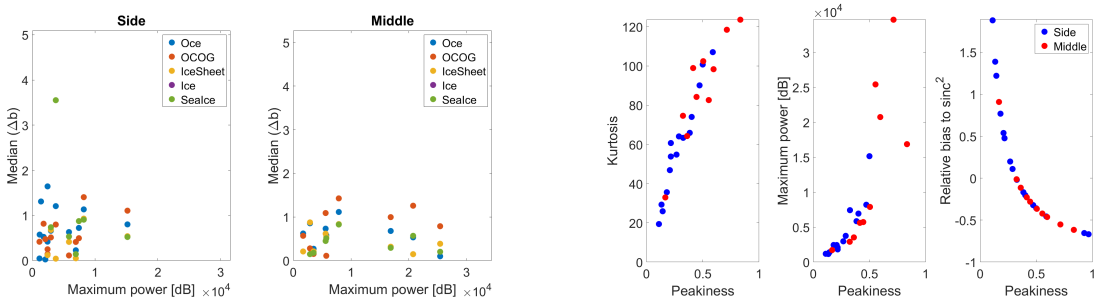

Figure A.3: *Spay (S3B1): Maximum power against median of a-posteriori corrections (left) and other waveform properties against each other (right)*

Spay (S3B2)

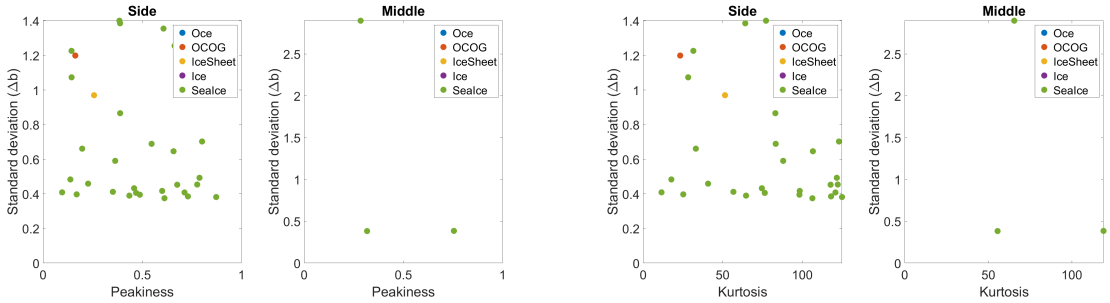

Figure A.4: *Spay (S3B2): Peakiness/kurtosis against standard deviation of a-posteriori corrections*

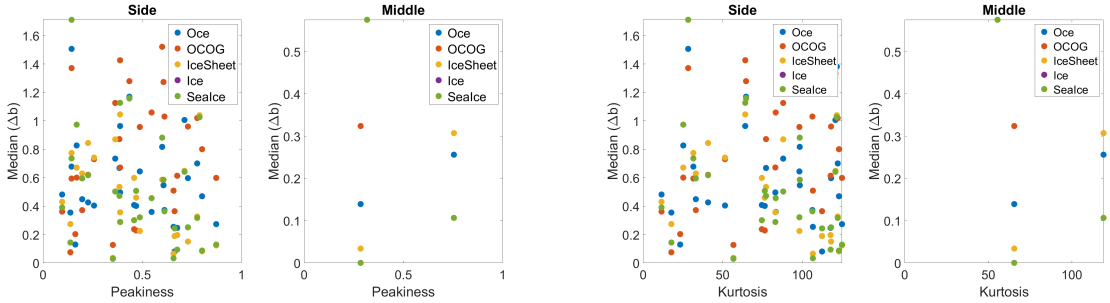

Figure A.5: *Spay (S3B2): Peakiness/kurtosis against median of a-posteriori corrections*

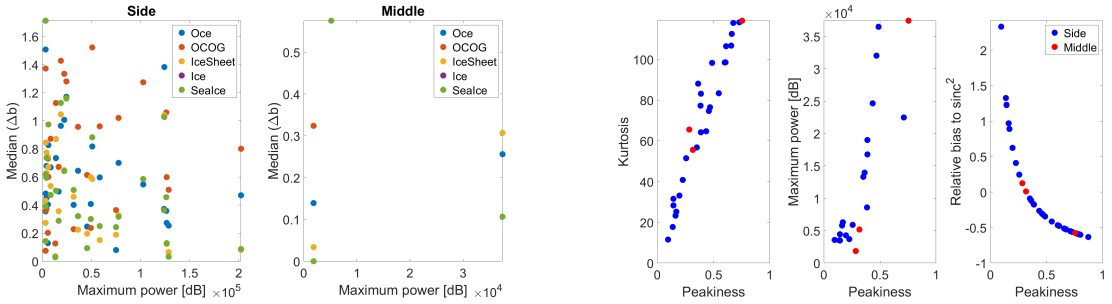

Figure A.6: *Spay (S3B2): Maximum power against median of a-posteriori corrections (left) and other waveform properties against each other (right)*

Mannheim (S3A)

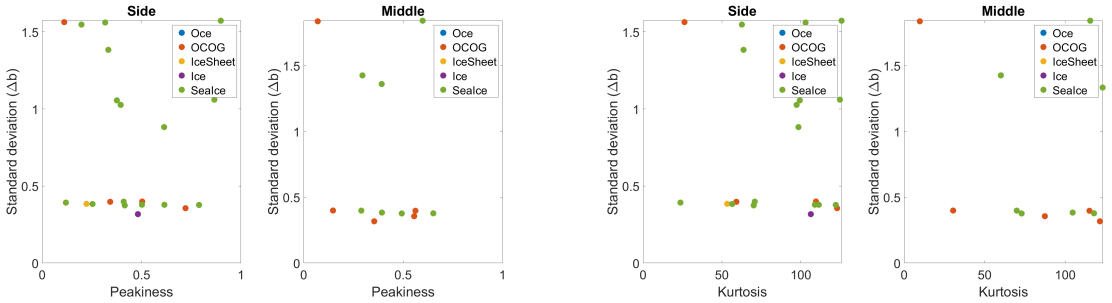

Figure A.7: *Mannheim (S3A): Peakiness/kurtosis against standard deviation of a-posteriori corrections*

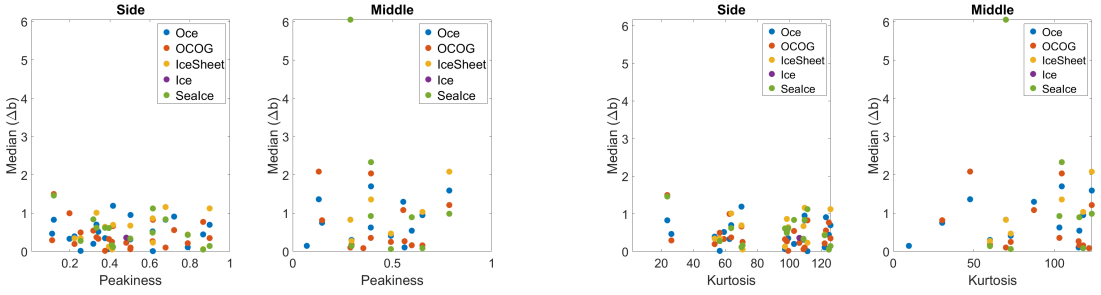

Figure A.8: *Mannheim (S3A): Peakiness/kurtosis against median of a-posteriori corrections*

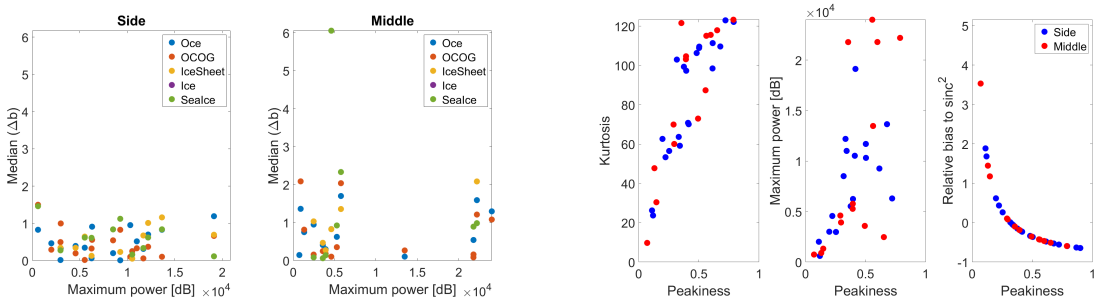

Figure A.9: *Mannheim (S3A): Maximum power against median of a-posteriori corrections (left) and other waveform properties against each other (right)*

Sankt Sebastian (S3B)

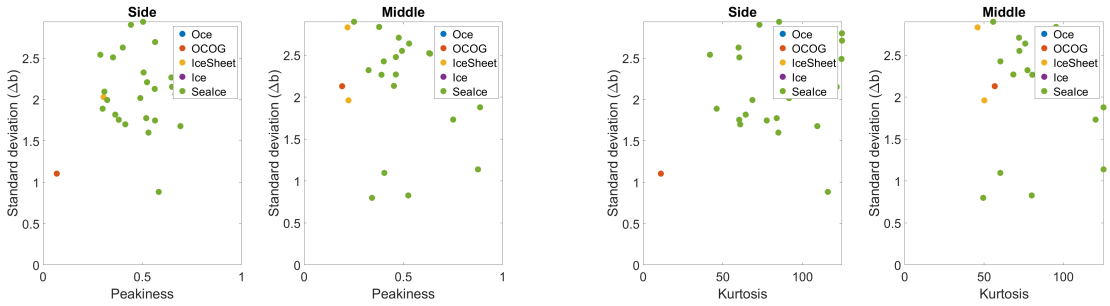

Figure A.10: *Sankt Sebastian (S3B): Peakiness/kurtosis against standard deviation of a-posteriori corrections*

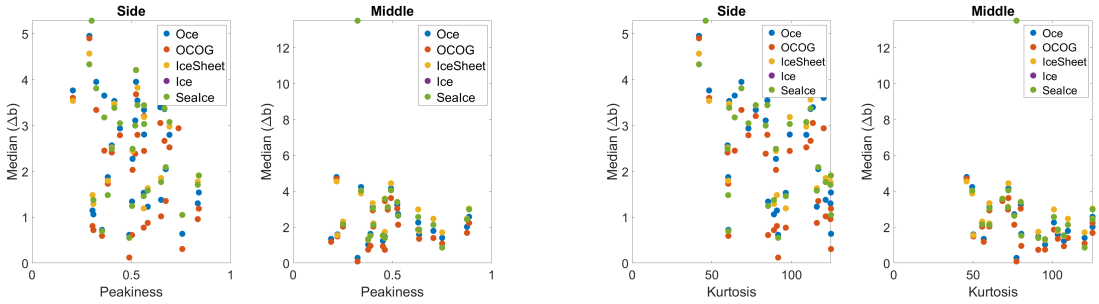

Figure A.11: *Sankt Sebastian (S3B): Peakiness/kurtosis against median of a-posteriori corrections*

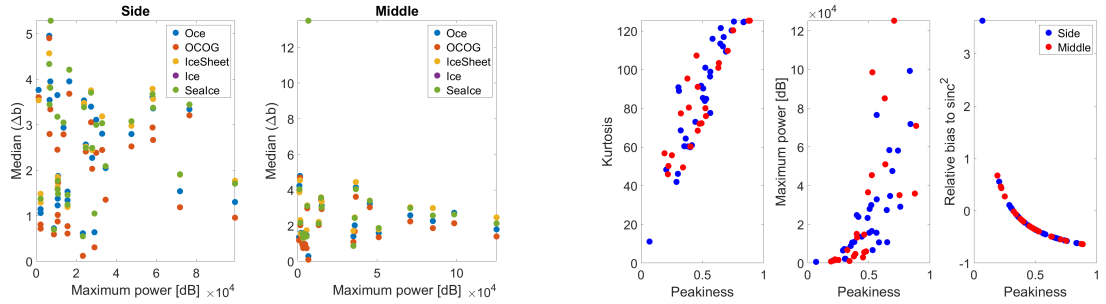

Figure A.12: *Sankt Sebastian (S3B): Maximum power against median of a-posteriori corrections (left) and other waveform properties against each other (right)*

Vuren (S3A)

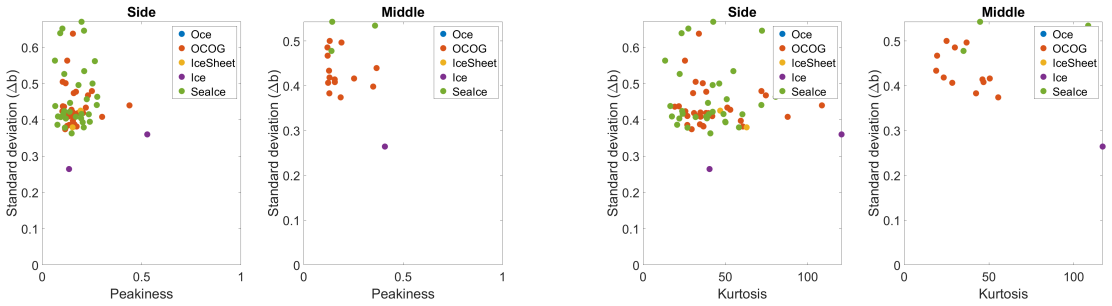

Figure A.13: *Vuren (S3A): Peakiness/kurtosis against standard deviation of a-posteriori corrections*

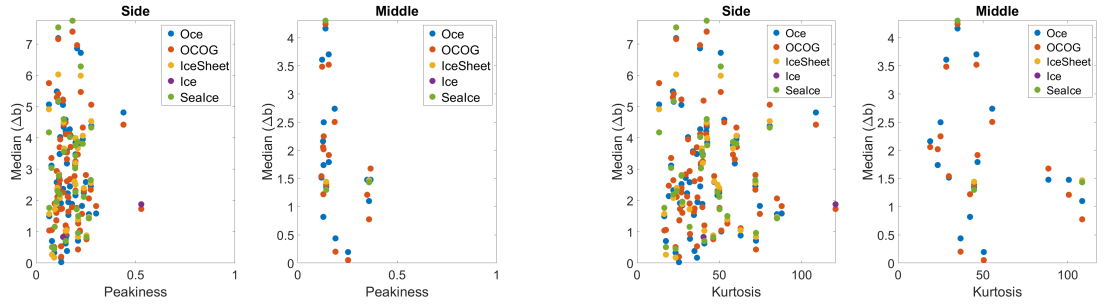

Figure A.14: *Vuren (S3A): Peakiness/kurtosis against median of a-posteriori corrections*

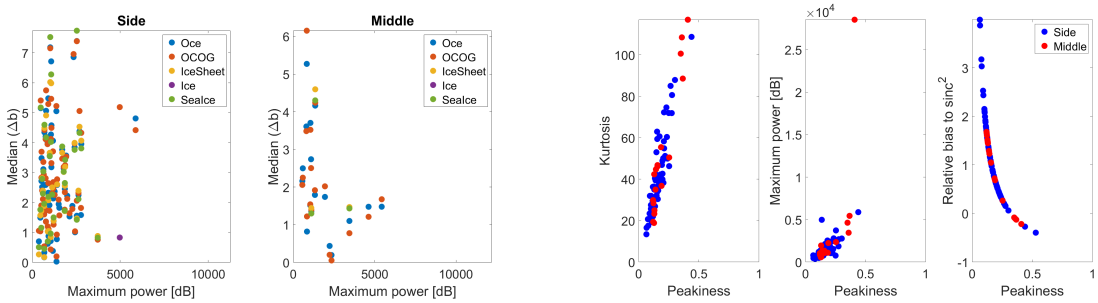

Figure A.15: *Vuren (S3A): Maximum power against median of a-posteriori corrections (left) and other waveform properties against each other (right)*

Vuren (S3B)

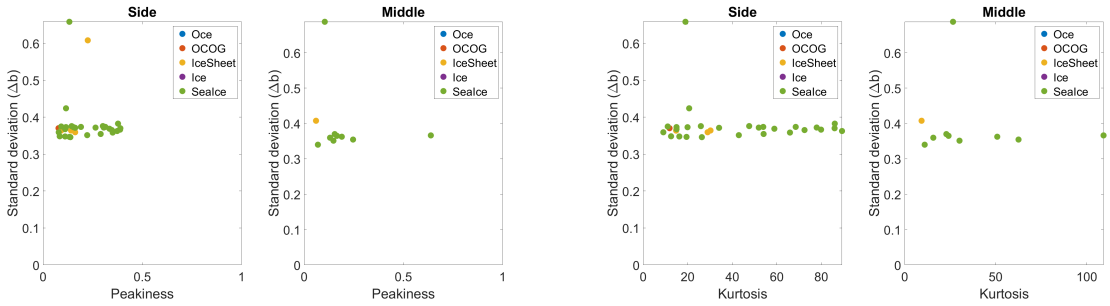

Figure A.16: *Vuren (S3B): Peakiness/kurtosis against standard deviation of a-posteriori corrections*

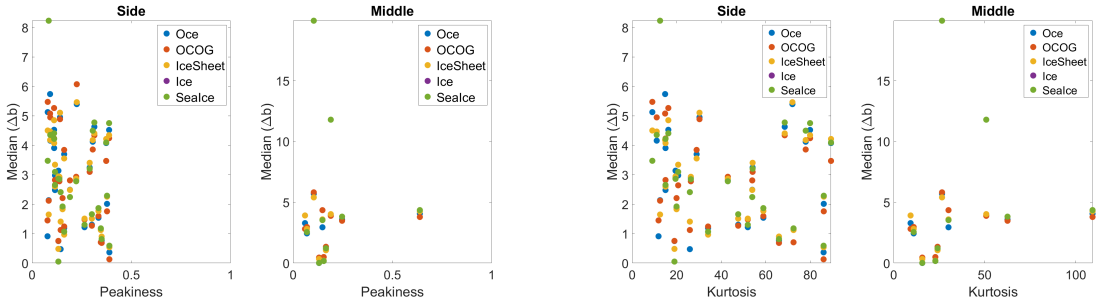

Figure A.17: *Vuren (S3B): Peakiness/kurtosis against median of a-posteriori corrections*

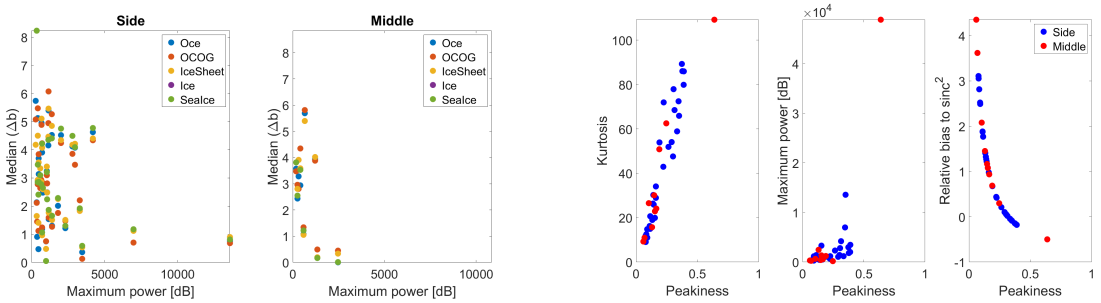

Figure A.18: *Vuren (S3B): Maximum power against median of a-posteriori corrections (left) and other waveform properties against each other (right)*

Groote Lindt (S3A)

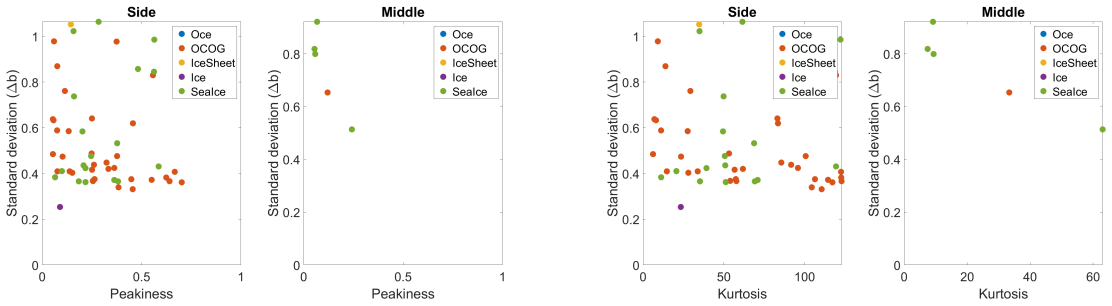

Figure A.19: *Groote Lindt (S3A): Peakiness/kurtosis against standard deviation of a-posteriori corrections*

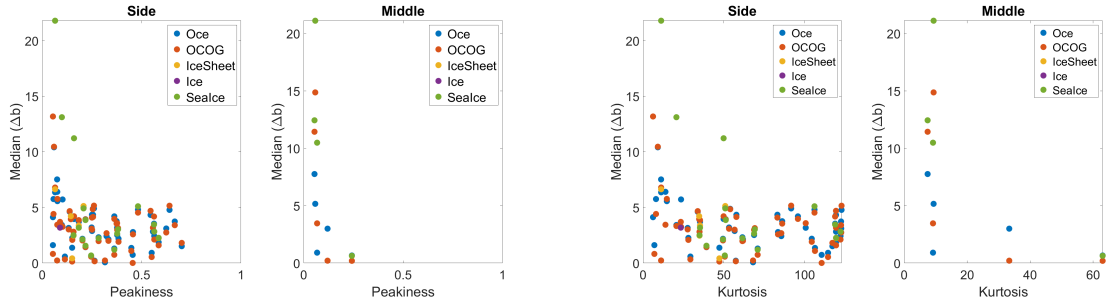

Figure A.20: *Groote Lindt (S3A): Peakiness/kurtosis against median of a-posteriori corrections*

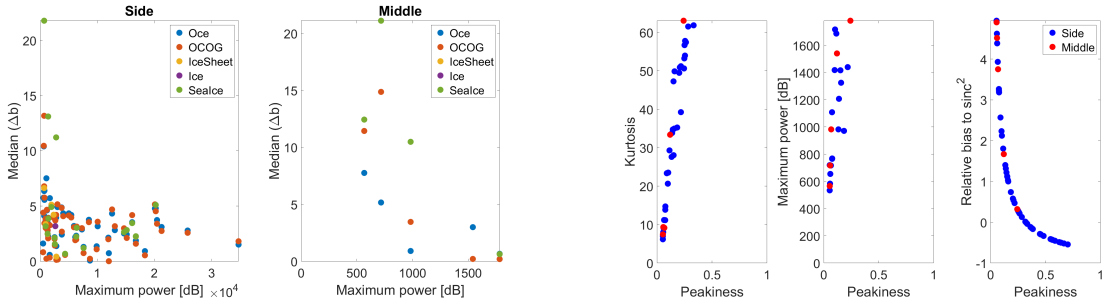

Figure A.21: *Groote Lindt (S3A): Maximum power against median of a-posteriori corrections (left) and other waveform properties against each other (right)*

Groote Lindt (S3B)

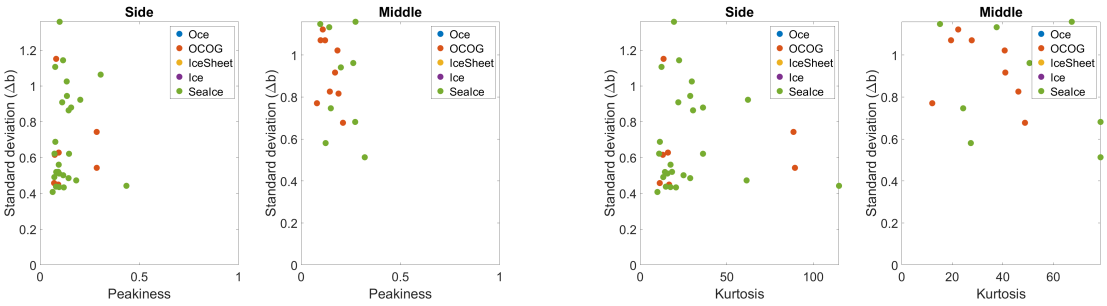

Figure A.22: *Groote Lindt (S3B): Peakiness/kurtosis against standard deviation of a-posteriori corrections*

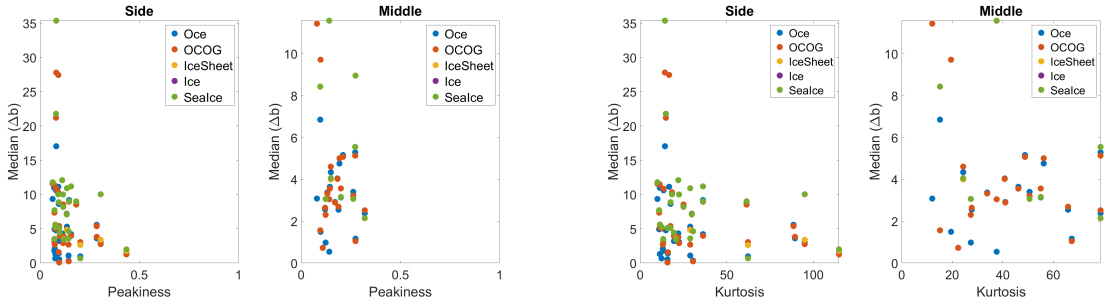

Figure A.23: *Groote Lindt (S3B): Peakiness/kurtosis against median of a-posteriori corrections*

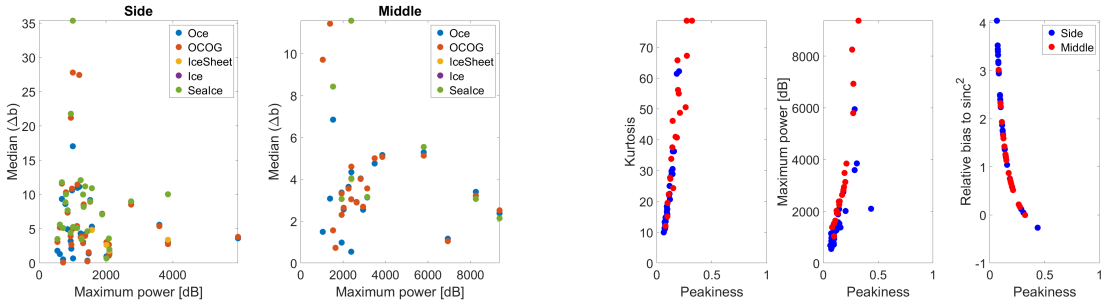

Figure A.24: *Groote Lindt (S3B): Maximum power against median of a-posteriori corrections (left) and other waveform properties against each other (right)*

A.2 Lake cases

Lake Constance (S3A)

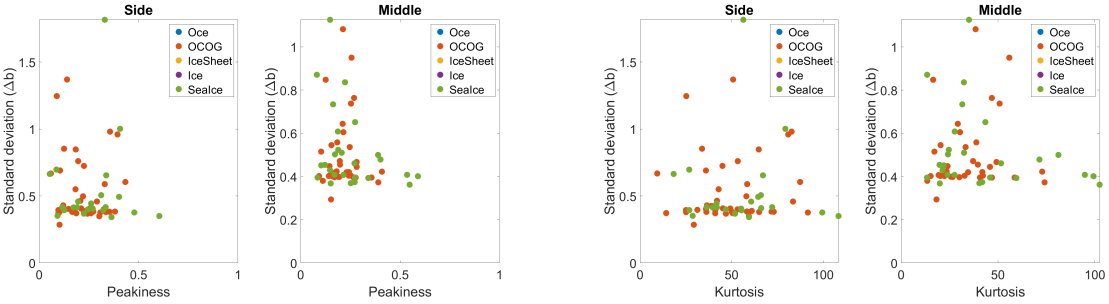

Figure A.25: *Lake Constance (S3A): Peakiness/kurtosis against standard deviation of a-posteriori corrections*

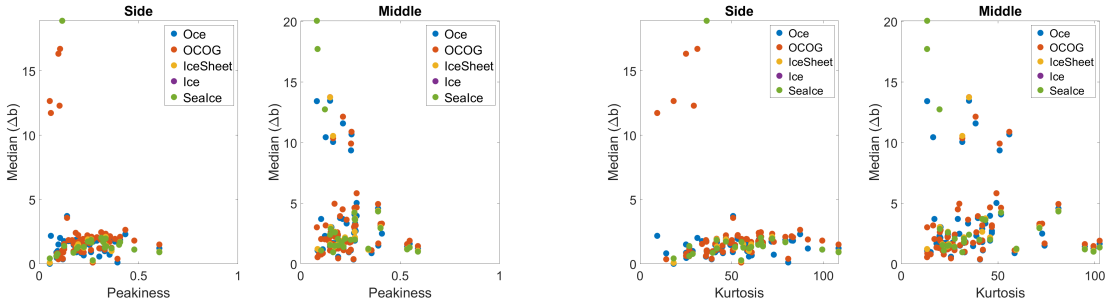

Figure A.26: *Lake Constance (S3A): Peakiness/kurtosis against median of a-posteriori corrections*

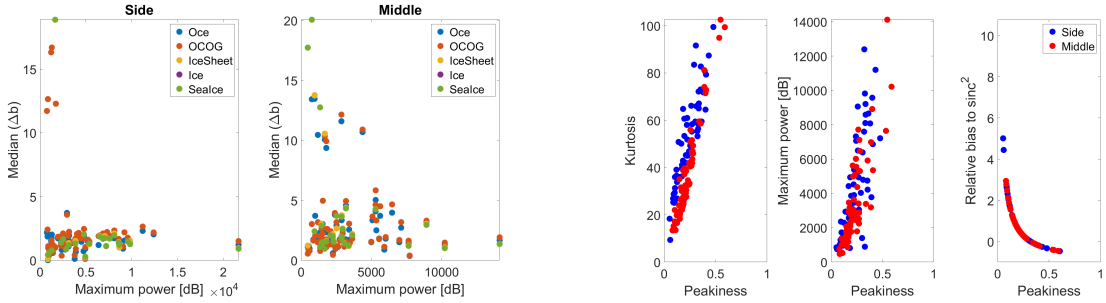

Figure A.27: *Lake Constance (S3A): Maximum power against median of a-posteriori corrections (left) and other waveform properties against each other (right)*

Lake Constance (S3B)

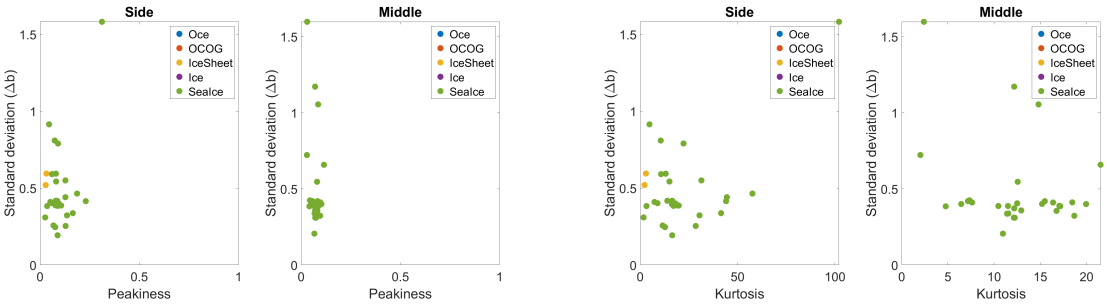

Figure A.28: *Lake Constance (S3B): Peakiness/kurtosis against standard deviation of a-posteriori corrections*

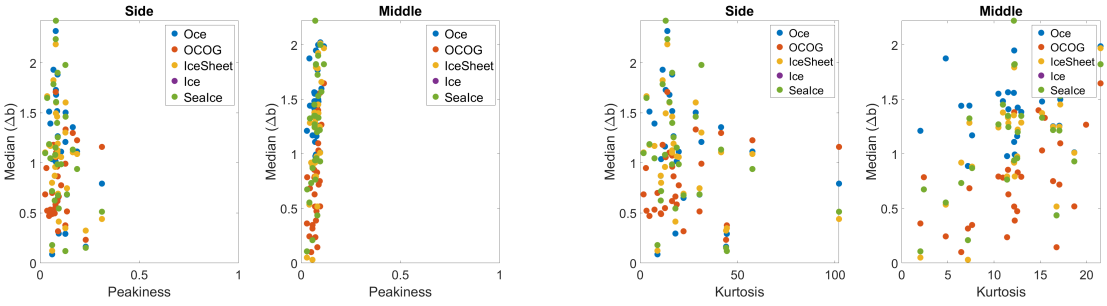

Figure A.29: *Lake Constance (S3B): Peakiness/kurtosis against median of a-posteriori corrections*

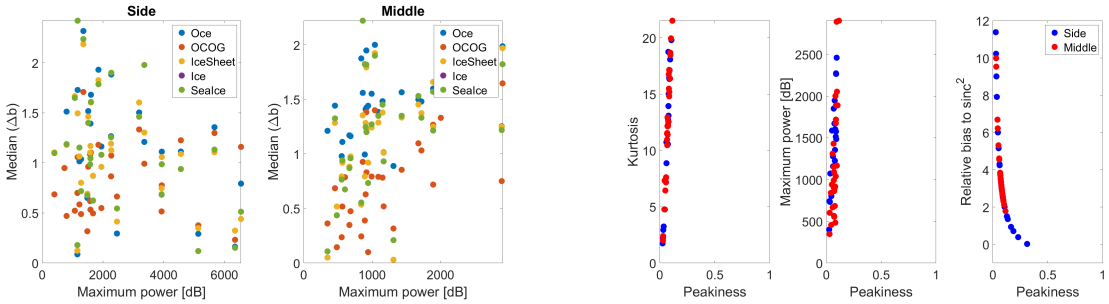

Figure A.30: *Lake Constance (S3B): Maximum power against median of a-posteriori corrections (left) and other waveform properties against each other (right)*

Lake Zurich (S3A)

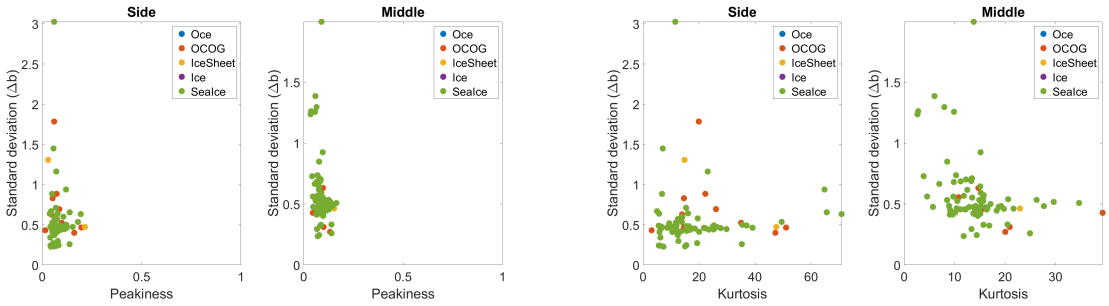

Figure A.31: *Lake Zurich (S3A): Peakiness/kurtosis against standard deviation of a-posteriori corrections*

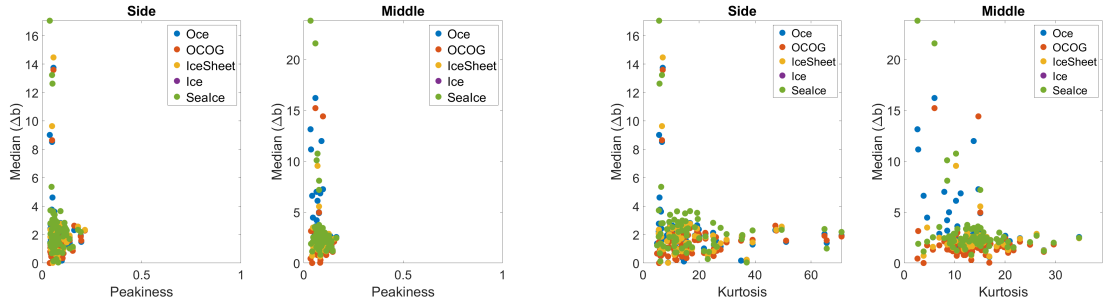

Figure A.32: *Lake Zurich (S3A): Peakiness/kurtosis against median of a-posteriori corrections*

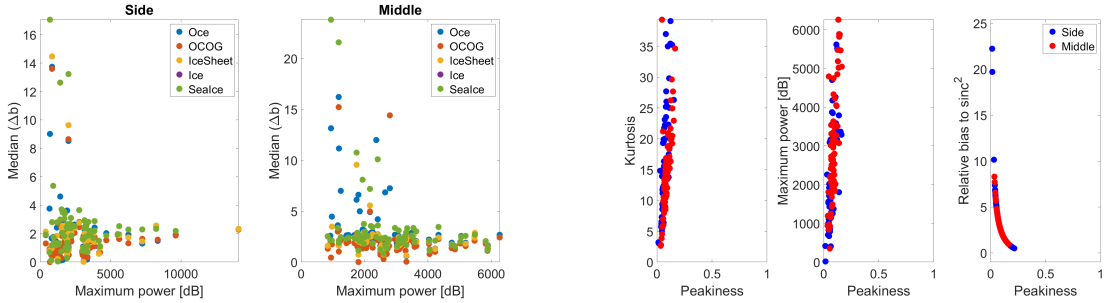

Figure A.33: *Lake Zurich (S3A): Maximum power against median of a-posteriori corrections (left) and other waveform properties against each other (right)*

Lake Zurich (S3B)

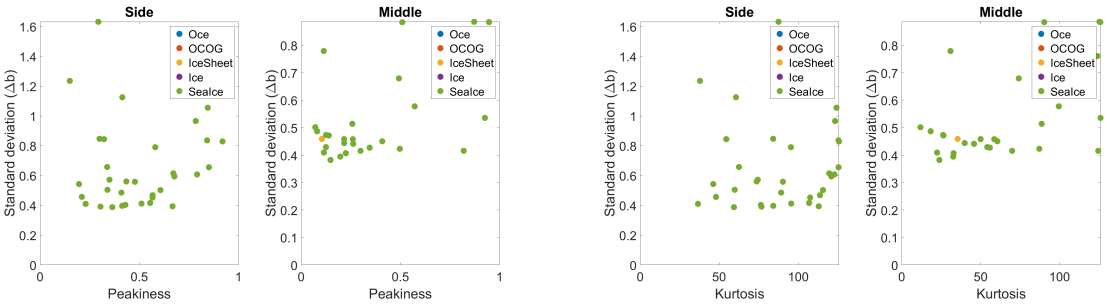

Figure A.34: *Lake Zurich (S3B): Peakiness/kurtosis against standard deviation of a-posteriori corrections*

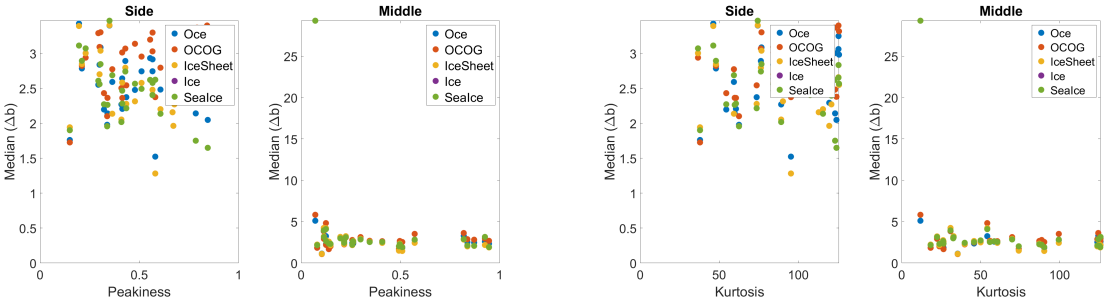

Figure A.35: *Lake Zurich (S3B): Peakiness/kurtosis against median of a-posteriori corrections*

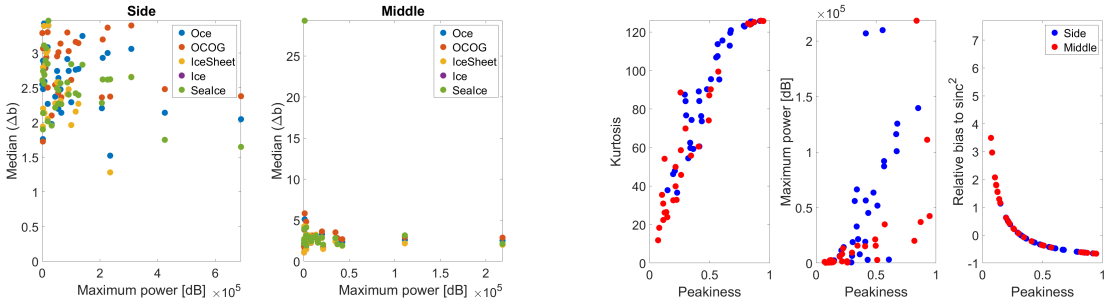

Figure A.36: *Lake Zurich (S3B): Maximum power against median of a-posteriori corrections (left) and other waveform properties against each other (right)*

Lake IJssel (S3A)

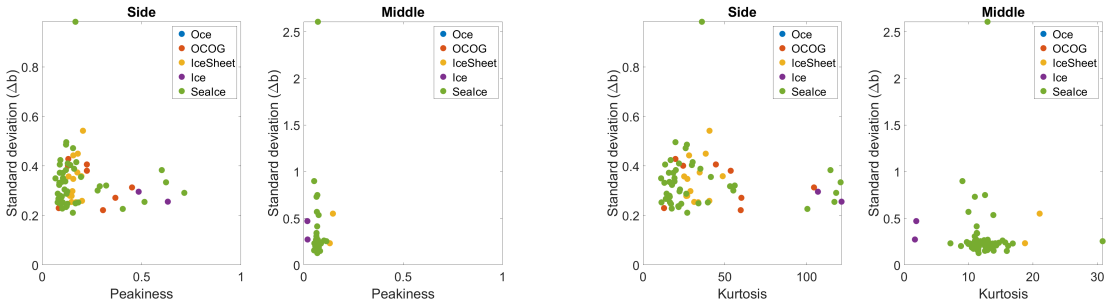

Figure A.37: *Lake IJssel (S3B): Peakiness/kurtosis against standard deviation of a-posteriori corrections*

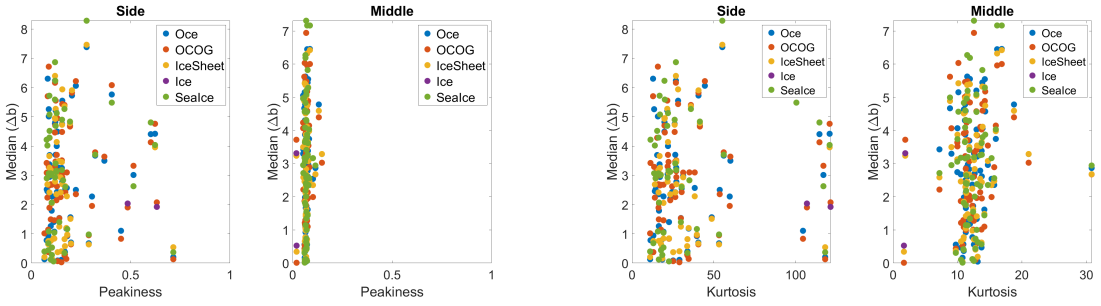

Figure A.38: *Lake IJssel (S3B): Peakiness/kurtosis against median of a-posteriori corrections*

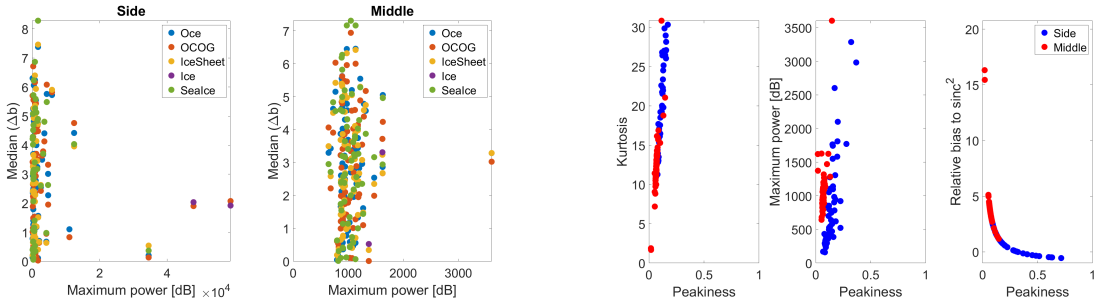

Figure A.39: *Lake IJssel (S3A): Maximum power against median of a-posteriori corrections (left) and other waveform properties against each other (right)*

Lake IJssel (S3B)

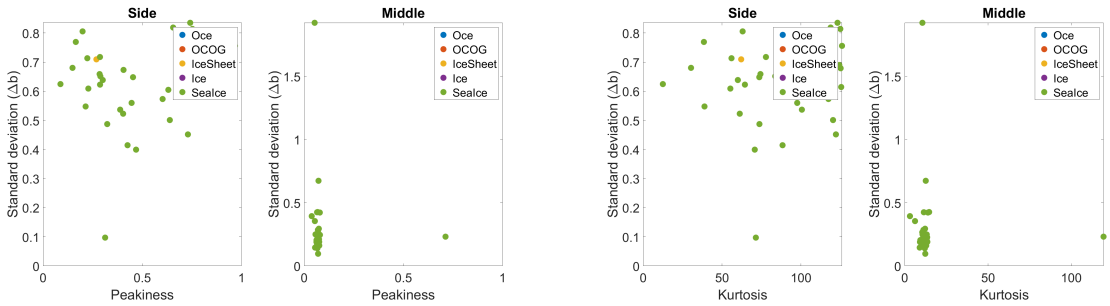

Figure A.40: *Lake IJssel (S3B): Peakiness/kurtosis against standard deviation of a-posteriori corrections*

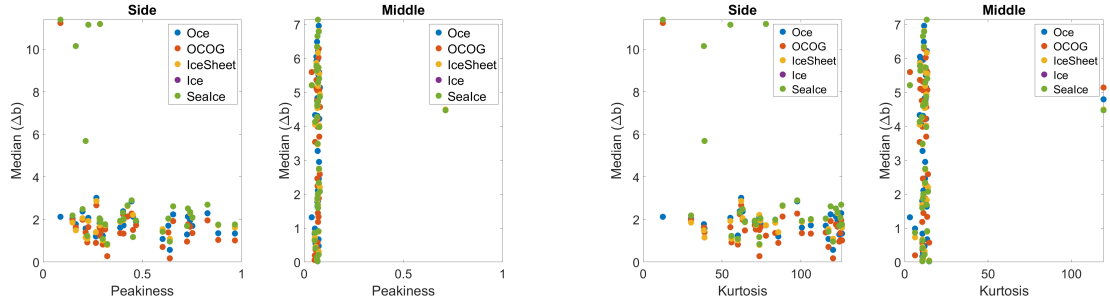

Figure A.41: *Lake IJssel (S3B): Peakiness/kurtosis against median of a-posteriori corrections*

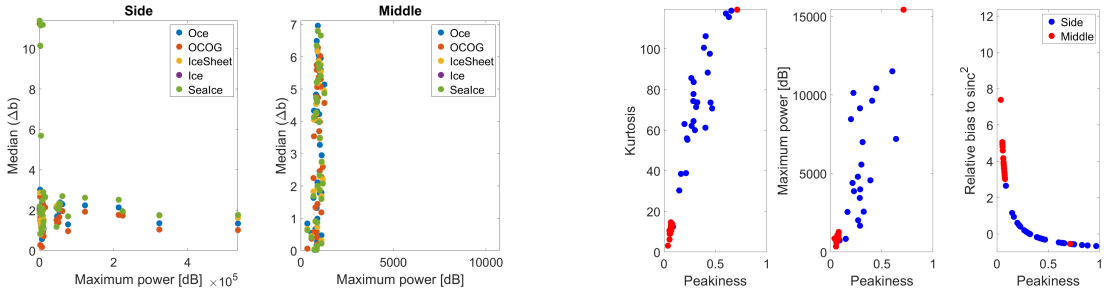

Figure A.42: *Lake IJssel (S3B): Maximum power against median of a-posteriori corrections (left) and other waveform properties against each other (right)*